MODELING OF THE HYDRODYNAMICS WITHIN THE HEADER OF A TUBULAR MEMBRANE MODULE

(James) Dimitrios F. Boukouris

May 1998

A thesis submitted to the School of Graduate Studies and Research in partial fulfillment of the requirements for the degree of Masters of Applied Science in the Department of Chemical Engineering, University of Ottawa.

0-612-36664-2

Abstract

Ultrafiltration (UF) is one of the many technologies used in the treatment of process and wastewaters. Tubular UF membrane modules are used to treat fiber suspensions for effluent control and chemical recovery in the pulp and paper industry. However, the treatment of pulp suspensions with modules containing tubes having an inside diameter of less than 2.54 cm is typically problematic. Severe blockage occurs at the inlet of the tubes due to the accumulation of pulp fibers within the header.

In the present study, the commercial computational fluid dynamics package, CFD-ACE+ was used to simulate the hydrodynamics within the header of a simplified system. The hydrodynamics were simplified by approximating the two-phase pulp suspension with a single-phase Newtonian fluid. The main flow structures within various header geometries were analyzed. Header geometry was varied by chamfering the inlet of a tube at four specific angles. These four angles, referred to as inlet angles, were 0°, 30°, 45°, and 55°. The hydrodynamic features within the different header configurations were compared. A central eddy in the shape of a torus of varying cross section was observed at lower inlet angles. The eddy was less discernable at larger inlet angles. The eddy intensity within the header was identified as the key hydrodynamic structure affecting fiber accumulation. Changes in the average velocity of recirculation of the eddy were found to be closely correlated (r^2=0.9986) to previously reported fiber accumulation results.

Résumé

L'ultrafiltration est un procédé de séparation par membrane utilisé dans le traitement des eaux usagées. Des modules d'ultrafiltration contenant des membranes sous formes tubulaires sont utilisés dans la récupération de produits chimiques et le contrôle des effluent dans l'industrie des pâtes et papier. Cependant, le traitement de solutions diluées de pâtes avec des modules contenant des tubes de moins de 2.54 cm en diamètre demeure problématique. Des fibres bloquent l'entrée de ces tubes lors de l'opération de ces modules.

Dans cette étude, un logiciel commercial de calcul de dynamique des fluides est utilisé pour simuler l'écoulement dans la tête distributrice du module d'ultrafiltration tubulaire pour un système reduit. Le système réduit comprend une approximation de la suspension de fibres, contenant deux phases, par un fluide Newtonien. La geometrie de la tête distributrice est variée pour augmenter l'angle d'entrée des tubes. Quatre angles sont utilisés: 0°, 30°, 45°, and 55°. La présente étude compare ces quatre configurations et identifie des boucles de recirculation présentes dans la tête distributrice en tant que la structure principale qui influence l'accumulation de fibres. Une correlation fortement linéaire (r^2= 0.9986) est observé entre la vitesse moyenne de recirculation de la boucle et l'accumulation de fibres dans la tête distributrice du module. Les résultats indiquent que la diffusion de fibres due au cisaillement du fluide est la cause principale de l'accumulation.

Acknowledgements

I would like to thank Dr. A Tremblay and Dr. D. Taylor for their indispensable support, encouragement and guidance throughout the course of this study. I would also like to thank my family for their support and encouragement throughout my studies. I would like to dedicate this thesis to my wife, Roslyn, whose patience and support has been unlimited during this period.

Nomenclature

Roman Symbols

a	particle size (m)
$\vec{v}$	velocity vector (m/s)
$\vec{r}$	position vector (m)
$\vec{e}_j$	covariant base unit vector
$\vec{e}^{\,j}$	contravariant base unit vector
C	concentration (kg/m^3)
C_μ	coefficient in the eddy viscosity relation in the $k-\varepsilon$ model
$C_{\varepsilon 1}$	coefficient of the production of ε in the ε equation
$C_{\varepsilon 2}$	coefficient of the destruction of ε in the ε equation
C_o	initial concentration (kg/m^3)
D	alternate notation for the rate of turbulence dissipation, ε (m^2/s^3), used in residual plots, 5.7 and 5.8.
D_t	membrane tube diameter (m)
f	body force (N)
I	grid cell index
J	grid cell index
J	Jacobian matrix
k	turbulent kinetic energy (m^2/s^2)
K	grid cell index
l	turbulent length scale (m)

L	tube length (m)
L_c	characteristic length (m)
l_m	Prandtl's mixing length (m)
N_p	particle flux ($kg/m^2{\cdot}s$)
p	pressure (N/m^2)
P	rate of production of turbulent kinetic energy
pp	pressure correction term
Q	flowrate (L/s)
r	radial component coordinate
Re	Reynolds number
Re*	modified Reynolds number
u	x-component of velocity (m/s)
u^+	normalized velocity in wall units
u_c	characteristic velocity (m/s)
u_i	velocity component in the i^{th} direction (m/s)
u_r	magnitude of velocity along centerline of pipe or channel (m/s)
v	y-component of velocity (m/s)
w	z-component of velocity (m/s)
w_{max}	maximum velocity component in the z-direction
y^+	normalized distance from the wall in wall units

Greek Symbols

$\vec{\varepsilon}_j$	covariant base vector
$\vec{\varepsilon}^{\,j}$	contravariant base vector
ρ	density (kg/m^3)
α	inlet angle measured from the deviation to the vertical (degrees)
μ	dynamic viscosity ($kg/m{\cdot}s$)
ν	kinematic viscosity (m^2/s)
ε	rate of turbulence dissipation (m^2/s^3)
ω	specific rate of turbulence dissipation (s^3/m^2)
ϕ	generic transport variable
φ	particle volume fraction
δ	characteristic width
ξ	curvilinear coordinate
η	curvilinear coordinate
ζ	curvilinear coordinate
σ	laminar Prandtl or Schmidt number, scattering coefficient
τ_{ij}	shear stress tensor ($kg/m{\cdot}s^2$)
δ_{ij}	Kronecker delta
μ_t	turbulent (eddy) dynamic viscosity ($kg/m{\cdot}s$)
ν_t	turbulent (eddy) kinematic viscosity (m^2/s)

σ_t turbulent Prandtl or Schmidt number, scattering coefficient

$\dot{\gamma}$ shear rate (s^{-1})

τ_w wall shear stress ($kg/m{\cdot}s^2$)

Subscripts

i index taking values of 1-3

j index taking values of 1-3

k index taking values of 1-3

Superscripts

" fluctuation term for Favre averaging

' fluctuation term for Reynolds averaging

~ density average of Favre averaging, Note, only in Sections 3.3.1-3.4.4, the tilde is dropped for clarity

– mean value, Note, only in Sections 3.3.1-3.4.4, the overbar is dropped for clarity

i index taking values of 1-3

j index taking values of 1-3

k index taking values of 1-3

Table of Contents

List of Tables

List of Figures

Chapter 1.0

Introduction

Environmental regulations are being increased in order to reduce the negative impact of industrial emissions on the environment. One of the many types of industries on which these regulations are being imposed is the pulp and paper industry. Many studies have been conducted to assess the impact of pulp mill effluents on the environment (Riebel and Tyler, 1993).

Currently in Canada, in addition to stringent end-of-pipe regulations, it is now required that pulp and paper mills conduct studies on the waters in which the effluents are being released. These are referred to as Environmental Effects Monitoring (EEM) studies and are designed, in general, to obtain a more all-encompassing and realistic view of mill effluent effects and to eventually perform causative studies (Riebel and Tyler, 1993). Although these regulations are fairly recent, aquatic ecosystem monitoring at Canadian pulp and paper mills date back to the mid 1950's. These mostly consisted of macro-invertebrate (benthic) surveys and water quality analysis both upstream and downstream from mill effluents. Benthic surveys were then related to water quality in order to assess the impact of the effluent on the surrounding ecosystem (Riebel and Tyler, 1993). Much of the environmental work in the sixties and seventies was devoted to the identification of the constituents of pulp mill effluents, which were responsible for acute and chronic toxicity to aquatic organisms (Riebel and Tyler, 1993, Fisheries and Environment Canada, 1978). However, during the mid-seventies to eighties, the toxicity of bleached kraft effluent and the presence of chlorinated organic compounds that could bio-accumulate in aquatic organisms was becoming a major concern (Riebel and Tyler, 1993). This led to the current end-of pipe and EEM regulations and ultimately, the achievement of zero liquid effluent (ZLE) papermaking (Riebel and Tyler, 1993, Wiseman and Ogden, 1996).

Membrane separation technologies have great potential in the realization of these regulations and objectives. Membrane ultrafiltration (UF) has been considered for applications in the pulp and paper industry since the advent of membrane technology (Yao et al., 1994). UF has the potential to be introduced into many aspects of the pulp and paper industry. For instance, during the bleaching stage in a pulp plant, the pulp is chlorinated to break down and remove the lignin present in pulp (Sun et al., 1989). The removal of lignin is desired as it is coloured and tends to cause paper to darken and deteriorate with time (Yao et al., 1994). However, this bleaching process results in effluents rich in chlorinated organics, the majority being chlorolignins. Most of these chlorolignins have molecular weights above 1000 Daltons, while some lower molecular weight chlorolignins are also formed. These low molecular weight chlorolignins are known to be toxic, mutagenic, and bioaccumulative. Although biological treatment has proven to be effective for the degredation of these low molecular weight compounds, its performance is adversely affected in the presence of the high molecular weight fractions of chlorolignins. Also, biological treatment generally does not decrease the colour associated with these compounds (Yao et al., 1994, Sun et al., 1989). It has been proposed that UF be used as a pretreatment for the removal of the high molecular weight components, and clarification of the bleach effluents. A biological treatment could then be used as a polishing step prior to release (Yao et al., 1994). Continuous multi-stage UF has been found to be a technically and economically feasible process for the removal of these colouring compounds and the high molecular weight chlorinated organics (Afonso and De Phino, 1990).

Another example for the potential use of UF in the pulp and paper industry is as a treatment process for paper coating effluents. Paper coating is used by the paper manufacturing industry in order to improve paper quality and printability. Hence, the use of paper coating is increasing. Paper coating procedures often result in the production of dilute paper coating effluents which present problems in post treatment. These paper coating effluents can represent significant economic losses (Jönsson et al., 1996a). Laboratory experiments and pilot-plant experiments performed at the MoDo Silverdan paper mill found that the overall economics of the paper coating process can be improved by the UF treatment of these dilute colour coating effluents. Ultrafiltration enables the recovery of dyes, as the retentate can be reused and the permeate can replace fresh water at some stages in the mills, thus reducing the consumption of fresh water (Jönsson et al., 1996b).

One of the reasons why UF has not reached its full potential in the pulp and paper industry is that the processing of pulp suspensions using membrane modules has been typically problematic. Tubular membrane modules are almost exclusively used for this type of application. It is found that when tubes of an internal diameter less than one inch are employed, blockage of the module occurs. This blockage is due to the accumulation of fibers within the header of the tubular membrane module, resulting in blockage at the entrance of the tubes. Hence, the current larger tube diameter separation systems suffer from low membrane surface area to fluid volume ratios.

Recently, an experimental study was performed at the University of Ottawa by Mr. Edgard Chehab (Chehab, 1995) which investigated the effects of header geometry on the accumulation of pulp fibers within tubular membrane module headers. It was found that changes to the inlet region of the tubes led to a reduction of approximately sixty percent of the accumulation in the header.

In this study, it was decided to investigate the flow of a pulp suspension through a module header using a mechanistic hydrodynamic model. The aim of this study was to model the hydrodynamics within the header and identify hydrodynamic characteristics that could cause the accumulation of particulates within the header. Attempts could then be made to correlate these modeling efforts with Chehab's experimental results. The commercial computational fluid dynamics package, CFD-ACE+ was used to model the system.

Modeling multi-phase, turbulent flow in a complex, re-circulating, 3D geometry is a complex and computationally intensive activity. Therefore, the approach was to use a simplified model of single-phase, Newtonian turbulent flow and see if this was sufficient to provide insight into the experimental results. During his previous study, Chehab also evaluated the rheology of the pulp suspension in use. His findings indicated that a 0.5% pulp suspension exhibits Newtonian behaviour (Chehab, 1995). Chase *et al.*

also found that both softwood and hardwood pulp suspensions of 0.5 % exhibited Newtonian behaviour (Chase *et al.* 1989).

The ultimate goal of this work would be to use a commercial CFD package as a potential design tool. The immediate objective was to identify characteristics of single-phase Newtonian flow that correlate well with the experimental observations of accumulation. These characteristics could then be used to evaluate other geometric configurations. If necessary, more complex models could then be considered. The objective of this study, then, is to link the results of the hydrodynamic modeling using single-phase Newtonian flow to the experimental observations obtained by Chehab (Chehab, 1995).

Chapter 2.0

Background

As mentioned in the introduction, ultrafiltration (UF) processes show great promise in the achievement of both effluent control and chemical recovery objectives in pulp and paper plants. However this promise has yet to be fully realized. Widespread use of UF processes in the treatment of pulp suspensions has been limited since the behaviour of these suspensions in the entrance region of the UF modules has been found to be typically problematic.

2.1 Previous Study on Particulate Accumulation in a Module Header

In this section, the module header geometry and selected experimental results obtained in Chehab's study (Chehab, 1995) will be presented. The general approach was to modify the header geometry, or more specifically, the geometry surrounding the inlet to the membrane tubes, and to perform a set of experiments that would investigate the effect of inlet geometry on both steady-state and transient fiber accumulation within the header. It was decided that these modifications should be simple in design and should not require the replacement of current technologies. The solution was that these changes would be implemented by way of retrograde plate inserts that could be fitted over the bottom of the header. Another issue was that the research focus was on the behaviour of pulp suspensions at the inlet region of the tubular membrane module and not on the membrane performance itself. Therefore, the tubular membranes in the module were replaced by non-porous acrylic tubes.

Figure 2.1 is a diagram illustrating a section of the tubular membrane module header used in Chehab's work. It illustrates the three distinct parts of the model header: 1) the distributor header chamber, consisting of a 1 in. (0.0254 m) inner diameter inlet tube which empties into a 3 in. (0.0762 m) long expansion chamber, 6 in. (0.1524 m) in diameter; 2) the exchangeable distributor header plate which has a diameter equal to that of the expansion tube and a height of 0.5 in. (0.0127m); and 3) the base plate and the tubes which it holds together. Also depicted are two other header plates with different inlet geometries.

Inlet tube geometry is altered by variation of an inlet angle α. This angle α results from the chamfering of the tubes and is measured from the deviation away from the inside wall of the tube, as seen in Figure 2.2. Figure 2.2 shows a schematic diagram of a cross-sectional view of the header plate, having an inlet angle of 30°. A straight tube has a value of α equal to 0°.

In all experiments, the number of outlet tubes was fixed at five. The distances from the centers of the tubes to the center of the header was fixed and equal, as were the angles between the tubes in relation to the center of the header. These design constraints are depicted in Figure 2.3.

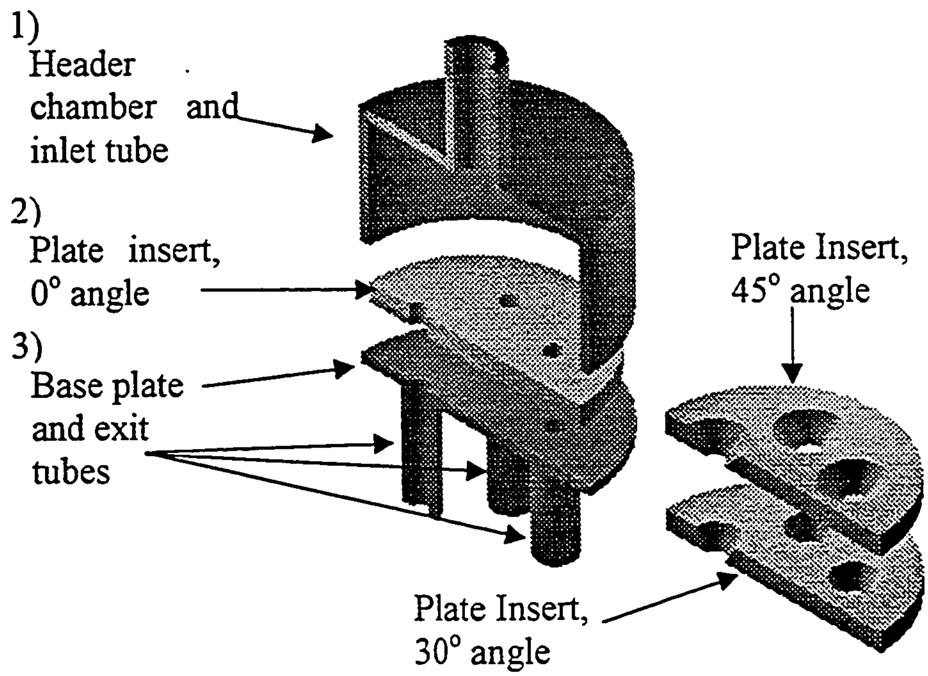

Figure 2.1: Section of the model header and plate inserts for the ¼ in. (0.00635 m) ID tubes.

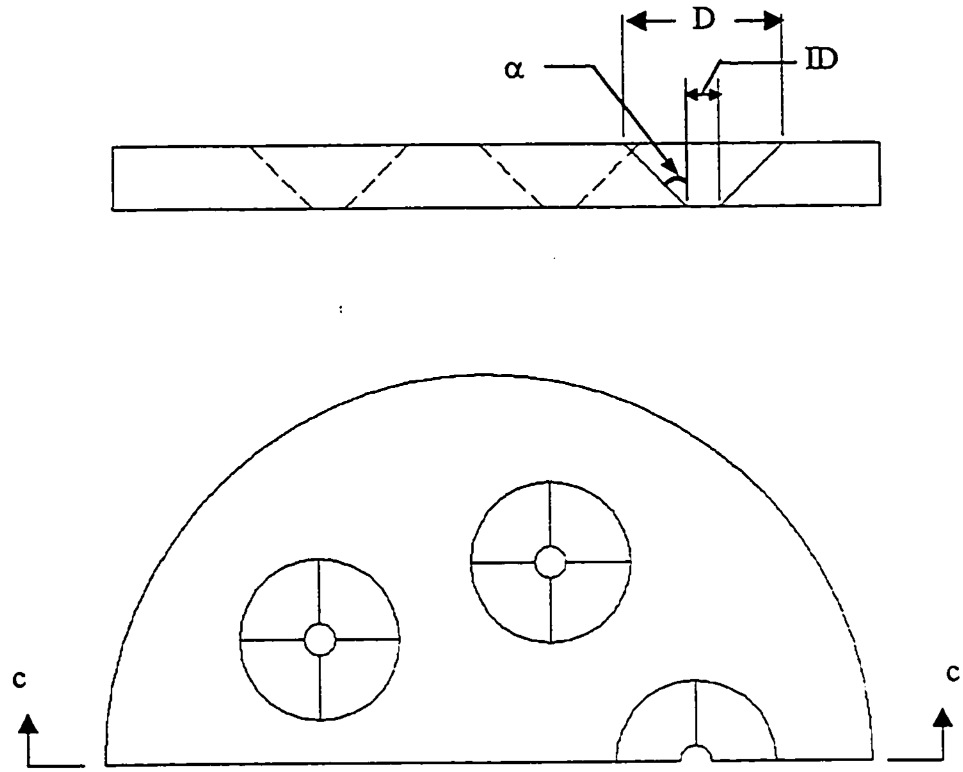

Figure 2.2: Schematic of a cross-sectional view of the header plate for $\alpha = 30°$.

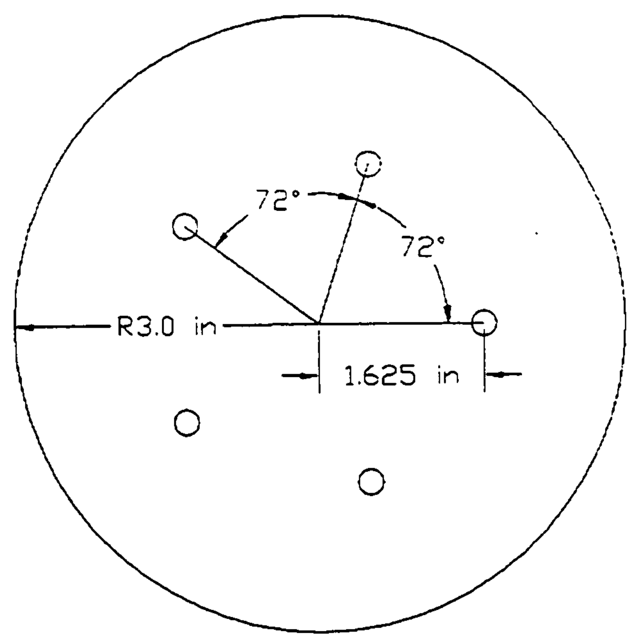

Figure 2.3: Schematic diagram depicting the design constraints for the model header.

Tubular membrane module cost can be measured by the ratio of the membrane surface area to fluid volume treated. The greater the ratio the lower the cost. An indication of this cost can be obtained by considering the ratio of membrane surface area to the fluid volume inside the tubes. This surface area to volume ratio can be expressed in terms of tube diameter, D_t, as follows:

$$\frac{membrane\ surface\ area}{fluid\ volume} = \frac{4}{D_t}, \tag{2.0-1}$$

Therefore for a given membrane tube length, the surface area to volume ration varies inversely with tube diameter. As mentioned in Section 1.0, industrial applications employ membranes with an inner diameter of 1 in. (0.0254 m), as applications employing membranes with a smaller inner diameter have been problematic. As it is most beneficial to operate with the smallest tube diameter possible and that the objective was to investigate header geometry on the accumulation phenomenon, Chehab's study focussed on tubes in this problematic range. The final physical configurations studied were model headers with tubes of ½ in. (0.0127 m) and ¼ in. (0.00635 m). The header containing the ½ in. (0.0127 m) diameter tubes were examined with three inlet geometries: $\alpha = 0°, 30°, 45°$, and the header containing the ¼ in. (0.00635 m) diameter tubes were examined with four inlet geometries: $\alpha = 0°, 30°, 45°$, and $55°$, for a total of seven configurations investigated.

Figure 2.4 depicts a flowchart of the experimental set-up used in Chehab's study (Chehab, 1995). The experiments were performed as follows: a 0.5 wt. % pulp suspension, consisting of 90% unbleached liner Kraft board and 10% bleached liner Kraft board was circulated from a storage/preparation tank through the model header for a specified time interval. At the end of each time interval, the suspension inside the cell was collected and weighed. The mass fraction of fibers within the header was determined gravimetrically. Each scenario was performed in triplicate to determine the reproducibility of the accumulation effects. In all experiments, the flowrate was kept constant at 1 L/s (0.001 m^3/s).

Selected results from Chehab's work are presented as averages in Table 2.1. Table 2.1 lists the average final steady-state, % accumulation of fibers for both diameters investigated and at all inlet angles studied.

Examining the results presented in Table 2.1, we see the overall effect of both the inlet angle α, and exit tube diameter on fiber accumulation. As the tube diameter increases fiber accumulation decreases. Specifically, we see that the accumulation at $\alpha = 0°$ for the ½ in. (0.0127 m) ID case was nearly half of that for the ¼ in. (0.00635 m) case. For the effect of inlet angle on accumulation, we see that as α increases, there is a reduction in the observed accumulation. In particular, if we examine the ¼ in. (0.00635 m) ID results, the accumulation observed using $\alpha = 55°$ is less than half of that observed for the base case of $\alpha = 0°$. Thus, it is experimentally shown that by altering the inlet geometries of the tubes, fiber accumulation can be reduced.

Table 2.1: Fiber accumulation after 24 hrs of circulation for the ¼ in. (0.00635 m) and the ½ in. (0.0127 m) ID tubes with different values of α (Chehab, 1995).

Angle α	¼ in. inner diameter tubes	½ in. inner diameter tubes
	Average Fiber accumulation (%)	Average Fiber accumulation (%)
0°	33.54	17.72
30°	28.15	12.38
45°	21.86	10.69
55°	13.36	N/A

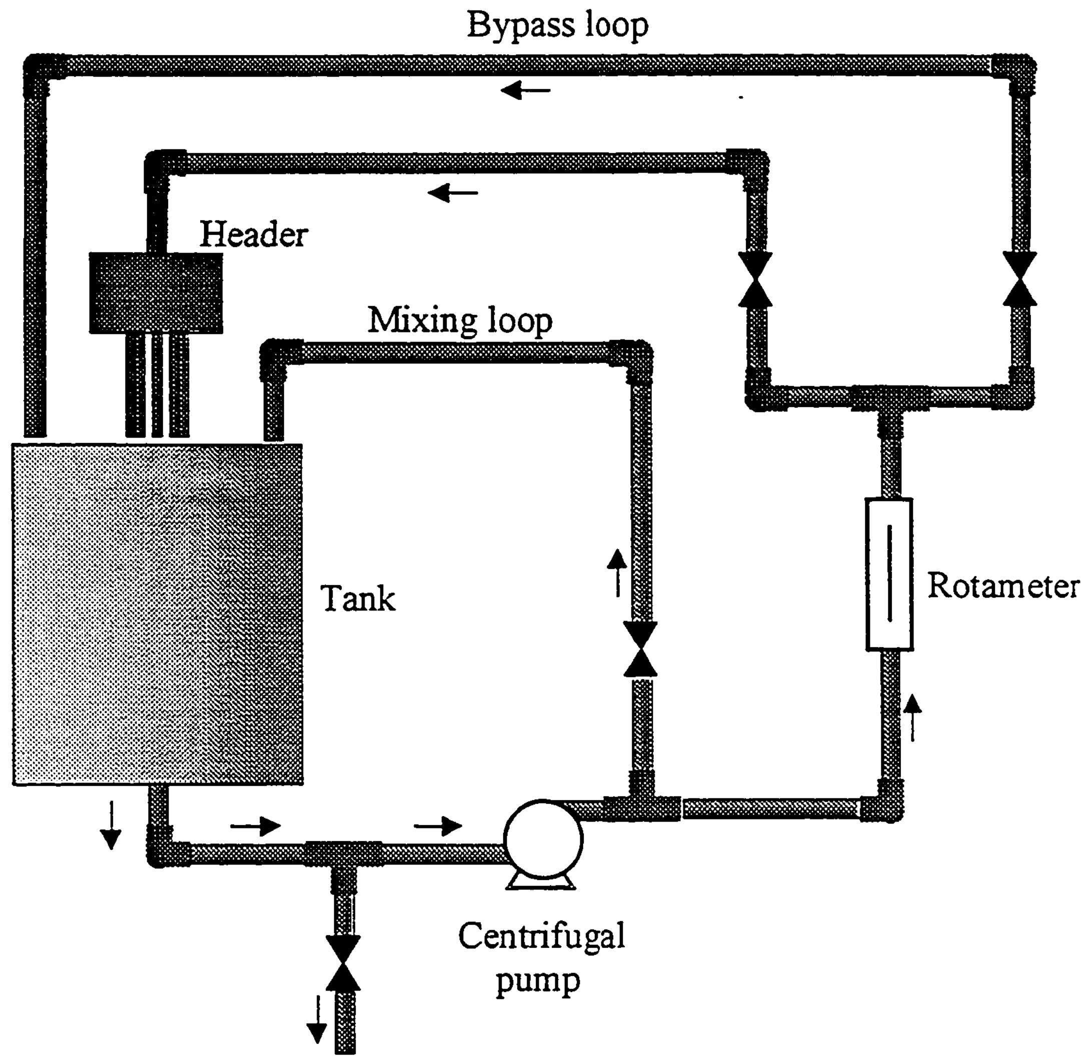

Figure 2.4: Schematic flow chart of the experimental apparatus used in (Chehab, 1995).

2.2 Possible Causes of Accumulation

The flow behaviour of particulate suspensions in a Couette device (concentric cylinders), was studied by Eckstein, *et al.*, (1977), Gadala-Maria and Acrivos (1980), and Leighton and Acrivos (1987a). They observed that when a suspension of particles was sheared, individual particles within the suspension experienced a random migration, which could be characterized as a diffusive process. It was established that this random migration was not due to thermal effects nor to Brownian motion, but to chaotic particle trajectories caused by shear (Brady, 1994). Gadala-Maria and Acrivos (1980), and Leighton and Acrivos (1987b) also observed that in the presence of an inhomogeneous shear rate, particles migrate from the regions of high shear rate to regions of low shear rate. This migration was proven to be intrinsic and led to concentration inhomogeneities in any inhomogeneous flow (Brady, 1994). This phenomenon is often referred to as shear-induced diffusion, or shear diffusivity. (Leighton and Acrivos, 1987a).

Other possible causes of phase separation are particle impingement onto the center of the bottom insert plate and centrifugal forces due to the spinning nature of the eddy formation that could force particles into the dead spaces within the header.

Chapter 3.0

Mathematical Modeling

In this section, the physical system and the mathematical models used to simulate the hydrodynamics within the header are presented. The physical system includes the pulp suspension and the header geometry. The mathematical model consists of the mass and momentum equations, and the turbulence model. These will be presented in 3-dimesional, steady-state, Cartesian form. Incorporation of the boundary conditions into the model is also be presented.

3.1 Physical System

The final physical system that was to be modeled consisted of the fluid representing the pulp suspension and the model header as described in the previous chapter. The flowrate, as in Mr. Chehab's study, was 1 L/s, giving rise to turbulent flow. The pulp suspension, used in all modeling studies, was represented by a single phase Newtonian fluid displaying a density and viscosity equal to those of Mr. Chehab's suspension: 970 kg/m^3 an 11.08 cp respectively. As mentioned earlier, the approximation of the suspension as a Newtonian fluid was found to be reasonable (Chehab, 1995). The length of the inlet tube was set to 5 in. (0.127 m), as were the lengths of the exit tubes. These values were chosen mostly due to computer memory constraints, but were found to be sufficiently long as to avoid end effects. Also, the smallest exit tube diameter, ¼ in. (0.00635 m), that was successfully examined by Mr. Chehab would be investigated as this was expected to give a more enhanced picture of the hydrodynamics leading to accumulation.

Figure 3.1 shows the model header from three views: a) top, b) side and c) isometric. It also illustrates its relation to the cartesian coordinate system. The z-component lies axially along the center of the header, with z = 0 at the inlet into the expansion chamber, and a cross-section of the header defined by an x–y plane. The location of the origin was chosen for ease of geometry creation in the CFD software.

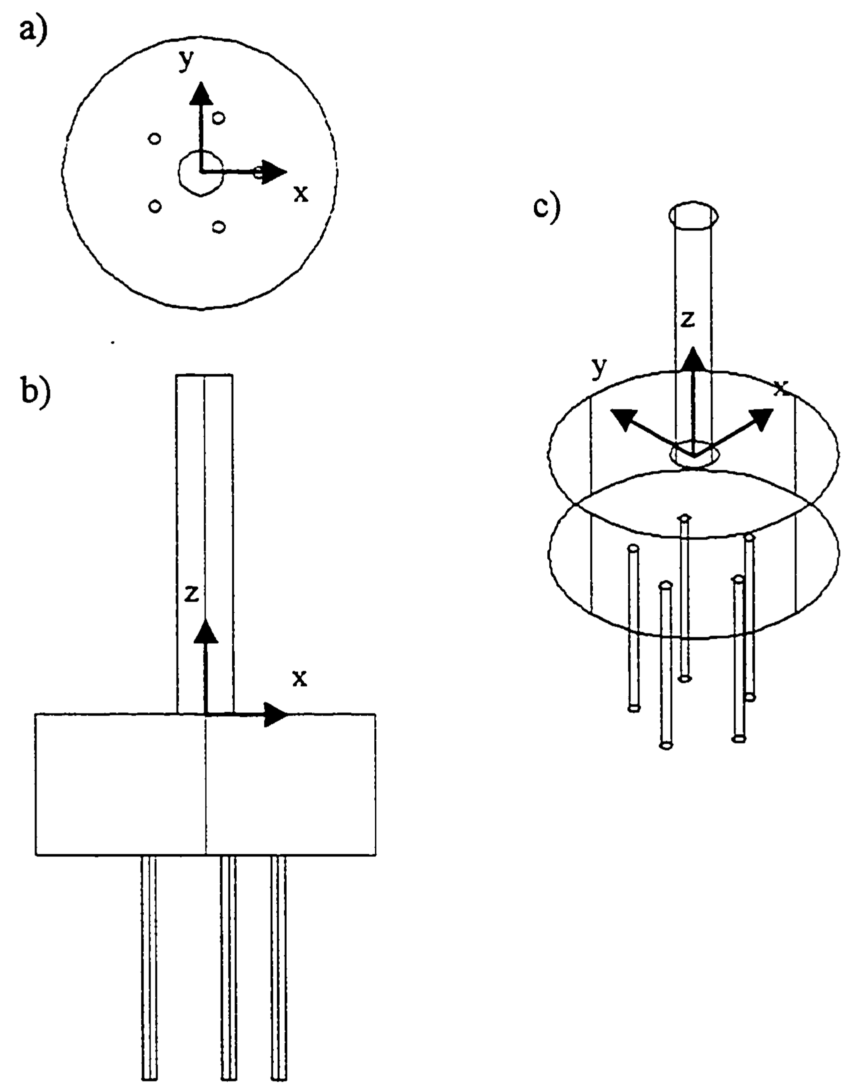

Figure 3.1: Model header from 3 views: a) top, b) side and c) isometric.

Early on it was found that modeling the entire header was computationally intensive and was rather unstable with respect to numerical convergence. Therefore, it was decided to take advantage of the symmetry inherent in the header design. Figure 3.2 depicts this ten-fold symmetry both in a cross-sectional view of the header and in isometric view with a symmetry sub-unit removed. Each symmetry sub-unit is a mirror image of an adjacent sub-unit. Thus, this symmetry enabled us to reduce the size of the problem by an order of magnitude.

3.2 Governing Differential Equations

In computational fluid dynamics (CFD) analysis, fluid flows are simulated by numerically solving the partial differential equations that govern the transport of flow quantities such as mass, momentum, energy, species concentration, turbulence quantities, mixture fractions, and heat fluxes. These differential equations, consisting of terms denoting influences on a unit-volume basis, express a conservation principle.

3.2.1 The Equation of Continuity

The equation of continuity is based upon the principle of the conservation of mass. It describes the rate of change of density at a fixed point resulting from the

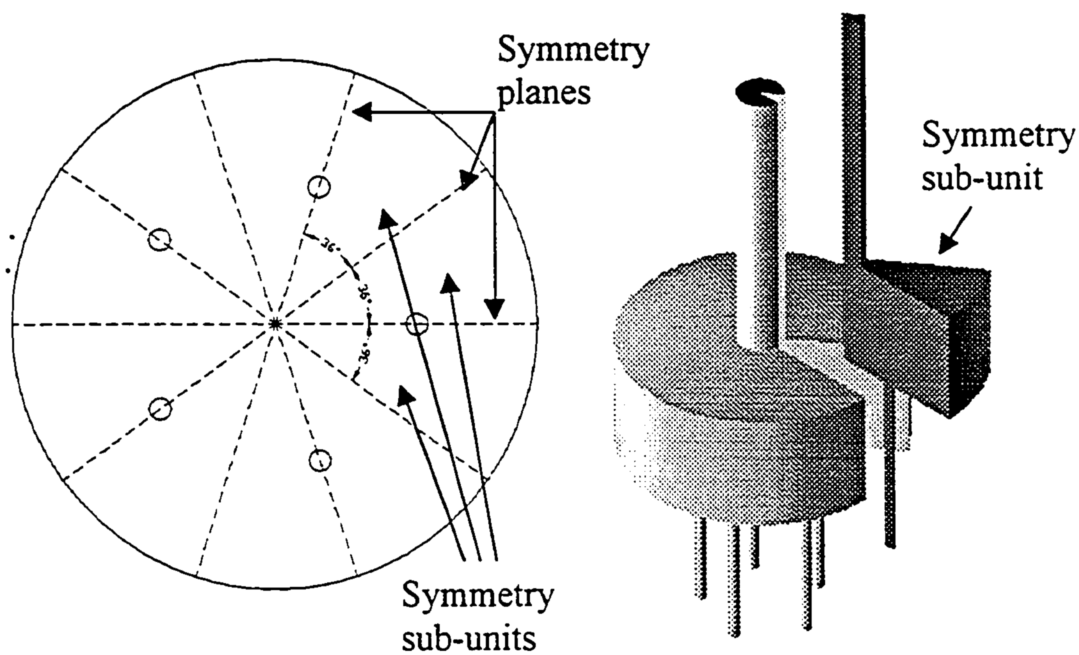

Figure 3.2: Ten-fold symmetry in the model header.

changes in the mass velocity vector (Bird et al., 1960). The equation of continuity in steady-state form can be expressed as follows:

$$\underbrace{\frac{\partial}{\partial x_j}(\rho\, u_j)}_{\substack{\text{net rate of mass}\\ \text{efflux per unit volume}}} = 0 \,. \tag{3.2-1}$$

3.2.2 The Equation of Motion

The equation of motion, also referred to as the momentum equation, is based upon the principle of the conservation of momentum. This momentum balance is equivalent to Newton's second law (Bird et al., 1960). The momentum equation, in steady-state form, can be expressed as follows:

$$\underbrace{\frac{\partial}{\partial x_j}(\rho\, u_i u_j)}_{\substack{\text{rate of momentum}\\ \text{gain by convection}\\ \text{per unit volume}}} = \underbrace{-\frac{\partial p}{\partial x_i}}_{\substack{\text{pressure force}\\ \text{on element per}\\ \text{unit volume}}} + \underbrace{\frac{\partial \tau_{ij}}{\partial x_j}}_{\substack{\text{rate of momentum}\\ \text{gain by viscous transfer}\\ \text{per unit volume}}} + \underbrace{\rho f_i}_{\substack{\text{body forces}\\ \text{on element per}\\ \text{unit volume}}} \,. \tag{3.2-2}$$

In order to be able to determine velocity distributions from these equations, it is necessary to obtain expressions for the stress tensors in terms of velocity gradients and fluid properties (Bird et al., 1960). For Newtonian fluids, τ_{ij} can be related to the velocity gradients through (CFDRC, 1993):

$$\tau_{ij} = \mu\left(\frac{\partial u_i}{\partial x_j} + \frac{\partial u_j}{\partial x_i}\right) - \frac{2}{3}\mu\left(\frac{\partial u_k}{\partial x_k}\right)\delta_{ij} \;, \tag{3.2–3}$$

where δ_{ij} is the Kronecker delta. The Kronecker delta takes a value of one when the indexes i and j are equal, and zero when they are not.

Substitution of equation (3.1.1–3) into equation (3.1.1–2) results in the Navier-Stokes equation:

$$\frac{\partial}{\partial x_j}\left(\rho u_i u_j\right) = -\frac{\partial p}{\partial x_i} + \frac{\partial}{\partial x_j}\left[\mu\left(\frac{\partial u_i}{\partial x_j} + \frac{\partial u_j}{\partial x_i}\right) - \frac{2}{3}\mu\frac{\partial u_k}{\partial x_k}\delta_{ij}\right] + \rho f_i \,. \tag{3.2–4}$$

3.2.3 Favre Averaged Equations

In the case of turbulent flows, direct numerical simulation of the governing equations is possible only for very low Reynolds numbers. As turbulent flows contain a wide range of time and length scales, it is often necessary to employ very short time steps and fine grids. Otherwise, CPU and memory requirements would surpass even the largest and fastest of today's computers. As Wilcox quotes Speziale (1985), "a direct numerical simulation of turbulent pipe flow at Re = 500 000 would require a computer ten million times faster than a Cray Y/MP" (Wilcox, 1993).

In most engineering applications, however, it is the time-mean behaviour that is of practical interest (CFDRC, 1993). Therefore, the Navier-Stokes equations are converted into the time-averaged equations for turbulent flow by an averaging operation in which it is assumed that there are rapid and random fluctuations about the mean value. In the averaging process, a flow quantity ϕ is decomposed into mean and fluctuating parts. There are two types of averaging that are generally used: Reynolds or time averaging and Favre or density averaging.

Reynolds averaging:

$$\phi = \overline{\phi} + \phi' \qquad (3.2\text{–}5a)$$

where,

$$\overline{\phi} = (1/T)\int_{t_0}^{t_0+T} \phi dt \qquad (3.2\text{–}5b)$$

Favre averaging:

$$\phi = \widetilde{\phi} + \phi'' \qquad (3.2\text{–}6a)$$

where,

$$\widetilde{\phi} = \overline{\rho\phi}/\overline{\rho} \qquad (3.2\text{–}6b)$$

CFD–ACE employs Favre averaging for the solution of turbulence flows; therefore only the Favre averaged forms of the governing equations are presented.

Applying the Favre averaging procedure to Equation (3.2–1), gives us the Favre averaged form of the continuity equation:

$$\frac{\partial}{\partial x_j}\left(\bar{\rho}\,\tilde{u}_j\right)=0. \tag{3.2–7}$$

Similarly, we can average the Navier-Stokes equation, Equation (3.2-4) and obtain the Favre-averaged Navier-Stokes equation (FANS):

$$\frac{\partial}{\partial x_j}\left(\bar{\rho}\,\tilde{u}_i\tilde{u}_j\right)=-\frac{\partial \bar{p}}{\partial x_i}+\frac{\partial}{\partial x_j}\left[\bar{\mu}\left(\frac{\partial \tilde{u}_i}{\partial x_j}+\frac{\partial \tilde{u}_j}{\partial x_i}\right)-\frac{2}{3}\frac{\partial \tilde{u}_m}{\partial x_m}\delta_{ij}\right]+\frac{\partial}{\partial x_j}\left(-\bar{\rho}\,\widetilde{u_i'' u_j''}\right). \tag{3.2–8}$$

As a result of the averaging process, the FANS equations may contain less information than the full Navier–Stokes equations, but still contain additional unknown terms. These $\left(-\bar{\rho}\,\widetilde{u_i'' u_j''}\right)$ terms are called Reynolds stresses and must be specified in order to achieve closure of the FANS equations (CFDRC, 1993). Turbulence modeling overcomes this problem of closure by devising approximations for the unknown quantities in terms of flow properties that are known (Wilcox, 1993). A large number of models exist, each with their weaknesses, strengths, and regions of applicability. A comprehensive account of all turbulence models and their development is beyond the scope of this work. However in the next section, a brief description of the turbulence models available in CFD–ACE will be presented as given by CFDRC (CFDRC, 1993).

3.3 Turbulence Models

As mentioned earlier, the FANS equations contain the unknown Reynolds stress terms that must be modeled to achieve closure. All the turbulence models available in CFD–ACE employ the generalized Boussinesq eddy viscosity concept in which the Reynolds stress is approximated as a linear function of the mean strain rate:

$$-\bar{\rho}\widetilde{u_i'' u_j''} = \mu_t\left(\frac{\partial \tilde{u}_i}{\partial x_j} + \frac{\partial \tilde{u}_j}{\partial x_i} - \frac{2}{3}\frac{\partial \tilde{u}_m}{\partial x_m}\delta_{ij}\right) - \frac{2}{3}\bar{\rho}k\delta_{ij} \qquad (3.3\text{–}1)$$

where μ_t is the turbulent eddy viscosity and k is the kinetic energy (per unit mass) of the turbulence fluctuations, given as half the trace of the Reynolds stress tensor:

$$k = \frac{1}{2}u_k'' u_k''. \qquad (3.3\text{–}2)$$

CFD–ACE offers a choice of six turbulence models: the Eddy Viscosity Model, the Baldwin-Lomax Model, the standard k–ε model, the RNG k–ε model, the k–ω model, and the Low Re k–ε model. Substituting Equation (3.3–1) into the FANS equations, Equation (3.2–8), gives us the modeled FANS equations:

$$\frac{\partial}{\partial x_j}\left(\bar{\rho}\tilde{u}_i\tilde{u}_j\right) = -\frac{\partial \bar{p}}{\partial x_i} + \frac{\partial}{\partial x_j}\left[\left(\bar{\mu} + \mu_t\right)\left(\frac{\partial \tilde{u}_i}{\partial x_j} + \frac{\partial \tilde{u}_j}{\partial x_i} - \frac{2}{3}\frac{\partial \tilde{u}_m}{\partial x_m}\delta_{ij}\right)\right] - \frac{2}{3}\frac{\partial}{\partial x_i}\left(\bar{\rho}k\right). \qquad (3.3\text{–}3)$$

A brief description will be given for each model in turn. Please note however, that in the following descriptions, the overbar for μ and ρ tilde for u, v, etc. will be dropped for clarity (CFDRC, 1993).

3.3.1 The Eddy–Viscosity Model

The Eddy–Viscosity Model is an algebraic turbulence model or a zero-equation turbulence model. By definition, an n-equation model is a model in which the solution to n differential transport equations, in addition to the standard conservation equation, is required (Wilcox, 1993). Therefore, the only information required is a correlation for the turbulent viscosity term, μ_t, in equation (3.3–3) given by (CFDRC, 1993):

$$\mu_t = C\bar{\rho}ql, \qquad (3.3.1\text{–}1)$$

where q is a velocity scale and l is a length scale. As μ_t is entered as a constant by the user, knowledge of flow behaviour must be known *a priori* in order for the simulation to be representative of the flow (Wilcox, 1993).

3.3.2 The Baldwin–Lomax Model

The Baldwin–Lomax model also belongs to the group of algebraic models. However in this model, μ_t is calculated using two expressions, one for the region inside the boundary layer and one for the region outside of it. Thus, μ_t is given by the following:

$$\mu_t = \begin{Bmatrix} \mu_{t,inner} \; for \; y \le y_{crossover} \\ \mu_{t,outer} \; for \; y \ge y_{crossover} \end{Bmatrix}. \tag{3.3.2–1}$$

The turbulent viscosity in the inner layer is given by:

$$\mu_{t,inner} = \rho \, l_m^{\,2} |\omega|, \tag{3.3.2–2}$$

where l_m is Prandtl's mixing length:

$$l_m = \kappa y \left[1 - \exp\left(-y^+ / A^+\right)\right], \tag{3.3.2–3}$$

and ω is the magnitude of the vorticity given by:

$$|\omega| = \left[\left(\frac{\partial u}{\partial y} - \frac{\partial v}{\partial x} \right)^2 + \left(\frac{\partial v}{\partial z} - \frac{\partial w}{\partial y} \right)^2 + \left(\frac{\partial w}{\partial x} - \frac{\partial u}{\partial z} \right)^2 \right]^{1/2}. \tag{3.3.2–4}$$

In Equation (3.3.2–3), A^+ is the Van Driest damping constant, and y^+ is the distance from the wall in wall units defined by:

$$y^+ = y u_\tau / \nu, \;\; u_\tau = \sqrt{\tau_w / \rho}. \tag{3.3.2–5}$$

In the above expression, u_τ is commonly referred to as the friction velocity with τ_w being the shear stress at the wall.

The turbulent viscosity in the outer layer is given by:

$$\mu_{t,outer} = K\, C_{cp}\, \rho\, F_{wake}\, F_{kleb}(y) \qquad (3.3.2\text{–}6)$$

where K is the Clauser constant and F_{wake} is given by:

$$F_{wake} = \min\left\{ y_{max} F_{max},\, C_{wk}\, y_{max} \frac{U_{dif}^{\,2}}{F_{max}} \right\}. \qquad (3.3.2\text{–}7)$$

The quantity U_{dif} is determined from:

$$U_{dif} = \sqrt{\left(u^2 + v^2 + w^2\right)_{max}} - \sqrt{\left(u^2 + v^2 + w^2\right)_{min}}\ . \qquad (3.3.2\text{–}8)$$

The quantities, y_{max} and F_{max} are determined from the following function:

$$F(y) = y|\omega|\left[1 - \exp\left(-y^+ / A^+\right)\right], \qquad (3.3.2\text{–}9)$$

where F_{max} is the maximum value of $F(y)$ that occurs within the boundary layer and y_{max} is the value of at which the maximum occurs. The Klebanoff intermittency factor, $F_{kleb}(y)$, in Equation (3.3.2–6) is given by the following:

$$F_{kleb}(y) = \left[1 + 5.5\left(\frac{C_{kleb}\,y}{y_{\max}}\right)^{6}\right]^{-1}. \qquad (3.3.2\text{–}10)$$

The six constants used in this model are:

$$A^{+} = 26;\ C_{cp} = 1.6;\ C_{kleb} = 0.3;\ C_{wk} = 0.25;\ \kappa = 0.4;\ K = 0.0168.$$

3.3.3 The k–ε Model

The k–ε model belongs to the group of two equation models, requiring the solution to two additional differential conservation equations beyond those of mass and momentum. For the past two decades, two–equation models of turbulence have dominated the field of turbulent model research, the most popular of which is the k–ε model (Wilcox, 1993). The form of the k–ε employed by CFD–ACE is that of Launder and Spalding (1974). This model is so well known that it is often referred to as the standard k–ε model and explicit reference to the paper is often omitted (Wilcox, 1993).

This model is composed of the two additional differential equations expressing the transport of k, the specific turbulence kinetic energy, and ε, the turbulence dissipation, as follows:

$$\frac{\partial}{\partial x_j}(\rho u_j k) = \rho P - \rho\varepsilon + \frac{\partial}{\partial x_j}\left(\left(\mu + \frac{\mu_t}{\sigma_k}\right)\frac{\partial k}{\partial x_j}\right), \tag{3.3.3–1}$$

and

$$\frac{\partial}{\partial x_j}(\rho u_j \varepsilon) = \frac{\partial}{\partial x_j}\left(\left(\mu + \frac{\mu_t}{\sigma_\varepsilon}\right)\frac{\partial \varepsilon}{\partial x_j}\right) + C_{\varepsilon_1}\frac{\rho P\varepsilon}{k} - C_{\varepsilon_2}\frac{\rho\varepsilon^2}{k}, \tag{3.3.3–2}$$

where,

$$P = \nu_t\left(\frac{\partial u_i}{\partial x_j} + \frac{\partial u_j}{\partial x_i} - \frac{2}{3}\frac{\partial u_m}{\partial x_m}\delta_{ij}\right)\frac{\partial u_i}{\partial x_j} - \frac{2}{3}k\frac{\partial u_m}{\partial x_m}. \tag{3.3.3–3}$$

The equation for eddy viscosity in kinematic form is as follows:

$$\upsilon_t = \frac{C_\mu k^2}{\varepsilon}. \tag{3.3.3–4}$$

The square root of k is taken to be the velocity scale while the length scale is obtained from the following:

$$l = \frac{C_\mu^{3/4} k^{3/2}}{\varepsilon}. \tag{3.3.3–5}$$

The five constants used in the model are:

$$C_\mu = 0.09;\ C_{\varepsilon 1} = 1.44;\ C_{\varepsilon 2} = 1.92;\ \sigma_k = 1.0;\ \sigma_\varepsilon = 1.3.$$

3.3.4 Wall Functions

Before continuing with the descriptions of the rest of the models available, a certain characteristic that some of these models share should be described in further detail. The standard k–ε model described above is also classified as a 'high Reynolds number' model. However, the qualifier here refers to the turbulent Reynolds number defined by Equation (3.3.4–1) and not the global Reynolds number (CFDRC, 1993).

$$\mathrm{Re}_t = \frac{k^2}{\nu\varepsilon} \tag{3.3.4–1}$$

From Equation (3.3.4–1), we see that Re_t is proportional to the ratio of the eddy viscosity to the molecular viscosity (*cf.* Eq. 3.3.3–4). Thus high Re models are designed for turbulent regions where the eddy viscosity is much larger than the molecular viscosity. The problem is that in the near-wall regions where viscous effects dominate and the molecular viscosity may be of the same order of magnitude or larger than the turbulent viscosity, the high Re models become invalid. The solution is to employ 'wall functions' in these near wall regions, which essentially connect the conditions at some distance from the wall with those at the wall (CFDRC, 1993).

CFD–ACE employs the standard wall function approach where the wall shear stress is obtained by assuming a velocity profile near the wall. For laminar flows, a linear velocity profile is assumed and therefore, finite differences can be used in estimating wall shear stress as follows:

$$\tau_w = \mu \left. \frac{\partial u}{\partial y} \right|_w = \mu \frac{u}{y}. \tag{3.3.4–2}$$

Here, y is the normal distance of the first grid point from the wall, and u is the velocity at that point relative to the wall. As for turbulent flows, the velocity profile between the wall and the first grid point away from the wall is assumed to obey the following law of the wall:

$$u^+ = y^+ \qquad \text{for } y^+ < 11.5, \tag{3.3.4–3}$$

and

$$u^+ = \frac{u_\tau}{\kappa} \ln\left(Ey^+\right) \quad \text{for } y^+ > 11.5, \tag{3.3.4–4}$$

where y^+ and u^+ are defined as follows:

$$y^+ \equiv \frac{\rho y u_\tau}{\mu}, \tag{3.3.4–5}$$

and

$$u^+ = \frac{u}{u_\tau}. \tag{3.3.4–6}$$

The friction velocity, u_τ, is defined as

$$u_\tau = \left(\frac{\tau_w}{\rho}\right)^{1/2}, \tag{3.3.4–7}$$

and the experimentally determined constants, E and κ, have values of 9.0 and 0.4 respectively. Thus, from known y and u at the first grid point, u_τ is iteratively determined from the preceding equations.

The values for k and ε in the first cell adjacent to the wall are not determined from numerical integration of the k and ε equations, but are determined from semi-empirical relations. These relations, given below, are obtained from a Couette flow analysis of the momentum and turbulence equations assuming a logarithmic velocity profile.

$$k = \frac{u_\tau^2}{\sqrt{C_\mu}} \tag{3.3.4–8}$$

$$\varepsilon = C_\mu^{3/4} \frac{k^{3/2}}{\kappa y} \tag{3.3.4–9}$$

This leads to an important aspect of wall functions: wall functions are valid only if the first grid point is placed inside the logarithmic boundary layer as shown in Figure 3.3.

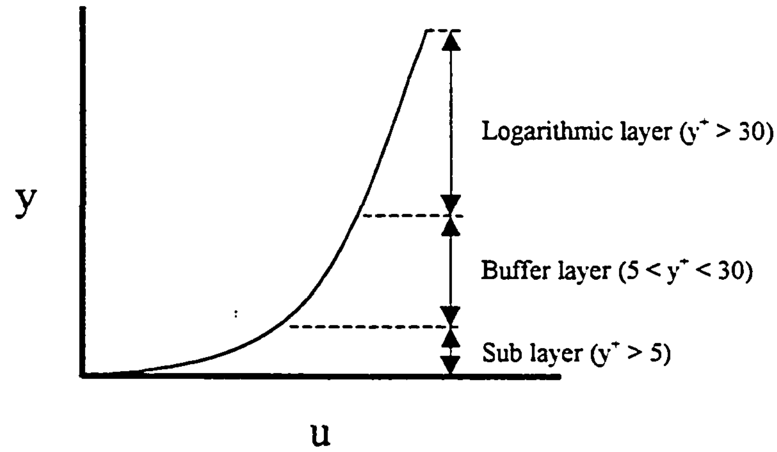

Figure 3.3: Schematic of near wall turbulent velocity profile depicting layers for locations of first grid points (CFDRC, 1993).

3.3.5 The RNG k–ε Model

This variation of the k–ε developed by Yakhot and Orszag (1986) uses a renormalization group (RNG) approach in which the smallest scales are systematically removed. The model currently employed by CFD-ACE is that of Yakhot et al.. (1992). The equations for k and ε have the same form as those of the standard k–ε model, Eqs. (3.3.3–1) and (3.3.3–2), but differ in the model coefficients. These are given below.

$$C_\mu = 0.085;\ C_{\varepsilon 2} = 1.68;\ \sigma_k = \sigma_\varepsilon = 0.7179$$

The coefficient $C_{\varepsilon 1}$ is given by:

$$C_{\varepsilon 1} = 1.42 - \frac{\eta\left(1 - \frac{\eta}{\eta_0}\right)}{1 + \beta\eta^3}, \qquad (3.3.5\text{–}1)$$

where $\eta_0 = 4.38$ and $\beta = 0.015$. The ratio of time scales for turbulence and mean strain rate, η, is given by:

$$\eta = \frac{Sk}{\varepsilon}, \tag{3.3.5-2}$$

where,

$$S = \sqrt{2S_{ij}S_{ji}}\ , \tag{3.3.5-3}$$

and, the rate of mean-strain tensor, S_{ij}, is defined as:

$$S_{ij} = \frac{1}{2}\left(\frac{\partial u_i}{\partial x_j} + \frac{\partial u_j}{\partial x_i}\right). \tag{3.3.5-3}$$

3.3.6 The *k*–ω Model

The k–ω model offered by CFD-ACE is based on the model of Wilcox (1991). Instead of a differential equation for ε, the second differential equation is developped in terms of the specific rate of turbulent dissipation, ω. The eddy viscosity in this model is defined by:

$$\nu_t = C_\mu \frac{k}{\omega}. \tag{3.3.6-1}$$

The transport equations for k and ω are:

$$\frac{\partial}{\partial x_j}\left(\rho u_j k\right) = \rho P - \rho\omega k + \frac{\partial}{\partial x_j}\left[\left(\mu + \frac{\mu_t}{\sigma_k}\right)\frac{\partial k}{\partial x_j}\right], \qquad (3.3.6\text{–}2)$$

$$\frac{\partial}{\partial x_j}\left(\rho u_j \omega\right) = C_{\omega 1}\frac{\rho P\omega}{k} - C_{\omega 2}\rho\omega^2 + \frac{\partial}{\partial x_j}\left[\left(\mu + \frac{\mu_t}{\sigma_\omega}\right)\frac{\partial \omega}{\partial x_j}\right]. \qquad (3.3.6\text{–}3)$$

The values of the parameters in the above equations are as follows:

$.C_\mu = 0.09$, $C_{\omega 1} = 0.555$, $C_{\omega 2} = 0.833$, $\sigma_k = 2.0$, $\sigma_\omega = 2.0$.

The boundary conditions for k and ω at wall boundaries are as follows:

$$k = 0 \quad \text{at} \quad y = 0, \qquad (3.3.6\text{–}4)$$

$$\omega = 7.2\frac{\nu}{y^2} \quad \text{at} \quad y = y_1, \qquad (3.3\text{–}5)$$

where y_1 is the normal distance to the wall from the center of the cell next to the wall (CFDRC, 1993).

3.3.7 The Low Re k–ε Model

The k–ε models previously described are of the high Re form and therefore require the use of wall functions. However, wall functions may not be as accurate in flows which include phenomena such as large separation, suction, blowing, heat transfer and relaminarization. This difficulty can be avoided by the use of low Reynolds number k–ε models. The k–ε equations of these models are modified to include the effect of molecular viscosity in the near wall regions and thus permit integration of the momentum, k, and ε equations all the way to the wall.

The particular version of the low Re k–ε model implemented by CFD-ACE is that of Chien (1982) and is given as follows:

$$\frac{\partial}{\partial x_j}\left(\rho u_j k\right)=\frac{\partial}{\partial x_j}\left(\left(\mu+\frac{\mu_t}{\sigma_k}\right)\frac{\partial k}{\partial x_j}\right)+\rho\left(P-\varepsilon-D\right) \qquad (3.3.7\text{–}1)$$

$$\frac{\partial}{\partial x_j}\left(\rho u_j \varepsilon\right)=\frac{\partial}{\partial x_j}\left(\left(\mu+\frac{\mu_t}{\sigma_\varepsilon}\right)\frac{\partial \varepsilon}{\partial x_j}\right)+C_{\varepsilon_1} f_1\frac{\rho P\varepsilon}{k}-C_{\varepsilon_2} f_2\frac{\rho\varepsilon^2}{k}+E \qquad (3.3.7\text{–}2)$$

$$\mu_t=C_\mu f_\mu\frac{\rho k^2}{\varepsilon} \qquad (3.3.7\text{–}3)$$

$$P=\nu_t\left(\frac{\partial u_i}{\partial x_j}+\frac{\partial u_j}{\partial x_i}-\frac{2}{3}\frac{\partial u_m}{\partial x_m}\delta_{ij}\right)\frac{\partial u_i}{\partial x_j}-\frac{2}{3}k\frac{\partial u_m}{\partial x_m}, \qquad (3.3.7\text{–}4)$$

where:

$$f_\mu = 1 - \exp(-0.0115 y^*), \tag{3.3.7–5}$$

$$f_2 = 1 - 0.22 \exp\left[-\left(\frac{\mathrm{Re}_t}{6}\right)^2\right], \tag{3.3.7–6}$$

$$D = \frac{2\nu k}{y^2}, \tag{3.3.7–7}$$

and

$$E = -2\nu\left(\frac{\varepsilon}{y^2}\right)\exp\left(-0.5 y^*\right). \tag{3.3.7–8}$$

The model parameters appearing in the above expressions are specified as:

$$C_\mu = 0.09;\ C_{\varepsilon 1} = 1.35;\ C_{\varepsilon 2} = 1.8;\ \sigma_k = 1.0;\ \sigma_\varepsilon = 1.3; f_1 = 1.0.$$

As the wall shear stress is calculated from finite differences for this model, the first grid point should be within the laminar sub-layer shown in Figure 3.3.

3.4 Boundary Conditions

In this section, the specification of the model boundary specification shall be discussed.

3.4.1 Inlet Boundary Conditions

There are two types of inlet boundaries available in CFD-ACE: specified mass flowrate and specified total pressure. In the present study, a design criteria of the experiments to be simulated was a fixed flowrate of 1 L/s. Therefore the specified mass flowrate was employed. The specified mass flowrate requires the specification of the three velocity components u, v and w, along with the turbulent quantities k and ε. It was decided that, in order to reduce end effects and aid in convergence, inlet profiles should be specified instead of constant values at all nodes on the inlet plane.

Profiles for the turbulence parameters k and ε for confined (internal) or semi confined (boundary layer, etc.) flows and in absence of detailed experimental data can be given by (fdi, 1993):

$$k = C_\mu^{1/2}\left(l_m \frac{du}{dy}\right)^2, \tag{3.4–1}$$

and

$$\varepsilon = C_\mu k^2 \left(l_m^2 \left|\frac{du}{dy}\right|\right)^{-1}. \tag{3.4–2}$$

Here, y denotes the normal coordinate axis to the wall, u is the streamwise velocity profile at the inlet plane, and l_m is a mixing length expression. Provided that the inlet is placed sufficiently far from flow obstructions, u can be approximated by the following power-law profile (fdi, 1993):

$$\frac{u}{u_r} = \left(\frac{y}{\delta}\right)^{1/h}, \tag{3.4–3}$$

where u_r is the magnitude of the velocity along the centerline of the pipe or channel, δ is the characteristic width, and h is a Reynolds number dependant parameter that can be obtained by interpolating from the data in the table below. Note however that here the characteristic width is the inlet pipe radius.

Table 3.1: Correlation of the power law exponent parameter, h, with the Reynolds number (fdi, 1993).

$\frac{\rho u_r \delta}{\mu}$	h
4×10^3	6.0
2.3×10^4	6.6
1.1×10^5	7.0
1.1×10^6	8.8
2×10^6	10
3.2×10^6	10

The mixing length expression, l_m in Equations (3.4–1) and (3.4–2) was obtained by curve fitting the data in Table B.1, found in Appendix B. The resulting correlation takes the following form:

$$y = a + bx^2 + c\exp(x) + d\sqrt{x}, \tag{3.3–4}$$

with an r^2 of 0.9988. The correlation parameters were found as follows:

$$a = -0.25295592;\ b = -0.35024659;\ c = 0.2529561;\ d = 0.076542158.$$

3.4.2 Exit Boundary Conditions

There are three types of exit boundaries that can be specified in CFD-ACE: 1) fixed pressure exit boundaries intended for subsonic flow, 2) extrapolated exit boundaries intended for supersonic flow conditions, and 3) the combined condition exit boundaries, intended for mixed supersonic and subsonic conditions.

In this study, the option for fixed pressure exit boundary for subsonic flow was selected. This boundary condition applies a fixed pressure of zero at exit boundary. Since fixed pressure outlet boundaries may also allow inflow, it is also important to prescribe realistic boundary values for the three velocity components and turbulence quantities. If at any time during this solution procedure inflow at the exit arises, these prescribed values would then be automatically incorporated into the domain. In this case realistic boundary conditions would also involve the specification of a fully developed flow profile. However, upon consultation with the CFD-ACE support personnel, it was decided that this amount of detail would not be necessary as the flow conditions at the outlet are so predominantly uni-directional that the chances of inflow occurring are negligible. The actual values chosen would have no influence on the solution.

Therefore, it was sufficient that a uni-directional flat velocity profile be assigned and that the values for w, k and ε should only be roughly of the same order of magnitude. Thus, the following values were used:

$$u = 0;\ v = 0;\ w = 0;\ k = 0.001;\ \varepsilon = 0.00075.$$

3.4.3 Wall Boundary Conditions

Wall boundaries are specified as the typical no slip and no flow boundary conditions.

3.4.4 Symmetry Boundary Conditions

As mentioned previously, it was necessary to take advantage of the symmetry of the header. The symmetry planes, as shown in Figure 3.2, all receive symmetry boundary conditions. In CFD-ACE this entails setting the velocity normal to the boundary to zero and, for all variables, setting the gradient normal to the boundary to zero.

Chapter 4.0

Solution Method

This section describes in detail the procedure used to perform the study. It describes the steps taken from the selection of the CFD package to the production of the modeled system.

4.1 *Selection of CFD Package*

At the onset of this study it was established that, due to the complexity of the physics involved with turbulent flow, a commercial computational fluid dynamics (CFD) software package would be employed to simulate flow within the tubular membrane module header. By the end of the study, two CFD packages had been tested: FIDAP from Fluid Dynamics International (fdi) and CFD-ACE+ from CFD Research Corporation (CFDRC).

Initially, the study began with FIDAP, which is based on finite element methods (FEM). This software was made available to the graduate students through Tesla, an IBM Risc 6000/390 server, equipped with 128 Mb of RAM. Tesla is a shared server for engineering graduate research.

The initial approach taken with FIDAP was to model the whole module header. However, true convergence was never obtained from this initial modeling attempt using FIDAP. Many problems were encountered, mostly due to computer resources. The problem itself, full 3-D modeling of turbulent flow in a complex geometry, was extremely resource intensive. When this was combined with a multi-user server on which several others were submitting FIDAP sessions, it resulted in system overloads and eventually system “crashes”. Another problem that presented itself with the multi-user system was that each user was allotted a limitted amount of disk space. However, when a FIDAP simulation is running, it requires large amounts of disk space for its run-time files. If this disk space is not available, the run is aborted.

It became evident that the solution approach had to be reconsidered. Seeing that the main difficulties stemmed from the use of the multi-user server, it was decided to move to a single user workstation. This would lead to more predictable run-times, a more stable environment, and assure available resources. The project was moved to an HP Apollo Series 7200 workstation equipped with 48 Mb of RAM.

Several packages were researched and information solicited from their manufacturers. Upon careful deliberation, it was decided that the package CFD-ACE+ from CFDRC (Hunstville, Alabama) would be purchased. There were several reasons why this package was chosen over the others, including FIDAP. First and foremost, this package's geometry and grid generator, CFD-GEOM , was very sophisticated. It had many advanced CAD tools for the creation of complex geometries, which greatly reduced the generation time (lengthy geometry creation times and primitive CAD tools were a serious problem with FIDAP when dealing with complex 3-D geometries). Also, it offered very good control of grid generation and grid distribution, which led to high quality grid generation.

4.2 CFD-ACE + and Body Fitted Coordinates

CFD-ACE+ is based upon the finite volume method of discretization. One fundamental requirement of this formulation is that the grid generated for the discretization of the computational domain be orthogonal. This would normally seriously limit the types of geometries that could be modeled, since many problems of engineering interest consist of curved boundaries in the flow domain. However, this problem is overcome by CFD-ACE's implementation of a 'Body-Fitted Coordinate' (BFC) system. In general, systems which require definition in BFC systems are those in which grid lines in the same direction are not parallel and those in different directions are not perpendicular (CFDRC, 1993).

Mathematically speaking, a BFC system can be defined as a coordinate transformation from the physical domain to an orthogonal, computational domain (CFDRC, 1993). To illustrate this, it would be useful to consider a 2-D BFC grid and its transformed, curvilinear counterpart, as depicted in Figure 4.1. The cell indices, I and J, vary along the ξ and η coordinate lines, respectively. Also, there is a one-to-one correspondence between (ξ,η) and (I,J) (CFDRC, 1993).

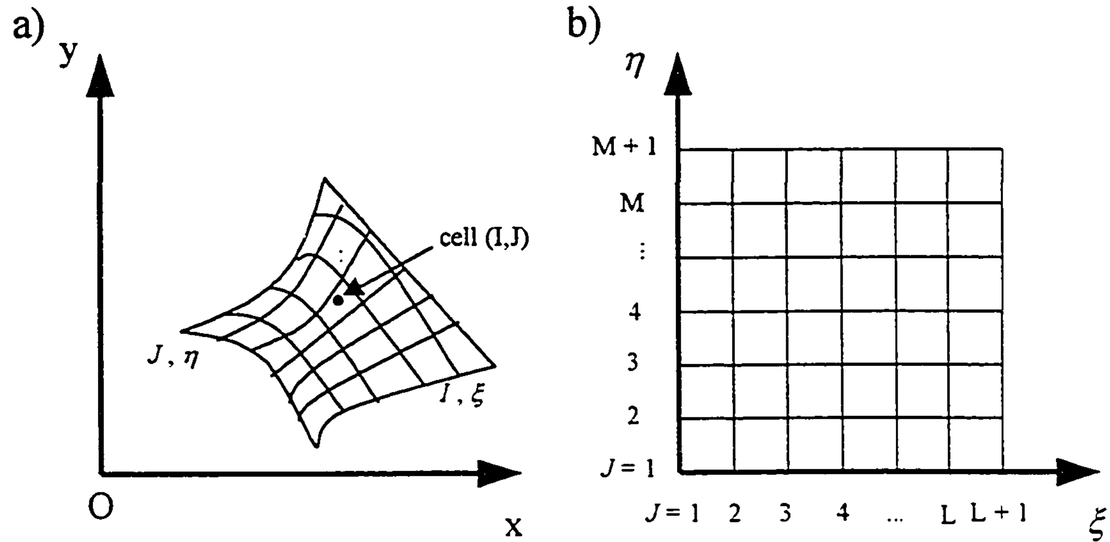

Figure 4.1: Figure depicting a hypothetical coordinate transformation from a) the physical domain to b) the computational domain (CFDRC, 1993).

In the next few paragraphs a brief mathematical description of the BFC system will be given followed by the BFC representation of common differential operators that appear in the governing equations of fluid flow.

Similar to the situation depicted in Figure 4.1, for a given 3D flow problem, each point in the flow domain can identified by (x,y,z), (ξ,η,ζ), or (I,J,K). Generally the coordinate transformations can be expressed as follows (CFDRC, 1993):

$$\left.\begin{array}{l}\xi=\xi(x,y,z), \eta=\eta(x,y,z), \zeta(x,y,z) \\ x=x(\xi,\eta,\zeta), y=y(\xi,\eta,\zeta), z=(\xi,\eta,\zeta)\end{array}\right\} \qquad (4.2\text{-}1)$$

To facilitate tensor notation while presenting the basic relations between the Cartesian and BFC systems, (ξ_1,ξ_2,ξ_3) will be used to denote (ξ,η,ζ). In a BFC coordinate system, the covariant base vectors, $\bar{\varepsilon}_j$, are defined as base vectors along the ξ_j coordinate line, and are given by the following (CFDRC, 1993):

$$\bar{\varepsilon}_j = \frac{\partial \bar{r}}{\partial \xi_j}, \tag{4.2-2}$$

where $\bar{r}$ is the position vector defined by:

$$\bar{r} = x\bar{i} + y\bar{j} + z\bar{k}, \tag{4.2-3}$$

and the subscript j takes the values of 1,2, and 3. The contravariant base vectors, $\bar{\varepsilon}^j$, are defined as base vectors normal to the surface formed by $\bar{\varepsilon}_i$ and $\bar{\varepsilon}_k$ where index $i \neq j \neq k$. The contravariant vectors are given by the following expressions (CFDRC, Theory Manual, 1993):

$$\bar{\varepsilon}^1 = \frac{\bar{\varepsilon}_2 \times \bar{\varepsilon}_3}{J}, \bar{\varepsilon}^2 = \frac{\bar{\varepsilon}_3 \times \bar{\varepsilon}_1}{J}, \text{ and } \bar{\varepsilon}^3 = \frac{\bar{\varepsilon}_1 \times \bar{\varepsilon}_2}{J}, \tag{4.2-4}$$

where J is the Jacobian defined as:

$$J = (\bar{\varepsilon}_1 \times \bar{\varepsilon}_2) \cdot \bar{\varepsilon}_3 \tag{4.2-5}$$

These base vectors for a 2-D BFC system are depicted in Figure 4.2.

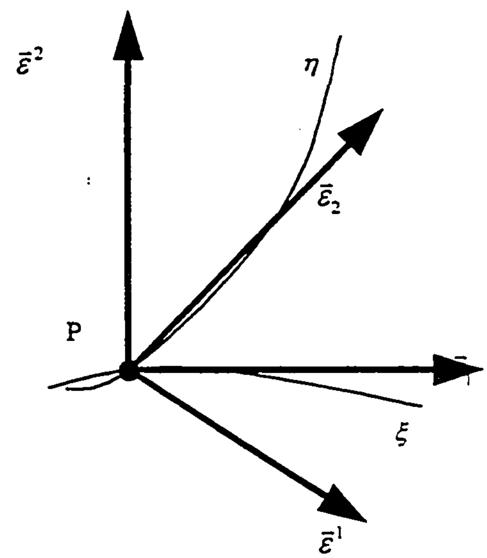

Figure 4.2: Covariant and Contravariant base vectors for a hypothetical 2-D BFC system (CFDRC, 1993).

By definition, the covariant and contravariant base vectors satisfy the following relationship:

$$\vec{\varepsilon}_i \cdot \vec{\varepsilon}^j = \delta_{ij} \qquad (4.2\text{–}6)$$

where δ_{ij} is the Kronecker delta. It should also be noted that $\vec{\varepsilon}_j$ and $\vec{\varepsilon}^j$ are not necessarily unit vectors. The covariant unit vectors can be defined as follows:

$$\vec{e}_j = \frac{\vec{\varepsilon}}{h_j}, \text{ where } h_j = |\varepsilon_j| = \sqrt{\left(\frac{\partial x}{\partial \xi_1}\right)^2 + \left(\frac{\partial y}{\partial \xi_2}\right)^2 + \left(\frac{\partial z}{\partial \xi_3}\right)^2}, \qquad (4.2\text{–}7)$$

and the contravariant unit vectors can be obtained from Equation (4.2–4) (CFDRC, 1993).

Some of the differential operators that commonly appear in fluid flow equations will be presented in BFC form (CFDRC, 1993):

Gradient:

$$\nabla f = \frac{1}{J}\frac{\partial}{\partial \xi_k}\left(J\varepsilon^k f\right) \tag{4.2–8}$$

Divergence:

$$\nabla \cdot \vec{V} = \frac{1}{J}\frac{\partial}{\partial \xi_k}\left(J\varepsilon^k \cdot \vec{V}\right) \tag{4.2–9}$$

Curl:

$$\nabla \times \vec{V} = \frac{1}{J}\frac{\partial}{\partial \xi_k}\left(J\varepsilon^k \times \vec{V}\right) \tag{4.2–10}$$

Laplacian:

$$\nabla^2 f = \frac{1}{J}\frac{\partial^2}{\partial \xi_i \partial \xi_j}\left(J\, f\, \varepsilon^i \cdot \varepsilon^j\right) \tag{4.2–11}$$

4.3 Grid Generation

In numerical analysis, the solution to the governing equations is approximated by discretizing the physical domain. Particularly, in the finite volume approach employed by CFD-ACE, the flow domain is discretized by dividing it into a discrete number of cells or finite volumes. The governing equations are then numerically integrated over each finite volume. This discretized representation of the computational domain is termed "the grid" and the procedure of obtaining this subdivided domain is termed "grid generation". Therefore, a properly structured grid in terms of density and distribution is an integral aspect of numerical simulations.

There are two approaches to grid generation available in CFD-GEOM, the grid generation module of CFD-ACE+: 1) the structured grid generation approach and 2) the unstructured generation approach. A 3-D grid is considered to be a structured grid if the three coordinate directions can be identified by three distinct grid lines. That is, a 3-D grid is structured if a single (I,J,K) index can be used to identify a cell or grid point. Thus, structured grids are inherently composed of quadrilateral cells. However, unstructured grids, as the term implies, bear none of these restrictions. 3D grids can be composed of tetrahedral and prism or wedge type elements. These elements can be combined in non-uniform and varied patterns to achieve the desired grid. The advantages of unstructured grids are that there is much greater control over grid element spacing and that more complex geometries can be meshed. Although CFD-GEOM can generate these types of grids, CFD-ACE, the actual numerical solver, is incapable of implementing these types of grids. This ability, however, is under development for a future release. The only alternative, therefore, was to proceed with structured grids in this study.

CFD-GEOM'S implementation of structured grid generation was still capable of producing sophisticated grids for quite complex geometries, while still maintaining some degree of control over the placement and distribution of grid cells. This was due to CFD-

GEOM's ability to produce a multi-domain grid, which is also implemented by CFD-ACE. Construction of a single domain structured grid may be an extremely difficult task for even moderately complex geometries. However, with the multi-domain approach, it is possible to subdivide the computational domain into sub-domains or zones for which a structured grid is much more easily constructed. Not only does this allow flexibility in the types and complexity of the geometries for which grids are produced, but, it also allows greater flexibility in grid clustering in each domain and hence can offer significant storage and computational benefits.

The strengths of the multi-domain approach can be best demonstrated by way of a simple 2-D example of the flow over a backward-facing step. Attempting to grid the computational domain using a single structured grid would lead to a highly skewed region behind the step. This is depicted in Figure 4.3 a). However, if the flow-domain is divided into two domains, smooth and uniform grids can easily be generated in each domain. This is depicted in Figure 4.3 b). From this figure, it can also be seen that the number of grid cells on opposite sides of a grid need not be the same, but each coarser grid cell vertex must coincide with a finer grid cell vertex. This ensures conservation of flow quantities.

a)

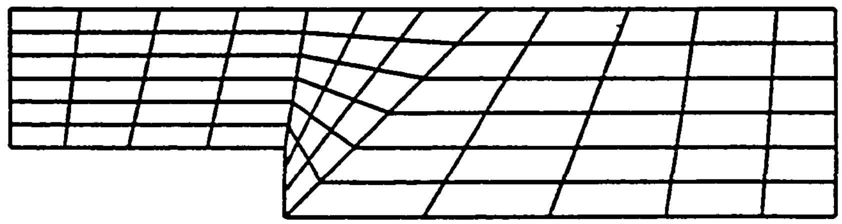

b)

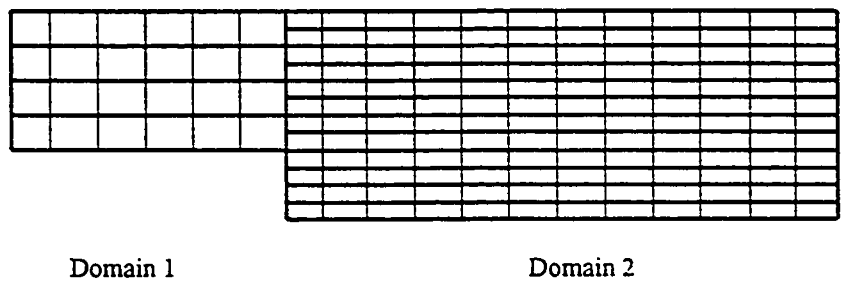

Figure 4.3: Schematic diagram of structured grids for a backwards facing step using: a) the single-domain approach, and b) the multi-domain approach (CFDRC, 1993).

The first step in generating a grid is modeling the geometry. At first glance, this task would seem rather straightforward. However, when dealing with complex geometries, the problem quickly becomes evident: deciding on the amount of geometric detail necessary to adequately solve the problem in question. Too much geometric detail could result in a gridding nightmare. Also, the greater the detail, the greater the demand for computer resources and the longer the computational time. CFDRC has several recommendations on deciding the geometrical detail of the model. These recommendations are listed below (CFDRC, 1996):

1. If the feature to be added is not suspected to have an impact on the desired results, it should be omitted.
2. A physical model should be used to simulate a feature where possible. For example, porous media can be simulated as a momentum resistance.
3. If the feature is small compared to the boundary layer thickness it can be eliminated.
4. If the time and computing constraints required to resolve this feature cannot be afforded, then again it should be omitted.
5. Any symmetry in the geometry should be taken advantage of as it can greatly reduce the size of the domain.

After reflecting on the approach taken with FIDAP in light of these recommendations, it was decided that the symmetry of the header would be used to reduce the size of the domain. Even though the study was moved off of the multi-user platform, the new workstation had less physical resources and any savings on resources were crucial. At this point, the figure depicting the symmetry of the header is repeated as Figure 4.4. As we again see from this figure, the model header to be studied contains a ten-fold symmetry as there are ten symmetry sub-units contained in the whole system. This would reduce system requirements by an order of magnitude. Also the numerical simulation of the reduced problem becomes much more stable as there are fewer volumes over which to integrate.

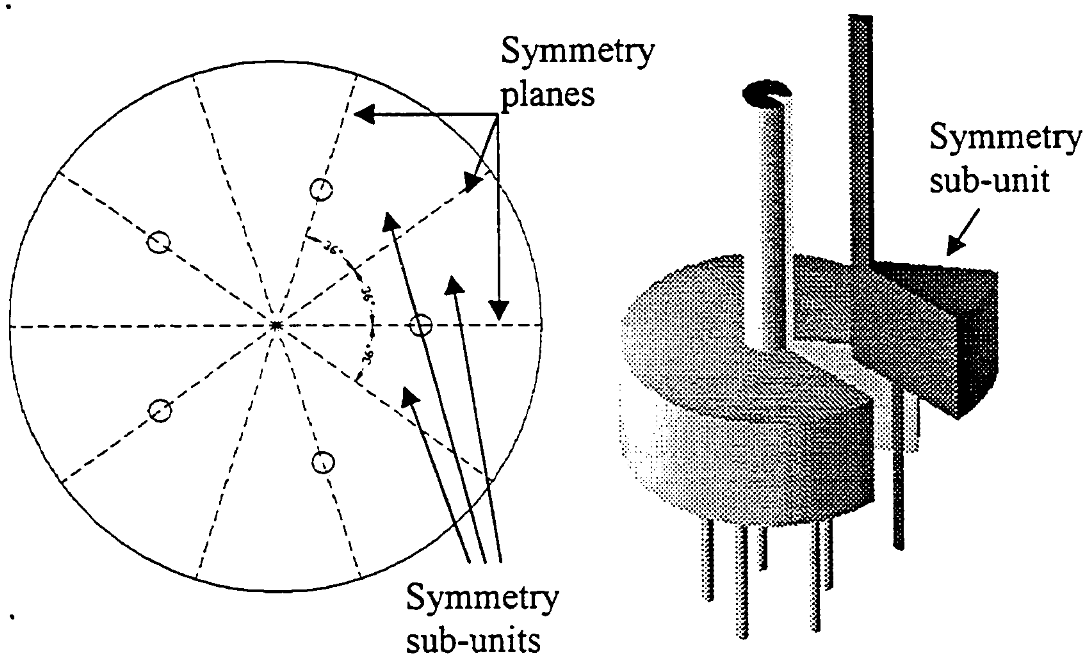

Figure 4.4: Ten-fold symmetry in the model header.

The first step in producing a finished grid is to model the finalized geometry of the system at hand. This task is performed in the geometry sub-module of CFD-Geom titled Geom, which offers many advanced CAD tools that facilitate the simple production of very complex geometries.

The model of the geometry provides the framework upon which the grid is to be built. Structured grid generation is performed within the CFD-Geom sub-module, S-Grid. Structured grid generation can be a very complex procedure, often requiring the return to Geom for re-evaluation of the division of the geometry in order to obtain a suitable grid structure. Therefore, only a brief description of the elements and procedures required for the production of a grid will be given. A detailed description of Grid assessment and the reasoning involved in geometry division in order to obtain a suitable grid is found in the next section, Section 4.4 and in the Results and Discussion section.

The procedures involved in the generation of a 3-D structured grid can be grouped into three main tasks: 1) identifying geometry elements as edges, 2) combining these edges to create faces, and 3) combining these faces to form a grid block.

An "edge" forms the basic grid generation element: it establishes the grid density and distribution. Edges can be defined along one or more connected geometric lines or curves. A "face" forms the basic surface grid generation element. Each face must consist of four connected edge sets, where one edge set can consist of one or more edges. This requires that opposite edge sets contain the same number of grid points. A "block" forms the basic element of volume grid generation. Each block is composed of six face sets, where one face set can consist of one or more faces. Thus, a requirement is that opposing face sets contain the same number of elements. The end result is a collection of one or more blocks composing a single- or multi-domain grid.

4.4 Grid Finalization and Evaluation

As mentioned in the previous section, grid generation for a complex 3-D geometry can be a very intricate and difficult procedure. It is not the individual tasks of defining edges, faces, and blocks that pose the difficulty, but determining how the computational domain should be subdivided and which geometrical elements should be combined for use as edges, *etc*. Also, deciding upon a method for evaluating the grid once obtained in order to assess its performance was found to be a difficult task when dealing with complex 3-D geometries. The main problem was that, as the physical domains were altered to obtain alternate grids, the physical location of the volumes were also altered. The visualization tools of CFD-ACE+ do not have the capability to transcend these domain divisions. It was not possible to extract data across domains. Also, as the physical location of each node was altered, obtaining values for a given variable at the same spatial location was not possible. Another factor was that for each incarnation of the grid, the degree of convergence obtained was different. Again this made it very difficult to compare their respective results. Actually, as shall be discussed later in this section, it was often very difficult to obtain a sufficiently converged solution.

After much deliberation, and in light of the fact that obtaining a converged solution was so difficult, it was decided that the most reliable criterium for the evaluation of a grid's performance was to examine and compare the ratio of the initial to final residuals for each prospective grid. In CFD-ACE, the residuals for each degree of freedom are obtained by calculating a residual at each control cell by taking the difference of the two sides of the discrete equation for that cell. These residuals are then summed over all the cells in order to obtain a single global residual. These residuals are not normalized and therefore, CFDRC recommends that, in order to consider a solution converged, the reduction in the ratio of the residuals be four to five orders of magnitude.

4.5 Solution Parameters

CFD-ACE offers a variety of solution options to customize the solution algorithm for a more accurate simulation of the problem in question, or to aid the convergence of the solution. These options, and the choices made, will be described briefly below. The actual final quantities employed are tabulated in Table 4.1.

Table 4.1: Solution parameters used in the simulations.

Solution Parameter	Values			
	$\alpha = 0°$	$\alpha = 30°$	$\alpha = 45°$	$\alpha = 55°$
Relaxation Factors	$u, v, w - 0.3$ $k, \varepsilon - 0.2$ $p, \rho, \mu - 1.0$	$u, v, w - 0.3$ $k, \varepsilon - 0.2$ $p, \rho, \mu - 1.0$	$u, v, w - 0.5$ $k, \varepsilon - 0.4$ $p, \rho, \mu - 0.7$	$u, v, w - 0.5$ $k, \varepsilon - 0.4$ $p, \rho, \mu - 0.7$
Multi-domain Initial Cond.	No	Yes	Yes	Yes
Continuity Iterations	1	1	1	1
Whole-I Solver	u, v, w, k, ε	u, v, w	u, v, w	u, v, w
Whole-I Iterations	$u, v, w, k, \varepsilon - 10$	$u, v, w - 10$	$u, v, w - 50$	$u, v, w - 50$
CGS Solver	pp	pp, k, ε	pp, k, ε	pp, k, ε
CGS Iterations	$pp - 500$	$pp - 500$ $k, \varepsilon - 500$	$pp - 1200$ $k, \varepsilon - 1000$	$pp - 1200$ $k, \varepsilon - 1000$

4.5.1 Spatial Differencing

The spatial differencing option allows the choice of differencing schemes for the calculation of the convective term in the transport equations. CFD-ACE offers the following four principal options: 1) the first-order upwind scheme, 2) the central differencing scheme, 3) the second-order upwinding scheme and 4) the Osher-Chakravarthy scheme. In addition, CFD-ACE allows the combination of the first-order upwinding scheme with any of the other schemes, which are all higher-order schemes, through a blending factor. This factor allows one to specify the percentage of the differencing that is first-order upwinded. This option allows a solution of greater accuracy than that using first-order upwinding when convergence with a higher-order model alone is not possible (CFDRC, 1996).

First order upwinding was used for all simulations, as it is the most stable of schemes available. It was recommended that higher-order schemes be attempted only after a fully converged solution with the first-order scheme was obtained (CFDRC, 1996).

4.5.2 Linear Equation Solvers

Once the set of discretized equations for a variable has been assembled, it must be solved using a linear equation solver. CFD-ACE employs iterative equation solvers as they are more economical in terms of computer memory requirements than are direct solvers which require the assembly and storage of the full coefficient matrix for the system in question (Gerald and Wheatley, 1989). Specification of which solver is to be employed and the number of iterations performed on the given dependent variable is established through the Solvers and Solver Iterations menu. There are two types of linear equation solvers employed by CFD-ACE: 1) the whole-field solvers based upon the Strongly Implicit Procedure (SIP), and 2) the Conjugate Gradient Squared algorithm (CGS). Three versions of the whole-field solver exist: 1) whole-I, 2) whole-J, and 3) whole-K. These differ by way of being biased in one of the three the grid coordinates I, J, or K. The solver iterations parameter specifies the number of iterations performed by the iterative solver for each dependant variable. For the CGS solver, the usual practice is to specify a very large number for the solver iterations as the solver stops executing upon convergence. For the whole field solvers only a few iterations need be specified (usually in the range of 10 to 50 for large complex problems as recommended by CFDRC) (CFDRC, 1996).

After many trials, and consideration of the recommendations made by CFDRC (CFDRC, 1996), it was established that for the 30°, 45°, and 55° angle cases, the whole-I solver would be implemented for the solution for u, v, w, while the CGS solver would be used for the pressure correction, pp, k, and ε. For the 0° angle case, the CGS solver would only be used for the variable pp.

4.5.3 Solution and Continuity Iterations

The solution and continuity iteration parameters specify the number of complete solution iterations performed and the number of iterations performed around the continuity equation respectively. The number of solution iterations required is established by the desired drop in residuals as described in the previous section. It is therefore problem dependent.

The number of continuity iterations specifies the number of iterations performed around the solution of the mass balances and the pressure correction equations. It is recommended that the number of iterations be increased from the default value of one, and be specified only for compressible flows, or when a highly skewed grid BFC grid is present (CFDRC 1996). Therefore after a few trial runs it was decided that the number of continuity equations would be specified as one for all simulations, as a greater number had negligible effect on the results and did not justify the drastic increase in simulation time.

4.5.4 Under-Relaxation

Under-relaxation is used to provide constraints on the updates of the dependent variables between successive iterations in order to aid in convergence. There are two different forms of under-relaxation used in CFD-ACE: 1) inertial under-relaxation for the dependent variables u, w, k, and ε, and 2) linear relaxation for the auxiliary variables ρ, p, and μ. It should be noted, however, that in CFD-ACE's implementation of under-relaxation, for inertial relaxation, factor values of 0.0 imply no under-relaxation while values greater than 0.0 apply increasing under-relaxation. Whereas, for linear relaxation, factors of 1.0 imply no under-relaxation and 0.0 implies maximum under-relaxation (CFDRC, 1996).

Initially, the guidelines established by CFD-ACE were followed for the selection of these relaxation factors, and were subsequently modified by trial and error to achieve better convergence. Guidelines, for incompressible turbulent flow, are listed in Table 4.2.

Table 4.2: Relaxation factor recommendations (CFDRC, 1996).

	Inertial		Linear		
Problem Type	u,v,w	k,ε	ρ	P	μ
Incompressible Turbulent flow	0.2-0.6	0.2-0.4	1.0	1.0	1.0-0.3

4.5.5 Initial Conditions

CFD-ACE allows the specification of initial conditions for individual domains for all dependant variables. These initial conditions are merely an initial guess for the particular dependant variable for all cells in a computational domain, and do not influence the final solution, although they can have a large influence on the solution's path to convergence (CFDRC, 1996). This approach was found to be extremely useful, especially when combined with the multi-domain approach to grid generation. In essence, this enabled the specification of different initial conditions in each domain. Therefore, the solution stability was somewhat increased as each domain contained similar predominant hydrodynamics, and appropriate starting values could be specified.

The method of obtaining representative initial conditions was by examining the solution to a previously simulated geometry. The 0° angle results were used to approximate a uniform set of initial conditions for the 30° angle case, which was in turn used to specify initial condition values for the 45° angle case, *etc*. Initial conditions for the 0° angle case were kept to the default value of zero for all dependant variables.

Chapter 5.0

Results and Discussion

5.1 Grid Generation and Convergence

Generating a suitable grid for a complex, curvilinear, three-dimensional geometry was found to be anything but the trivial task assumed at the onset of this study. Rather, it was found to be one of the most crucial aspects to successfully modeling such complex flow geometries. Note: all grids in this section were evaluated using the Low Re $k-\varepsilon$ turbulence model.

The first of the 3 cases to be modeled was the configuration with $\alpha = 0°$. This case also happened to be simplest geometrically as it did not contain the conical entrance to the outlet tube. The preliminary approach to producing a grid for this domain was to examine the physical aspects of the symmetry unit to be modeled in light of the restrictions to structured grid generation: i.e., each face must have four logical sides, opposing face grids must be topologically similar, *etc*. It was obvious that the geometry was composed of 3 distinct components: 1) the inlet tube, 2) the expansion chamber or header, and 3) the outlet pipe. The geometry to be modeled with the three distinct components labeled is shown in Figure 5.1. Logically then, it was decided that the model geometry should also be divided into the same 3 domains. Also, greater stability would then be expected, as each domain also defines a region in which the predominant flow characteristics are similar. The next issue to address was that the pie-slice shaped symmetry unit is inherently three-sided. Therefore, to create the face, a logical fourth side must be somehow obtained. After consultation with the support experts at CFDRC,

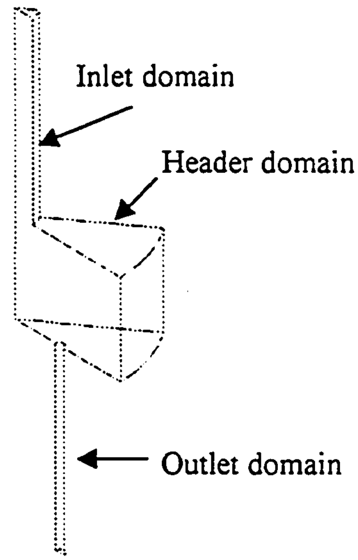

Figure 5.1: Geometry with $\alpha = 0°$ and with labeled domains.

it was decided that a fourth side could be generated by approximating the actual geometry by one that replaces the absolute apex of the pie-slice wedge with a miniscule plane of symmetry. The location and nature of this side is depicted in Figures 5.2 a) and b). Figure 5.2 a) shows the location of this symmetry plane in the geometry and Figure 5.2 b) shows a zoomed in view to present it in greater detail. The radius describing the cylinder surface was set to 0.0005 m. When contacted, the CFDRC support staff stated that this type approximation is often used successfully in CFD. Figure 5.2 a) also shows the other modifications that were necessary to produce a suitable grid: one extension line extending from the apex to the outlet tube and another from the outlet tube to the wall. It should be understood that these extension lines do not further divide the whole geometry into more than the three domains described above. They are simply used to create more faces, which are later combined to form the set of bottom faces in the header domain. This was necessary to avoid skewed elements at the corners of the outlet tube. This approach finally produced what was considered to be acceptable drops in residuals.

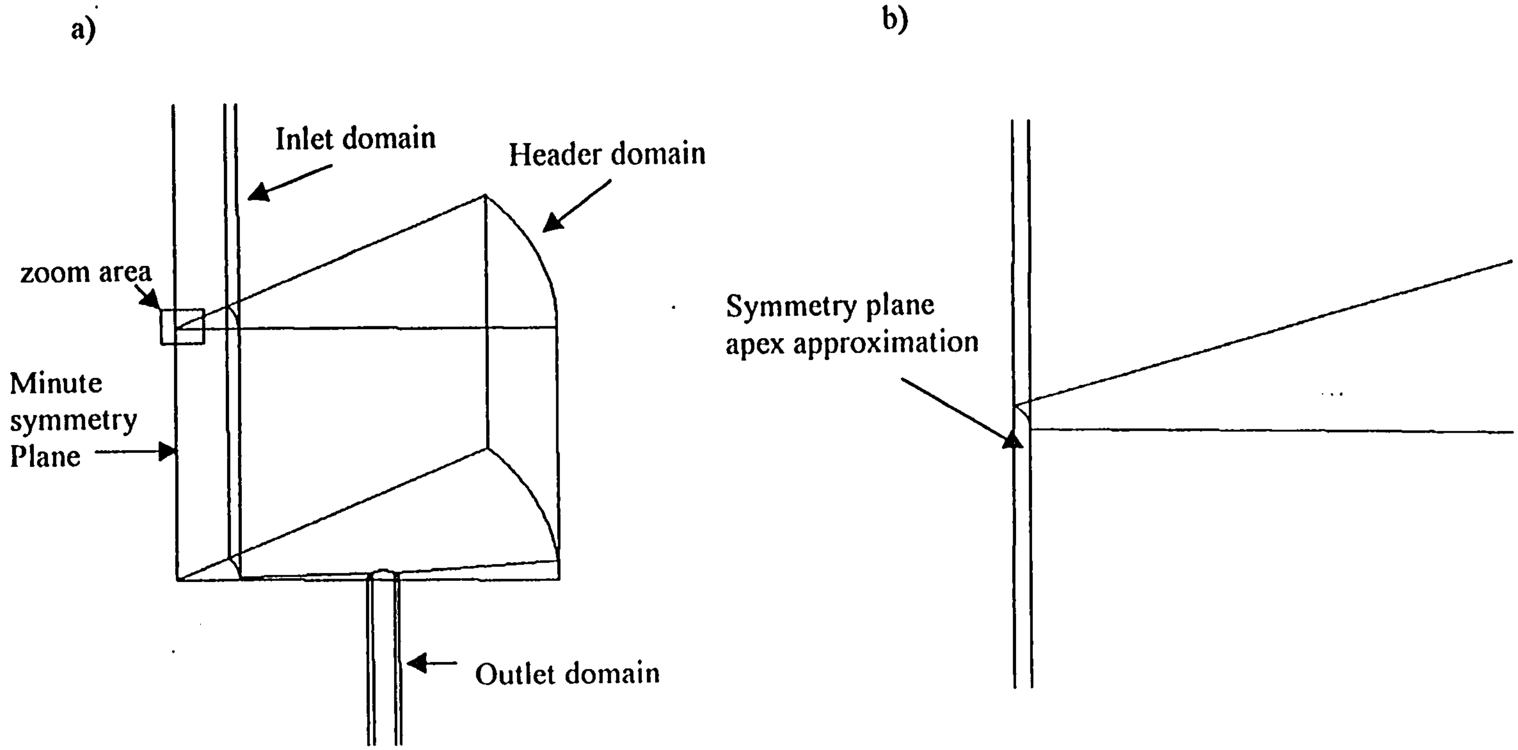

Figure 5.2: Geometry of the model with $\alpha = 0°$ showing a) the main components and the location of the symmetry plane approximation, and b) zoom area providing a close-up of the symmetry plane.

Figure 5.3 a) shows a cross-section of the final grid along the bottom of the header domain. Again, as mentioned earlier, discussion of the residuals of all cases will be left to the end of this section.

Next, the geometry with $\alpha = 30°$ was modeled using the same technique as for the $\alpha = 0°$ case with the following exception: a fourth domain was defined consisting of the conical entrance to the outlet tube. Figure 5.4 shows a screen capture of this model with the domains labeled, and Figure 5.2 b) shows a cross-section of the final grid along the bottom of the header domain. It should be noted that the method of using extension lines for controlling grid quality was also used for the $\alpha = 30°$ case. This type of grid also led to the successful completion of the 30° case. It should be noted, however, that some fine-tuning of the simulation parameters was necessary. The most crucial modification was the adaptation of the initial conditions to be domain specific. This and other solution techniques available to aid in convergence were discussed in Section 4.5.

This technique was not as successful when further applied to the case where α = 45°. Figure 5.5 shows the geometry of the model and a cross-section of the grid along the bottom of the header domain, respectively. As can be seen from Figure 5.5 a), a different procedure was necessary for the subdivision of the bottom face of the header. The drop in residuals obtained from this approach was unacceptable even after attempting to improve the convergence by modifying some of the solution parameters, such as: various linear equation solvers, relaxation factors, domain specific initial conditions, etc.

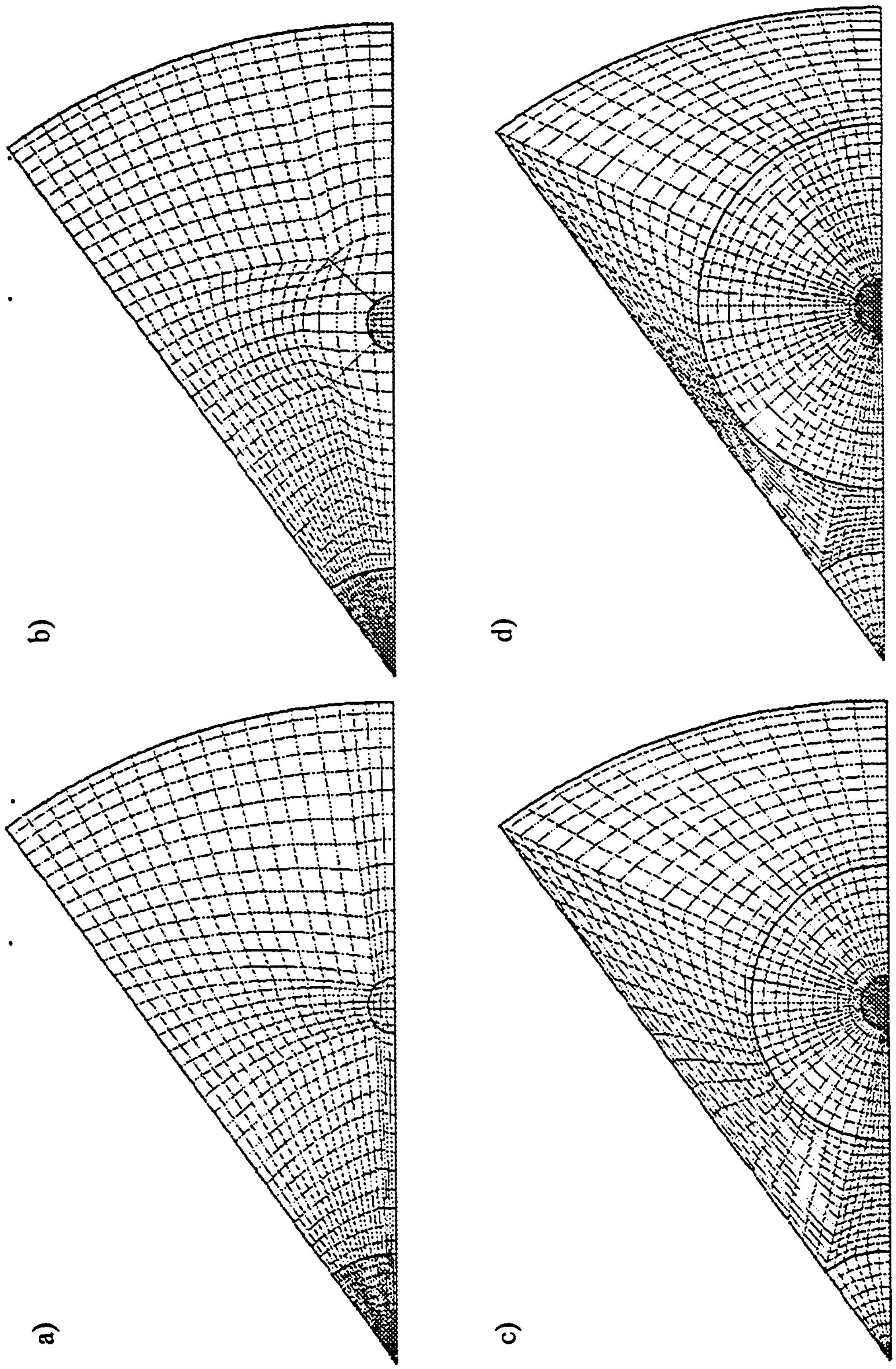

Figure 5.3: Cross-section of model grid for a) $\alpha = 0°$, b) $\alpha = 30°$, c) $\alpha + 45°$, and d) $\alpha = 55°$

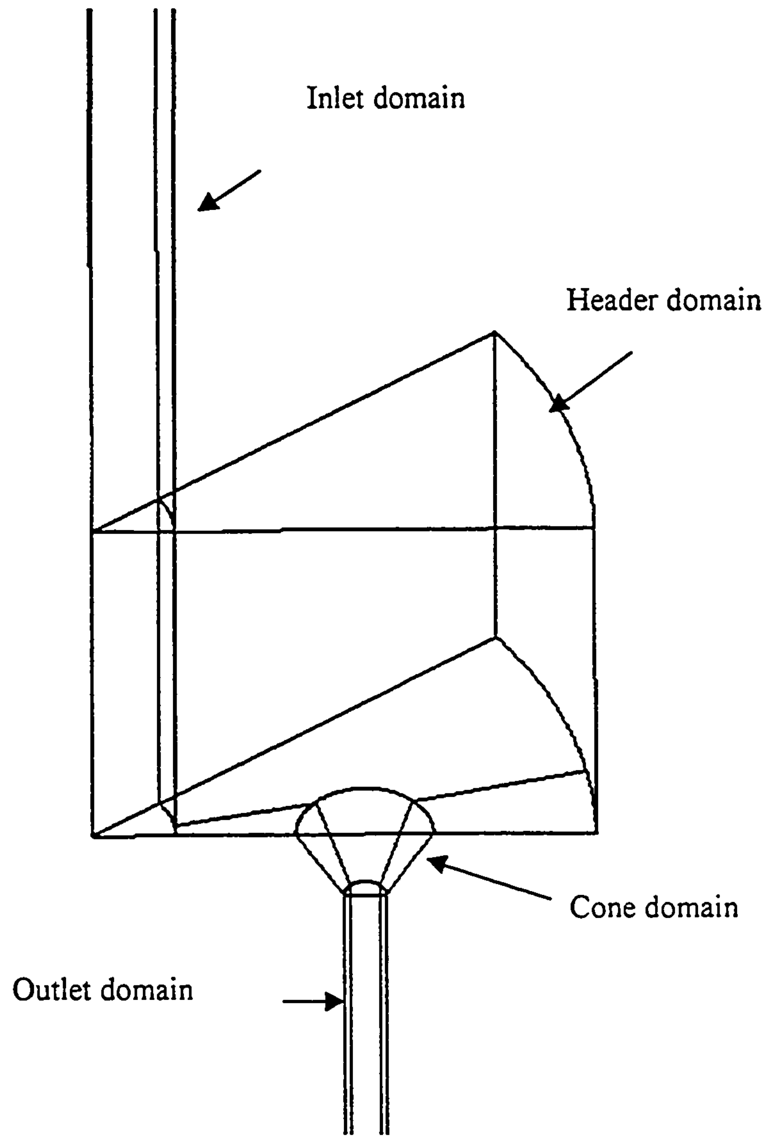

Figure 5.4: Geometry with $\alpha = 30°$ with the 4 domains labeled.

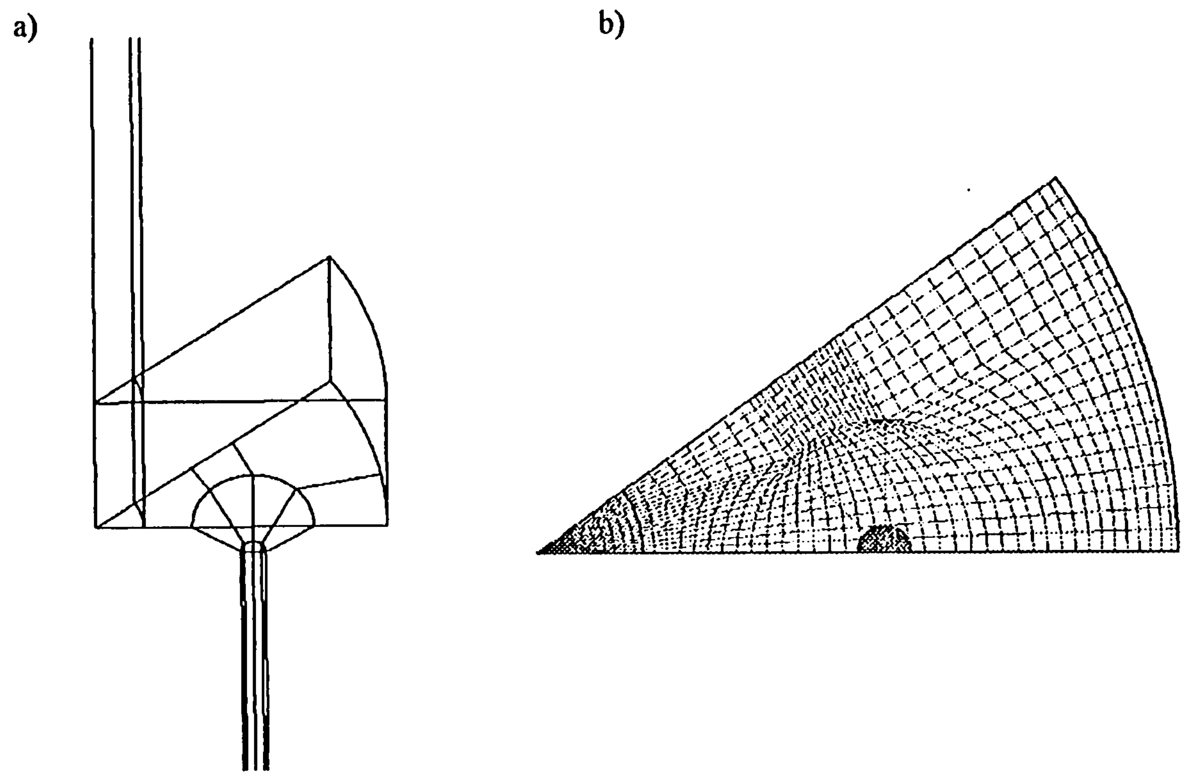

Figure 5.5: a) Geometry and b) grid for the model with $\alpha = 45°$ using the 4-domain approach leading to unacceptable solution convergence.

A solution for the $\alpha = 55°$ case was not even attempted as the grid produced by such methods was unacceptably skewed.

It was finally established that a new grid configuration was in order. Many types of grid configurations were attempted; none of which offered any improvement to the above configuration. Finally a successful grid and model configuration was conceived. This approach proved to be successful for both the $\alpha = 45°$ and $\alpha = 55°$ cases. This configuration is depicted in Figure 5.6. There are two main innovations to this new approach: the further subdivision of the header into three domains, and most importantly, the addition of another minute symmetry plane running axially along the center of the outlet domain and continuing through header. Figure 5.6 a) shows these two sub-divisions. One is the extension of the inlet tube into the header and the other is the extension of the inlet to the cone domain into the header. It should be noted that the remaining C-shape is actually composed of three logical sub-domains, but they are all linked into one composite domain. Also shown in this figure is the zoom area expanded in Figure 5.6 b). As we can see, this other symmetry plane is defined by the surface of a cylinder cut axially in half. The radius of this cylinder is also 0.0005 m.

The reason for these modifications was as follows. It was seen through many of the trial runs that certain features aided or deterred the convergence of the solution. Grids in which the grid size increased drastically led to poor results, as did grids that were coarse in the cone domain and in the regions surrounding the entrance to the cone, along the base of the header. This is understandable, as these are the areas in which rapid

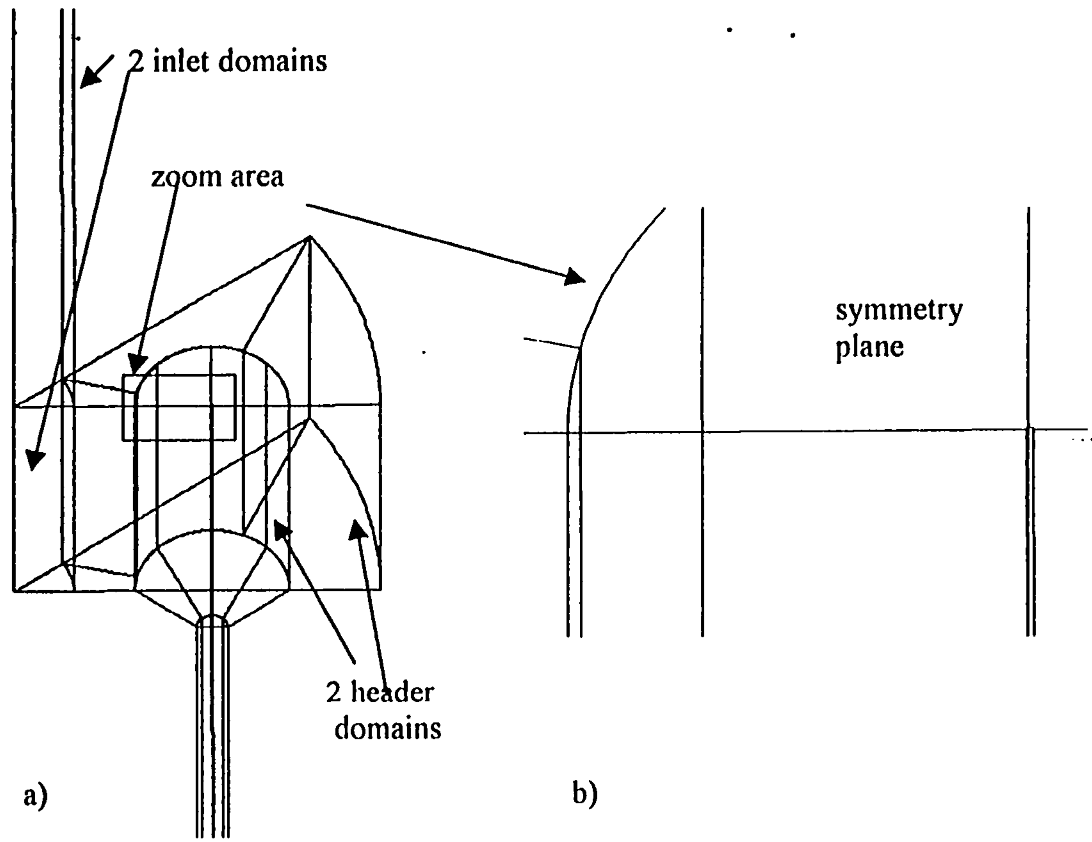

Figure 5.6: Geometry of the model with $\alpha = 45°$ showing a) the sub-domains, and b) close-up of the symmetry plane approximation leading to acceptable solution convergence.

change in flow characteristics occur. The addition of the miniscule symmetry plane approximation enabled a much more structured and finer grid in the regions of interest. It also enabled a smoother radial-type of grid formation. Thus, these modifications afforded greater control over the grid distribution and density than previously possible. Figures 5.3 c) and d) show the finer grids that are obtained with this approach for the α = 45° and α = 55° cases, respectively. The added uniformity and density of the grid in the regions surrounding the entrance to the cone and the cone itself can immediately be seen when compared with Figures 5.5 b) showing the grid for the α = 45° case using the old approach.

The residuals obtained for α = 45° with the domain and grid configuration described in Figure 5.5 are plotted in Figure 5.7. The residuals obtained for the final simulations using the grids in Figure 5.3, are shown in Figure 5.8 a) through d). As was mentioned earlier, it was very difficult to meet the recommended residual drop of four to five orders of magnitude for all degrees of freedom. Early on it was realized that a major limitation would be the amount of computer memory resources. All simulations were run with grids having a total of 36,000 – 40,000 cells. This was the maximum allowable number of grid cells given the amount of memory on the HP workstation. Therefore, for a given simulation, it was not possible to increase the overall density of the grid. It was only possible to "shift" grid density. If greater detail was needed in one area, detail in some other area had to be sacrificed. This was also a very important constraint during grid generation, as it was very important to avoid wasting memory by having the grid dense in areas where it was not required.

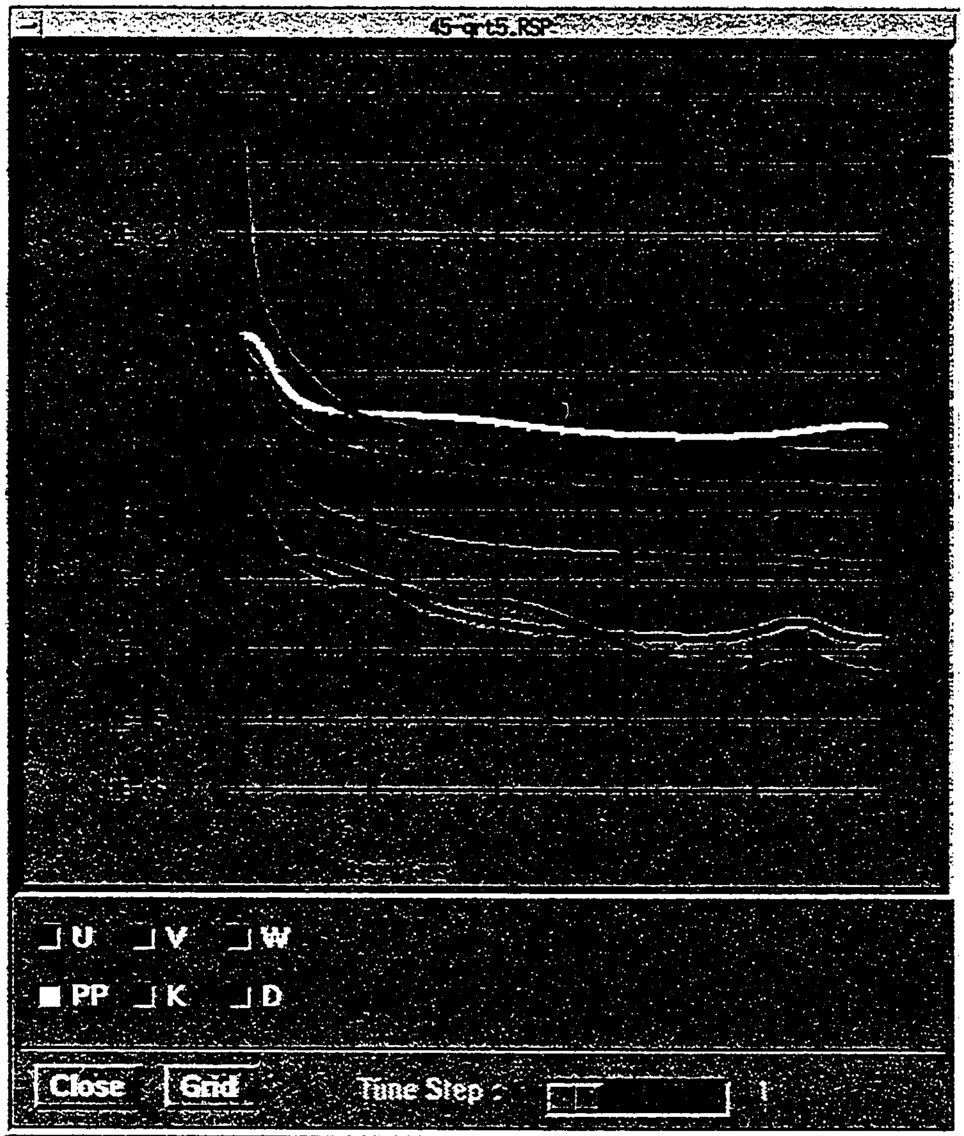

Figure 5.7: Residual plots for the model with $\alpha = 45°$, using the grid shown if Figure 5.5.

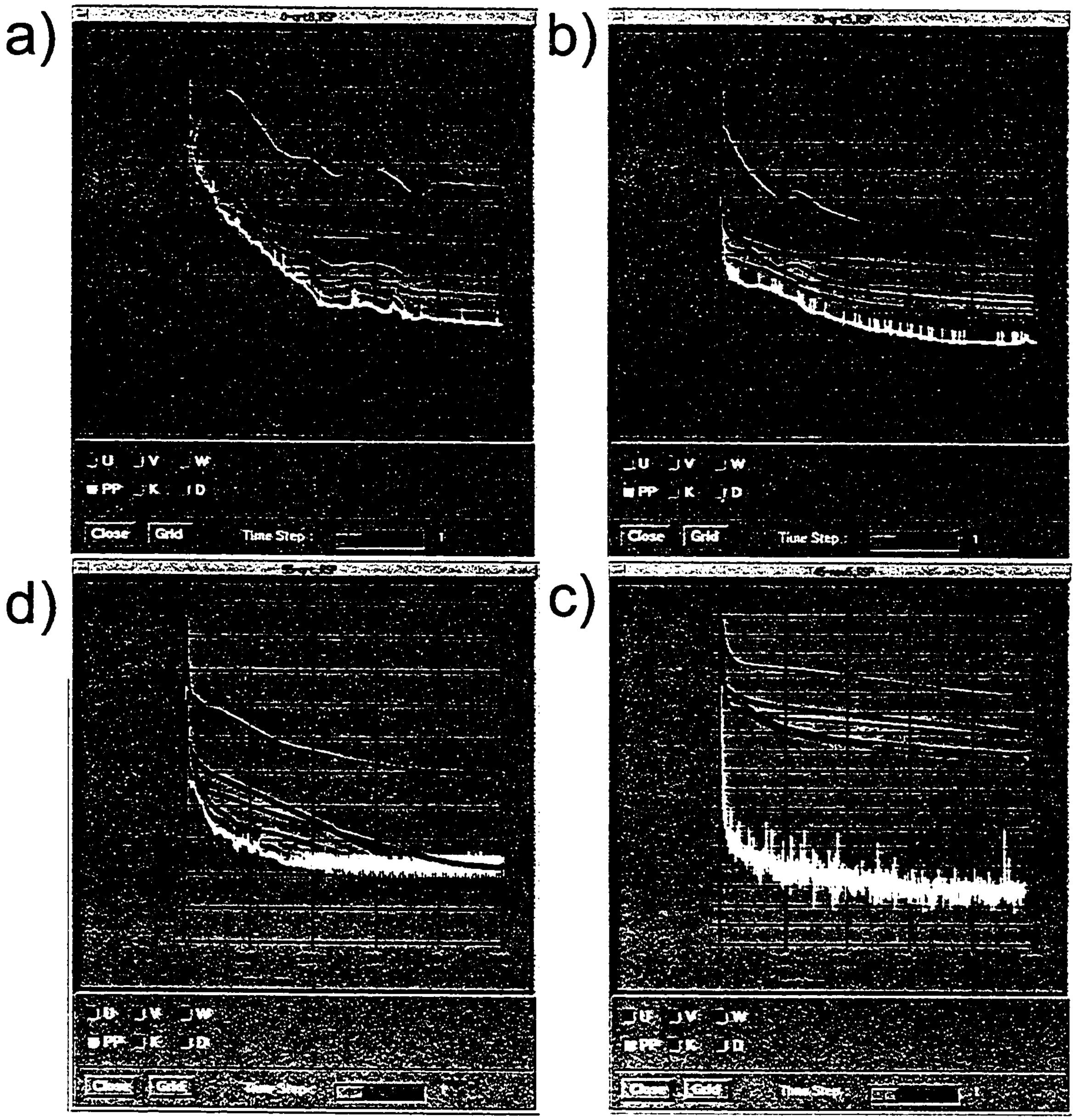

Figure 5.8: Plots of the residuals for the 4 models, where: a) $\alpha = 0°$, b) $\alpha = 30°$, c) $\alpha = 45°$, and d) $\alpha = 55°$.

Thus a decision was made as to what level of convergence would be acceptable for this study. It was kept in mind that the objective of the study was to use the simulations as a design tool. It was not intended that the physics be exactly replicated (already, a two-phase pulp suspension was being approximated by a single-phase fluid). The intention was to see if there exists a characteristic in the hydrodynamics of the approximated system that can be linked to the experimental results already obtained by Chehab (1995). This feature could then be used to assess the effect that geometry would have on fiber accumulation within the header. It was established that, for these purposes, a drop of four orders of magnitude would be acceptable for the most dominant variables (i.e. the pressure correction term and *w*) and three orders of magnitude for the other variables.

From the residual plots in Figure 5.8 a) through d), we can see that these drops in residuals have been achieved. However, if we examine the residuals given in Figure 5.7 for the grid formulation of the $\alpha = 45°$ case depicted in Figures 5.5 a) and b), we see that *pp* and *w* did not meet these criteria and thus the grid formulation was rejected. Therefore, the $\alpha = 0°$ and $\alpha = 30°$ cases were modeled using a single symmetry plane approximation axially along the center of the inlet tube. Whereas, the $\alpha = 45°$ and $\alpha = 55°$ cases were modeled using two symmetry planes, one axially along the center of the inlet tube and another along the axis of the outlet tube. This provided acceptable convergence for all values of α as seen in Figure 5.8.

5.2 Turbulent Model Effects

Several models are available to approximate the turbulent hydrodynamics occurring within the header. These were presented in Section 3.3. Firstly, the Eddy Viscosity model was dismissed as it required the input of a value of the turbulent viscosity, μ_t. Such experimental data was not available for this study. Also, it was recommended in the documentation that the Eddy Viscosity model is mainly useful as a rough but simple approximation to turbulent flow (CFDRC, CFD-ACE User Guide, 1996). The Baldwin-Lomax model was also dismissed as it was developed mainly for wall bounded flows. This model might not faithfully predict the areas of high free-shear flow that would arise in the header where the incoming fluid would encounter a vortex formation. It was finally decided that the preliminary simulations would employ the standard $k\text{–}\varepsilon$ model. CFDRC documentation (CFDRC, CFD-ACE User Guide, 1996) strongly recommends that this model be used in most situations unless another model is obviously more suitable.

As discussed earlier, the standard $k\text{–}\varepsilon$ model employs wall functions and hence requires that the first grid point be placed within the exponential layer, that is y^+, the normal distance from the wall in wall units, should be between 30 and 100. Figure 5.9 is a screen capture of the results of one of these simulations. This figure shows sample plots of the value of y^+ along trace lines on the walls in various positions in the header. As we see, all values of y^+ along the wall are approximately below the value of 5. It was then attempted to alter the grid spacing so as to obtain y^+ values in the appropriate range.

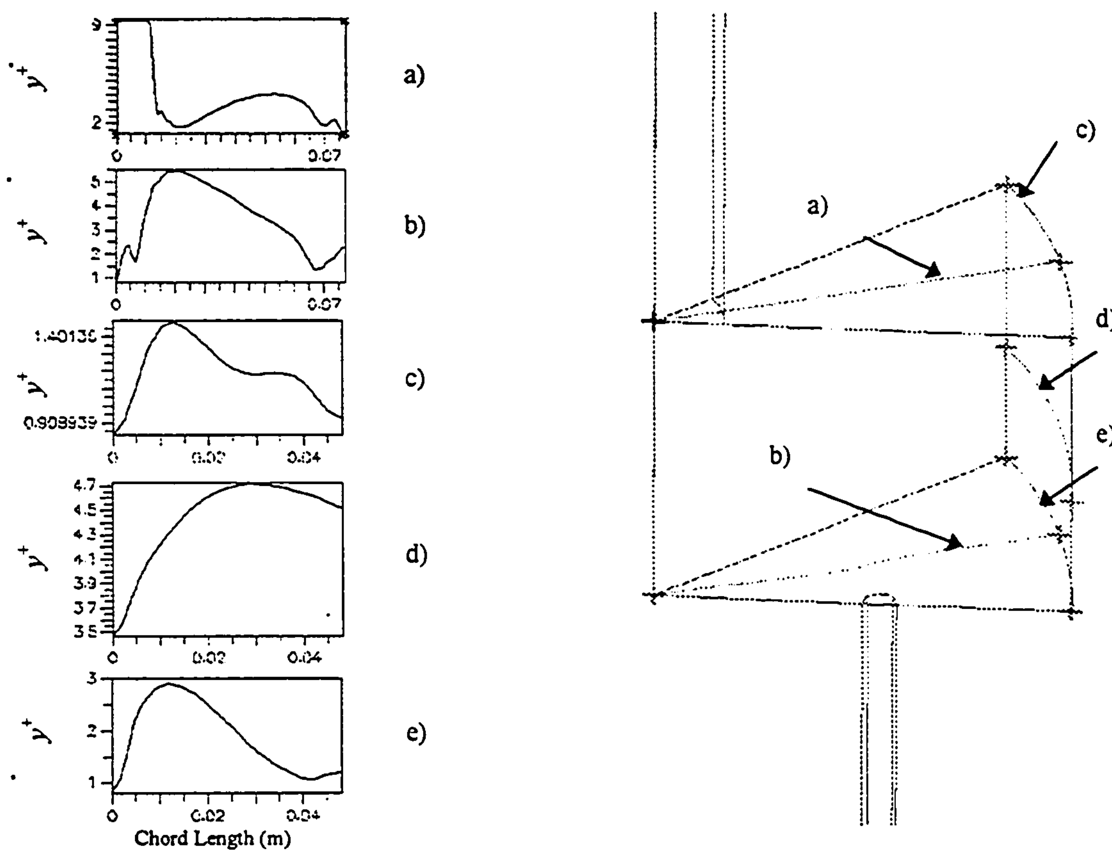

Figure 5.9: Plots of y^+ versus chord length along selected line traces adjacent to walls, using the standard k–ε model.

However, this had adverse effects upon the convergence of the simulation. Therefore, it was concluded that the standard $k-\varepsilon$ model was inadequate and that a low Re turbulence model was required. Again, referring to Figure 5.9, it can be seen that y^+ is approximately 5 or less, which is a requirement for a low-Re model, so that no further grid restructuring is necessary with respect to y^+.

There are two low Re models to choose from in CFD-ACE: 1) the Low Re $k-\varepsilon$ model and 2) the $k-\omega$ model. As the standard $k-\varepsilon$ is in such widespread use, it was decided that its variant, the Low Re $k-\varepsilon$ would be used for this study. The major difference between these models is in their prediction of the behaviour in the near wall regions. The differences in the results of the two models in the other regions within the header were investigated. Simulations were performed with the two turbulence models. One employed the Low Re $k-\varepsilon$ model, and the other employed the $k-\omega$ model. The results are shown in Figures 5.10 and 5.11, where the magnitude of the velocity vector taken along line traces at various sample positions in the header is shown.

As we can see from these figures, the trends predicted by both of these models are similar. If we examine the plots a) and d) in both figures, we also see that the only places where the values predicted by the two models differ significantly are in regions close to the wall. There is no significant difference in the velocity profiles away from the wall. Due to its widespread use, the Low Re $k-\varepsilon$ model was chosen as the turbulence model to be used throughout the study.

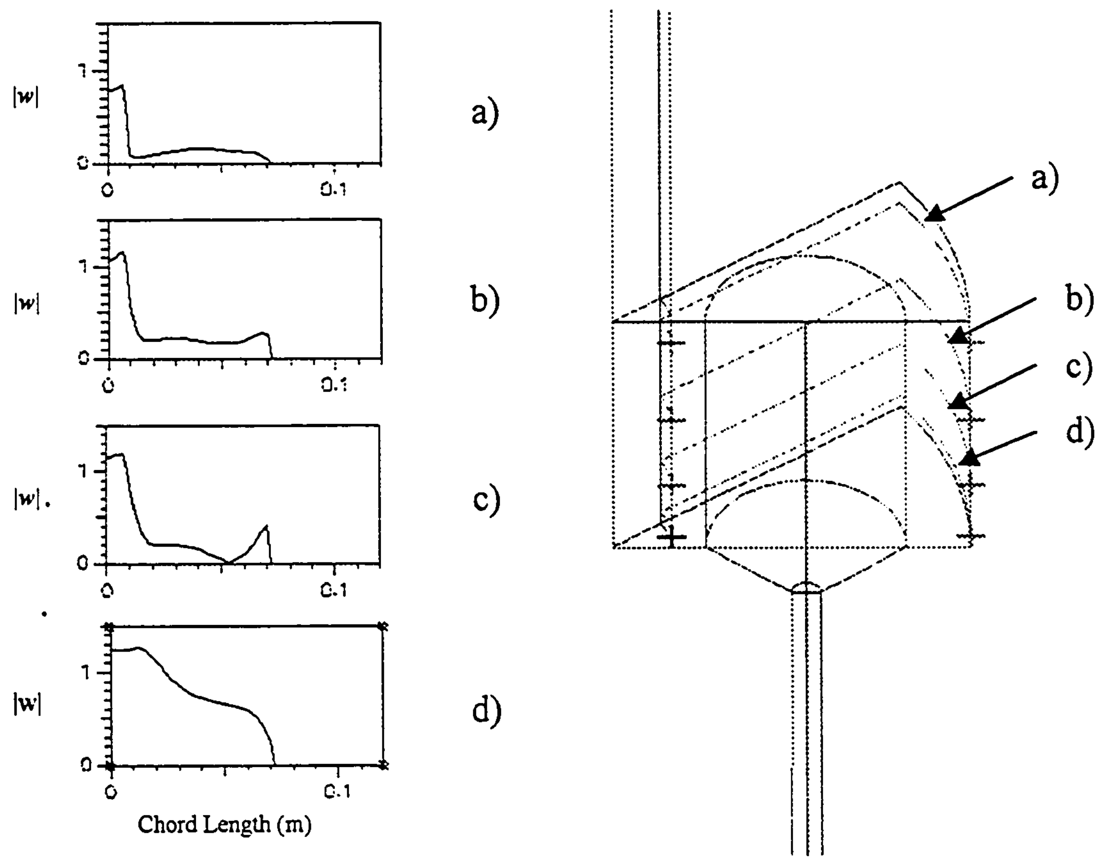

Figure 5.10: Plots of |w| (m/s) versus chord length along selected line traces for the simulation employing the low Re $k-\varepsilon$ model.

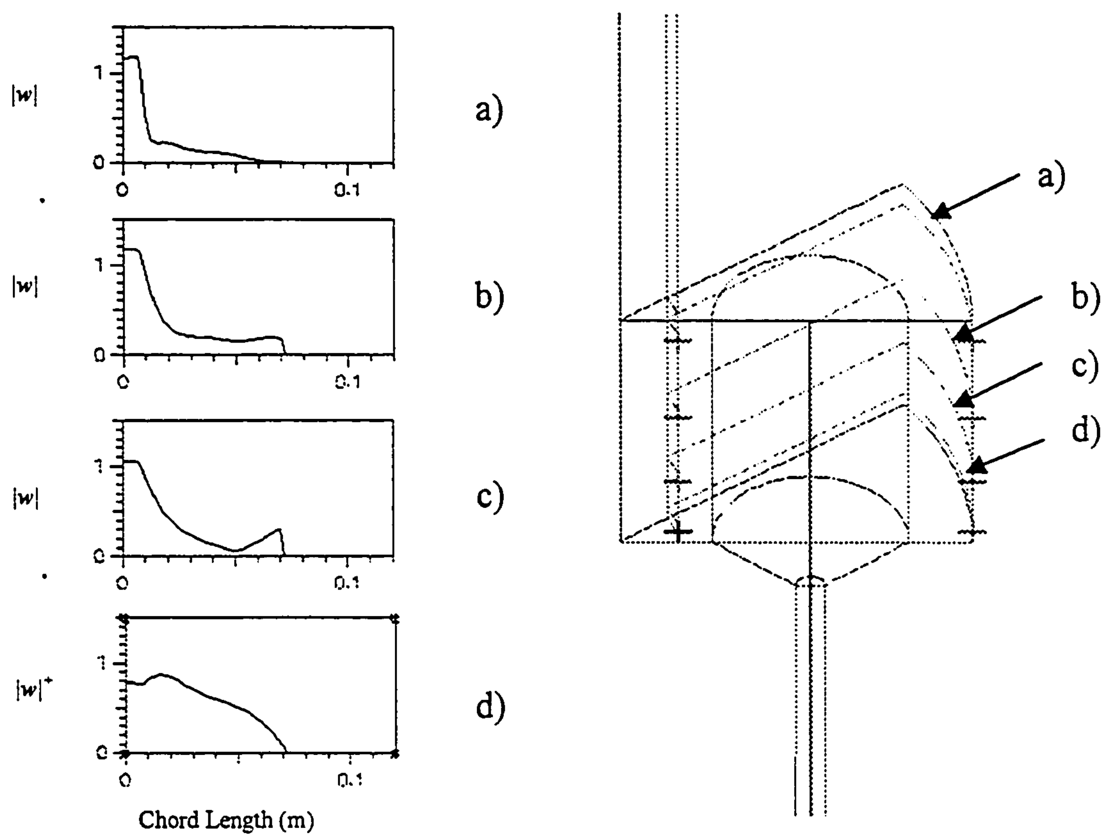

Figure 5.11: Plots of $|w|$ (m/s) versus chord length along selected line traces for the simulation employing the $k\!-\!\omega$ model.

5.3 Header Hydrodynamics Simulation and Characterization

The hydrodynamics within the model header were simulated using the CFD-ACE+ package. The values for u, v, w, k, and ε throughout the module header were obtained by solving the disctretized forms of the governing equations at the spatial locations specified by the grids described in Section 5.1 and using the Low Re k-ε model to simulate turbulence. The full velocity vector $\bar{v}$ was selected as the quantity to characterize hydrodynamic features within the header. The results of this characterization are presented in the following section.

The hydrodynamics of all simulations exhibited very defined structures. These can best be identified by looking at the results of the $\alpha = 0°$ case. Figure 5.12 presents the plots of the velocity, in three formats. Figure 5.12 a) presents a two-dimensional contour plot of the magnitude of the velocity vector, $|\bar{v}|$, along a cross-sectional cut through the center of the header. Figure 5.12 b) presents a two-dimensional velocity vector plot superimposed over a contour plot of $|\bar{v}|$ along an axial cut down the center of the geometry, such that an outlet tube is bisected. Figure 5.1 c) depicts a three-dimensional iso-velocity surface plot of $|\bar{v}| = 0.1$ m/s for a half section of the header. An iso-velocity surface plot is a plot depicting a surface of constant velocity. In Figure 5.12 c), two such surfaces exist within the header. One surface close to the walls is wrapped around a smaller surface of toroidal shape. One half of the surface defining a toriodal surface of a constant velocity of 0.1 m/s is easily seen in Figure 5.12 c).

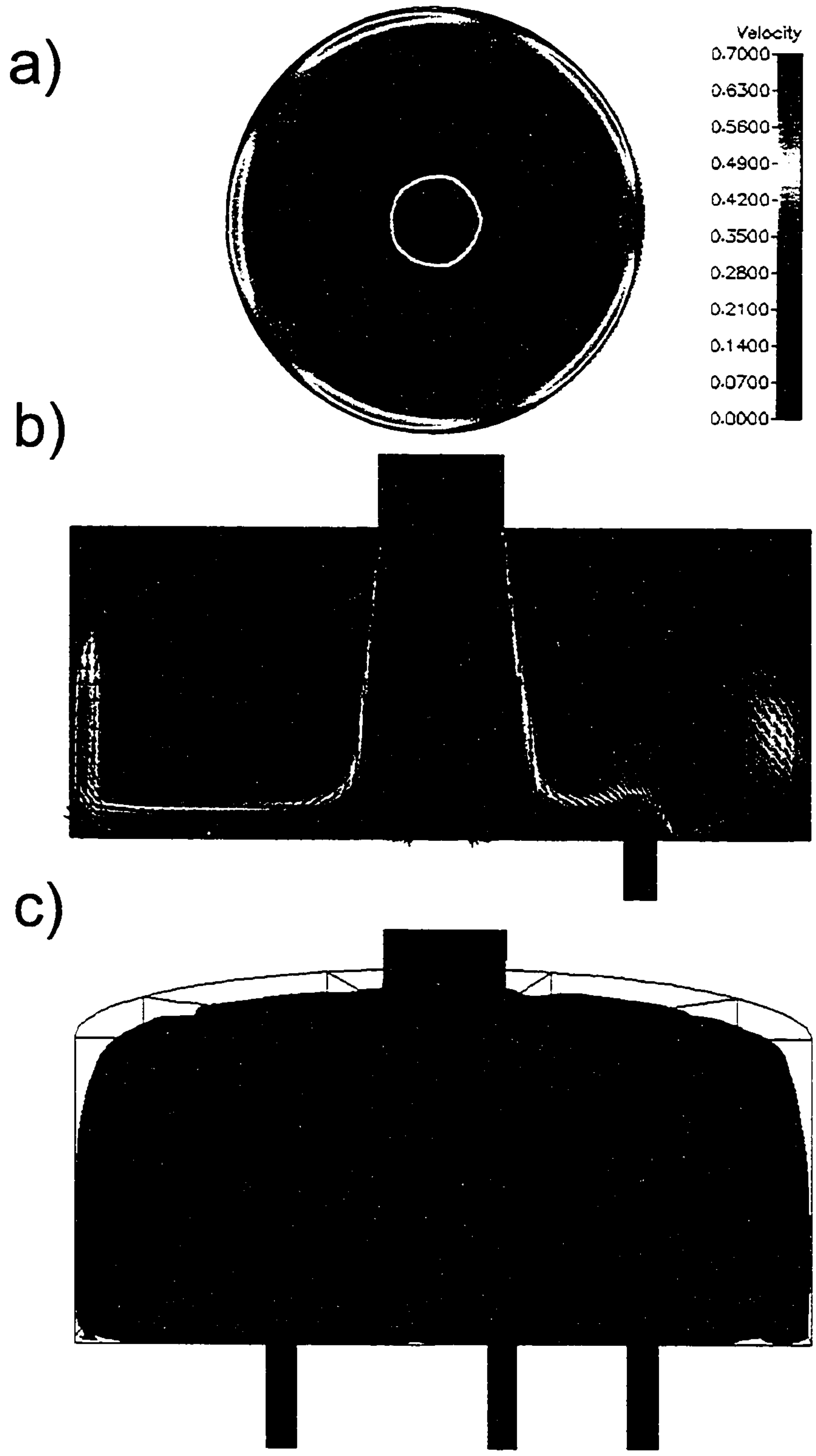

Figure 5.12: Velocity magnitudes depicted in a) cross sectional contours, b axial slice vector plot and contours, and c) iso-surface of velocity = 1 m/s.

It should be noted here, that although only the symmetry sub-unit as depicted in Figure 3.2 and Figure 4.4 was modeled, CFD-VIEW, the results visualization package of CFD-ACE+, allows the replication of the results database of such symmetrical domains, such that the full system can be obtained. Most of the figures that will be presented make use of this replication, as this format better illustrates the results.

From these three views, and in particular the vector plot of Figure 5.12 b), we can identify 3 distinct areas within the header. Firstly, in the "corners" where the top and side walls of the header meet, we see a region of low velocity re-circulation. Secondly, in the region defined by a cylinder in the center of the header, we see a region dominated by the high velocity jet of the incoming fluid, which impinges on the bottom of the header. Thirdly, most of the remaining volume is occupied by an area of fluid re-circulation or eddy.

As the eddy seems to be a prominent flow structure in the header, a more detailed description of the eddy is in order. From Figures 5.12 a), b), and c), the 3-dimensional, physical nature of this eddy formation can be seen. The colours used in these figures are designated in the legend and are as follows: red implies high velocities or fluid movement and blue lower fluid movement. The legend applies to Figure 5.12 a), b), and c).

The eddy forms a large irregular toroid, concentric with the header and inlet tube. It can be seen in Figure 5.12 a) and c) that the eddy swells and contracts at regular intervals coinciding with the presence or absence of an exit tube. In the regions between the exit tubes, the eddy becomes more defined and intense. Its strong re-circulating pattern encompasses more of the header volume at these locations. Also the area of little movement (dark blue) also becomes elongated to occupy more vertical space as seen in Figure 5.12 b). In regions above the exit tubes, the eddy becomes less intense and more diffuse. The re-circulating pattern becomes less defined and occupies less space. As seen in Figure 5.12 b), there is more fluid mixing in the upper part of the header above the exit tube. Also it is evident that the volume of stagnation at the center of the eddy decreases. One very important feature to notice is the high velocities on the return side of the eddy in the regions between the exit tubes. The return side is defined as the wall side of the eddy. This is seen from the more reddish areas along the wall of the header in Figure 5.12 a).

To get a general perspective on the changes that occur within the header as the inlet angle is increased, a succession of plots of iso-velocity surfaces were generated. Figures 5.13 through 5.15 compare the iso-velocity surface plots for all four values of α, for velocity magnitudes of 0.1, 0.2, and 0.3 m/s respectively.

First, examining Figure 5.13, it can be seen that as α increases from 0° to 55°, the volume of this torus confined to a velocity magnitude of 0.1 m/s does not vary in any significant manner. This is expected, as the regions in which the velocity is at this lower end of the spectrum within the header, is usually confined to the central areas of the eddies and to vicinities near the wall of the header. As iso-velocity surfaces depicting higher velocities are examined, the effect of the inlet angle, α, upon the eddy becomes

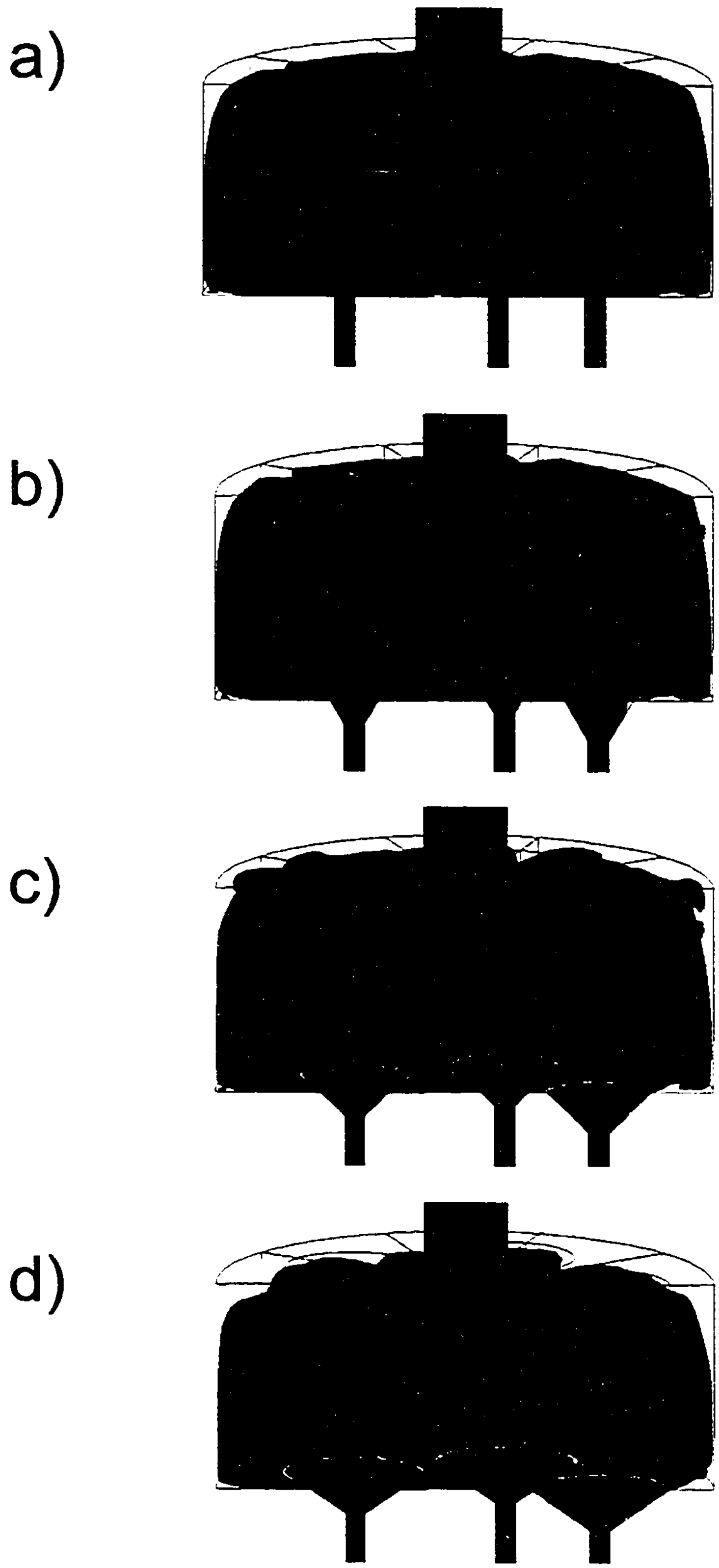

Figure 5.13: Iso-velocity plots with velocity = 0.1 m/s for: a) $\alpha = 0°$, b) $\alpha = 30°$, c) $\alpha = 45°$, and d) $\alpha = 55°$.

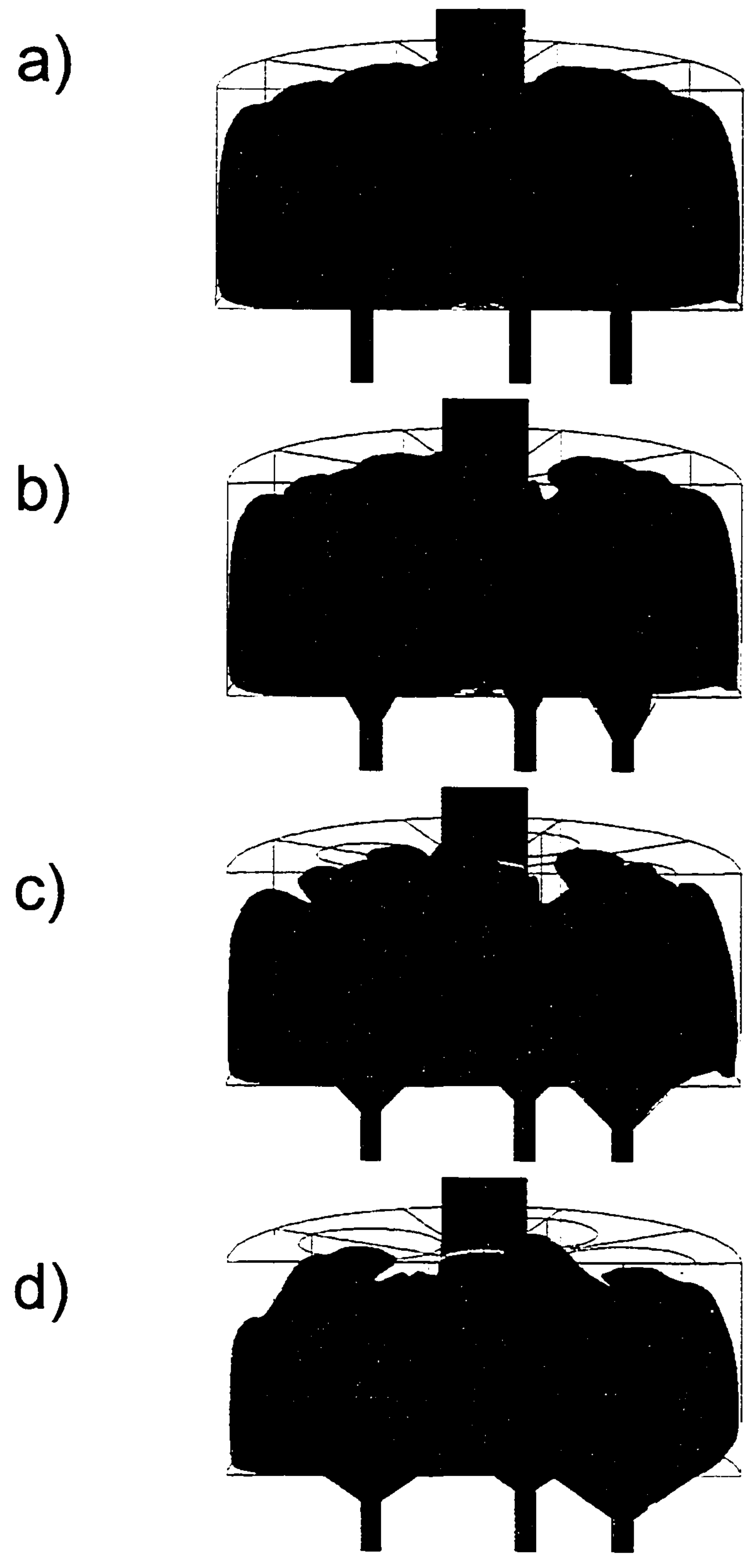

Figure 5.14: Iso-velocity plots with velocity = 0.2 m/s for: a) $\alpha = 0°$, b) $\alpha = 30°$, c) $\alpha = 45°$, and d) $\alpha = 55°$.

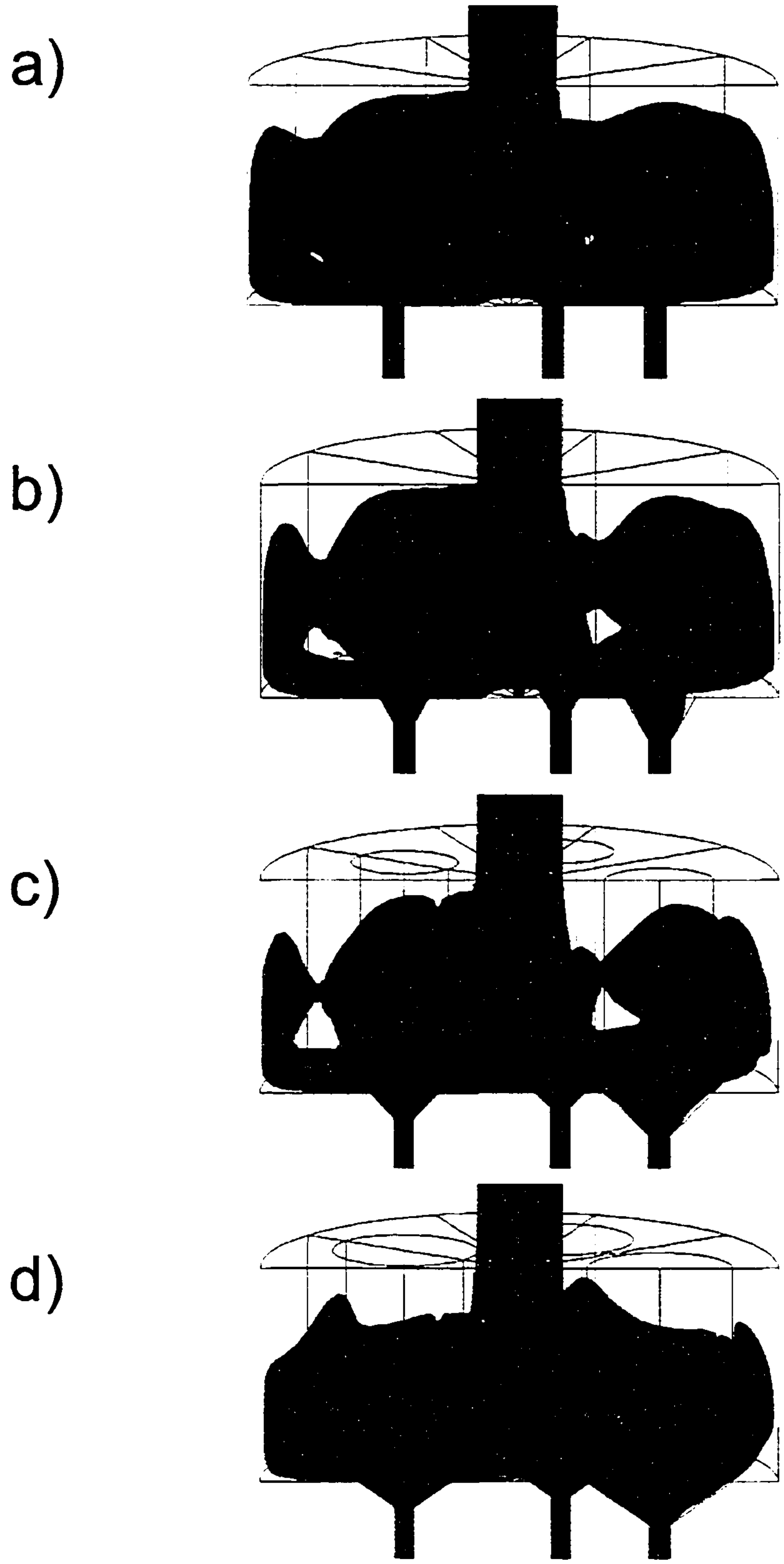

Figure 5.15: Iso-velocity plots with velocity = 0.3 m/s for: a) α = 0°, b) α = 30°, c) α = 45°, and d) α = 55°.

evident. Figure 5.14 shows the surfaces for iso-velocities of 0.2 m/s for all four cases. As α increases, it can be seen that the eddy becomes less structured and intense with respect to regions of higher velocity. More volume within the header is occupied by velocities of this magnitude when $\alpha = 55°$, than when $\alpha = 0°$. Therefore the overall intensity of the eddy decreases while mixing in the header increases. Turning to Figure 5.15 a), it can be seen that the higher velocity in the $\alpha = 0°$ case still occupies a very defined and large volume along the walls of the header. As α increases, this volume along the walls occupied by the higher velocity decreases.

In order to better evaluate the changes in the intensity of the eddies as the inlet angle is varied, the magnitude of the velocities in a cross section of the header were compared. Figure 5.16 shows flooded contour plots of the velocity magnitude in a cross-section taken through the middle of the header. For all angles, the eddy is most intense in the regions between the exit holes. Also the intensity of the eddy decreases and the eddy is more diffuse as the value of α increases.

To obtain a more detailed picture of the changes of the eddy formation as the inlet angle decreases, plots of the velocity vectors superimposed over the velocity magnitude contour plot along an axial slice were examined. The slice bisects the header running through the center of the outlet tube, and midway between two outlet tubes. Figures 5.17 and 5.18 show these sections for the four cases. Looking at the eddy on the left side of these plots, or the side between two exit tubes, we see that as α increases, the eddy

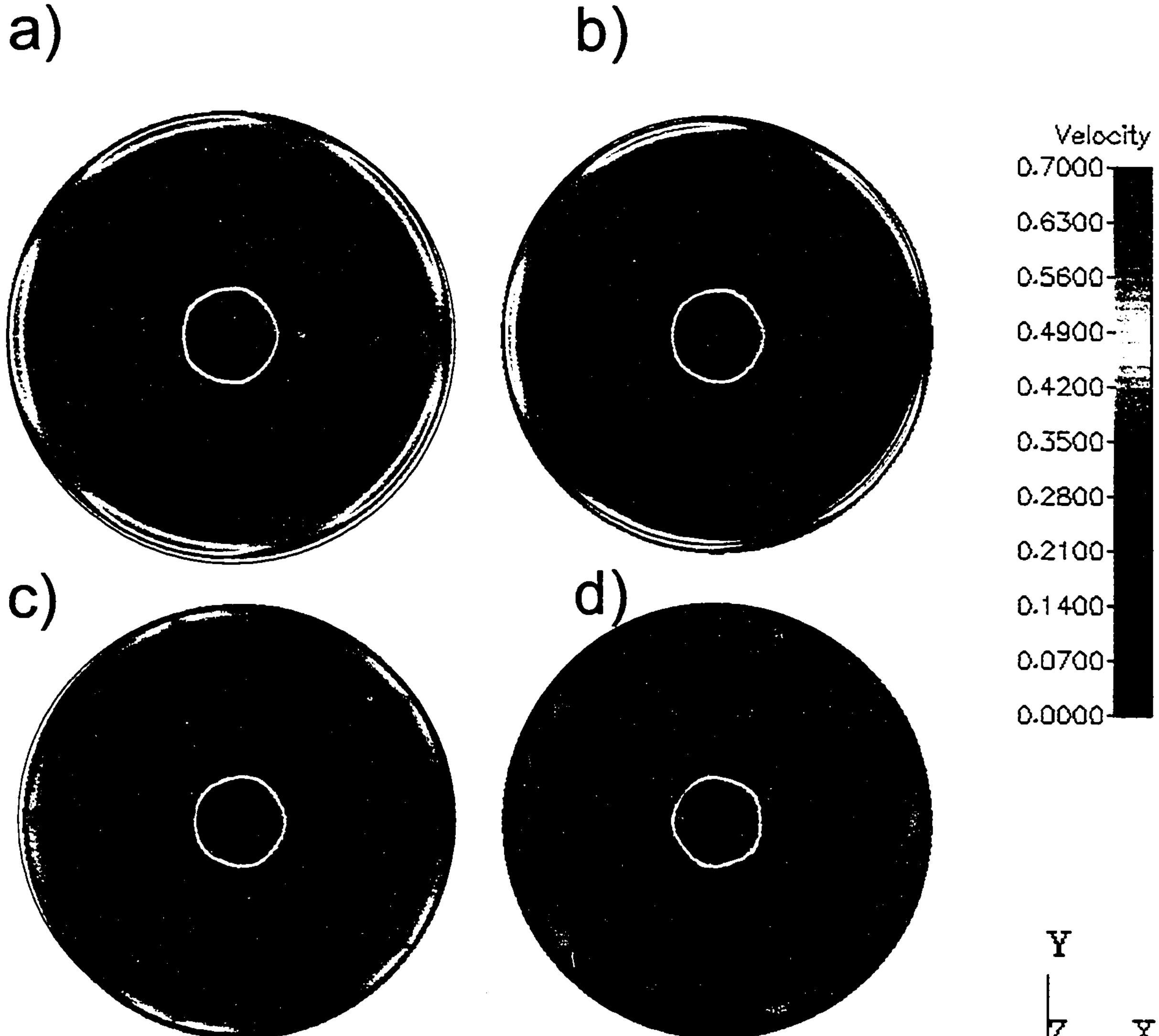

Figure 5.16: Velocity contour plots through midpoint of header for: a) $\alpha = 0°$, b) $\alpha = 30°$, c) $\alpha = 45°$, and d) $\alpha = 55°$.

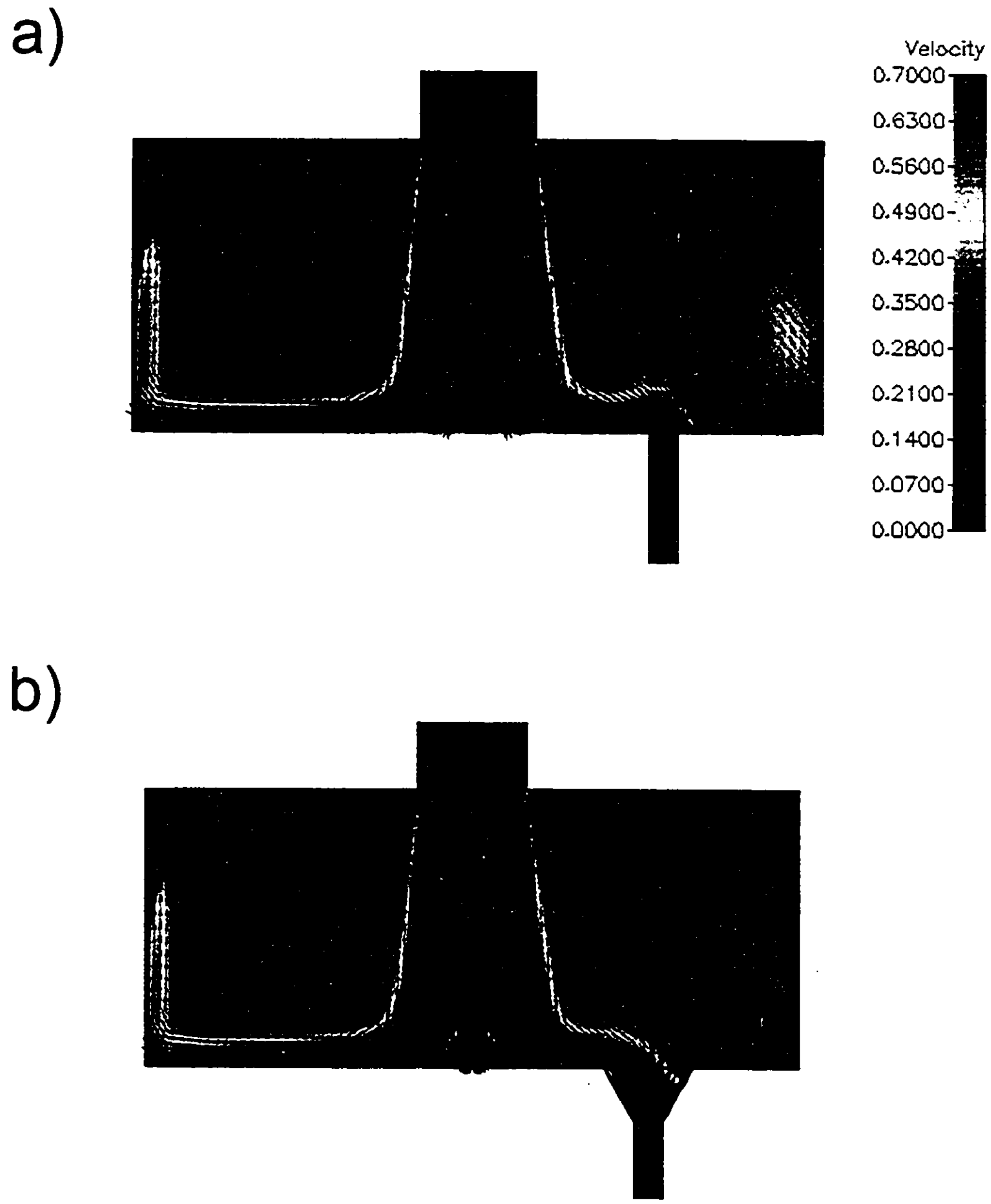

Figure 5.17: Velocity vector plots superimposed over velocity contour plots along an axial cut for: a) $\alpha = 0°$, b) $\alpha = 30°$.

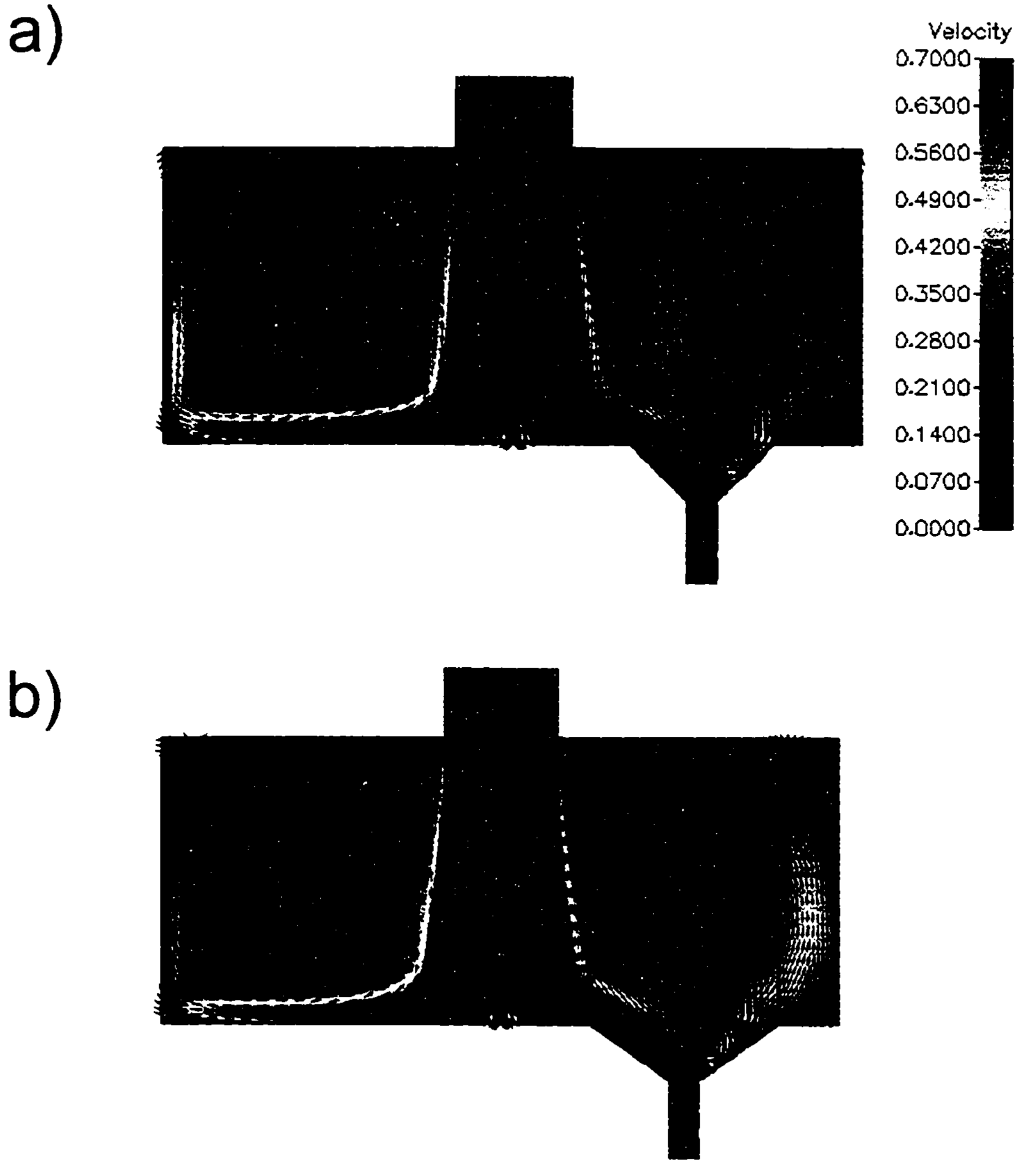

Figure 5.18: Velocity vector plots superimposed over velocity contour plots along an axial cut for: a) $\alpha = 45°$, b) $\alpha = 55°$.

formation becomes more circular and less intense. A greater amount of mixing throughout these sections is also clearly visible at higher values of α.

5.4 Correlation of Hydrodynamic Modeling with Experimental Results

The approach then, is to focus the study on changes in the eddy structure in the region between exit tubes as the inlet angle is varied and then correlate the observed experimental accumulation with these changes in the eddy formations. For a more quantitative analysis, figures showing the axial velocity components, w, along a selected cell index through the header are presented. This trace was fixed exactly midway between two exit tubes as this was established to be the most intense part of the eddy. Axially, the trace was fixed halfway through the header. Figures 5.19 through 5.22 show plots of w versus radial distance for the four values of α. These traces, similar to those depicted in Figures 5.10 and 5.11, all begin at about 1.2 cm in from the center and extend to the wall. This axial section was found to fully define the eddy structure, including the effects of the shearing action due to the incoming fluid. From these figures, it is evident that the effect due to the shearing action of the incoming fluid equally affects all cases. There is little effect of inlet angle, α, on the hydrodynamics of the inlet-side of the eddy. However, we do see that there is a strong effect of the inlet angle on the return side. This effect manifests itself in two ways. First, as the value of α increases, we see that the peak axial velocity component decreases. It drops from around 0.57 m/s for $\alpha = 0°$ to 0.30 m/s for $\alpha = 55°$. Secondly, we also see that the velocity gradient also is strongly affected by the inlet angle. As α increases, the velocity gradient decreases.

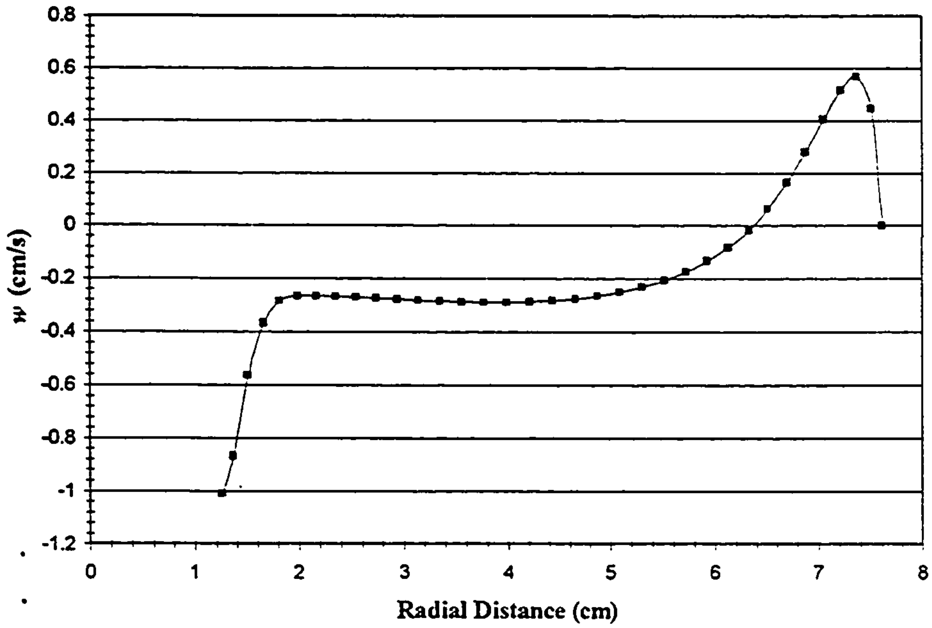

Figure 5.19: Axial velocity component w versus radial distance from inlet side of eddy, for $\alpha = 0°$.

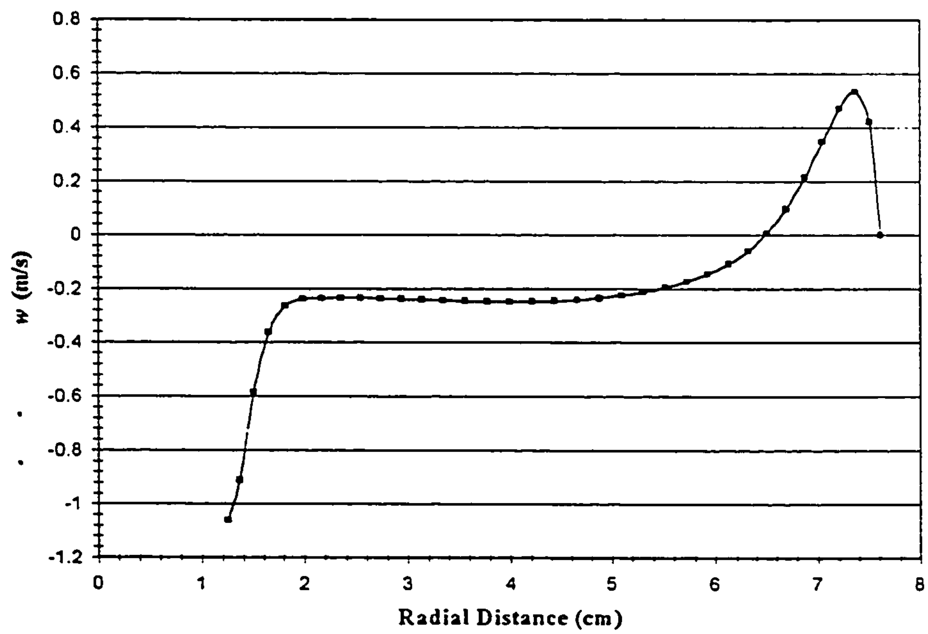

Figure 5.20: Axial velocity component, w versus radial distance from inlet side of eddy, for $\alpha = 30°$.

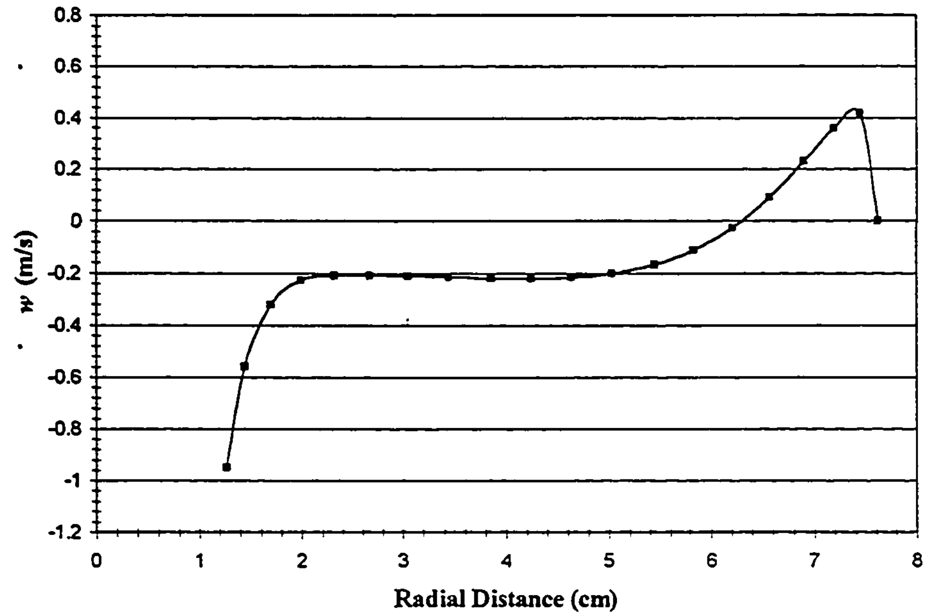

Figure 5.21: Axial velocity component, w versus radial distance from inlet side of eddy, for $\alpha = 45°$.

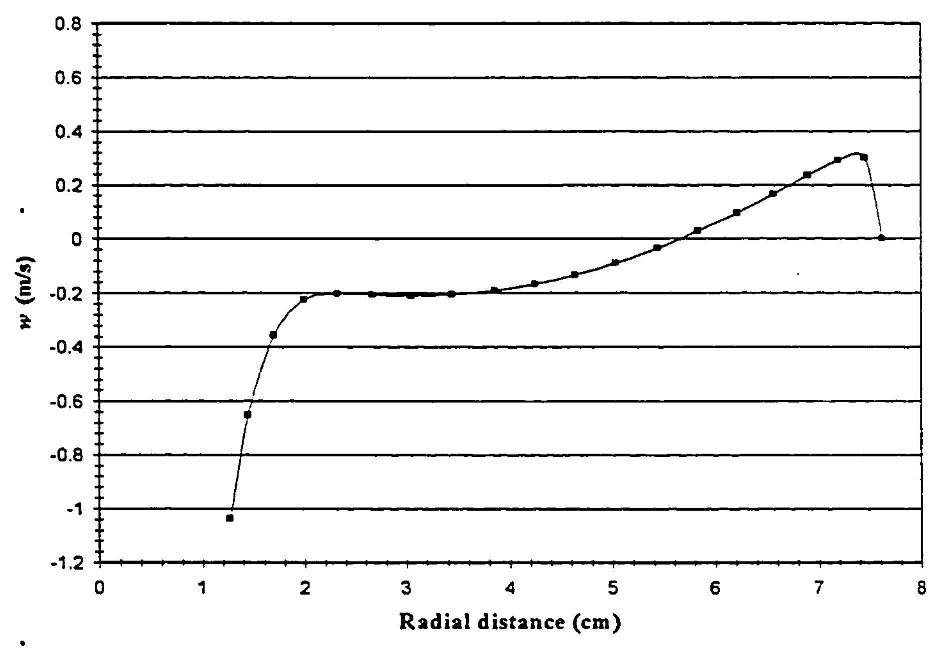

Figure 5.22: Axial velocity component, w versus radial distance from inlet side of eddy, for $\alpha = 0°$.

In order for this analysis to be most useful, some quantitative indicator of eddy intensity must be found with which the experimental results can be correlated. By reviewing Figures 5.19 to 5.22 and seeing that the characteristic length defining the return side of the eddy is sufficiently similar for all cases, it can be proposed that the return side w_{max} would be a good indicator for the eddy intensity. Figure 5.23 shows the results of correlating w_{max} with the observed experimental accumulation. As we see from this figure, there is a strong agreement between the observed accumulation and w_{max}. The correlation results in linear relationship with a correlation factor of 0.9802. The intercept of 0.12 m/s can be physically interpreted as the value of w_{max} that would be required to produce no accumulation.

As mentioned in section 2.2, possible mechanisms of accumulation are: impingement , centrifugal forces and shear diffusion. By re-examining Figures 5.17 and 5.18, we see that there is very dominant flow along the bottom plate of the header to the outlet. Therefore, it can be reasoned that any particles that are dephased upon impingement would be swept along with this flow out of the header. Also, impingement does not account for the strong correlation between w_{max} and the experimental data for accumulation. The centrifugal force is given by the following (Jenson and Chenoweth, 1972):

$$F_c \; \alpha \; \frac{v^2}{r} \qquad (5.4\text{–}1)$$

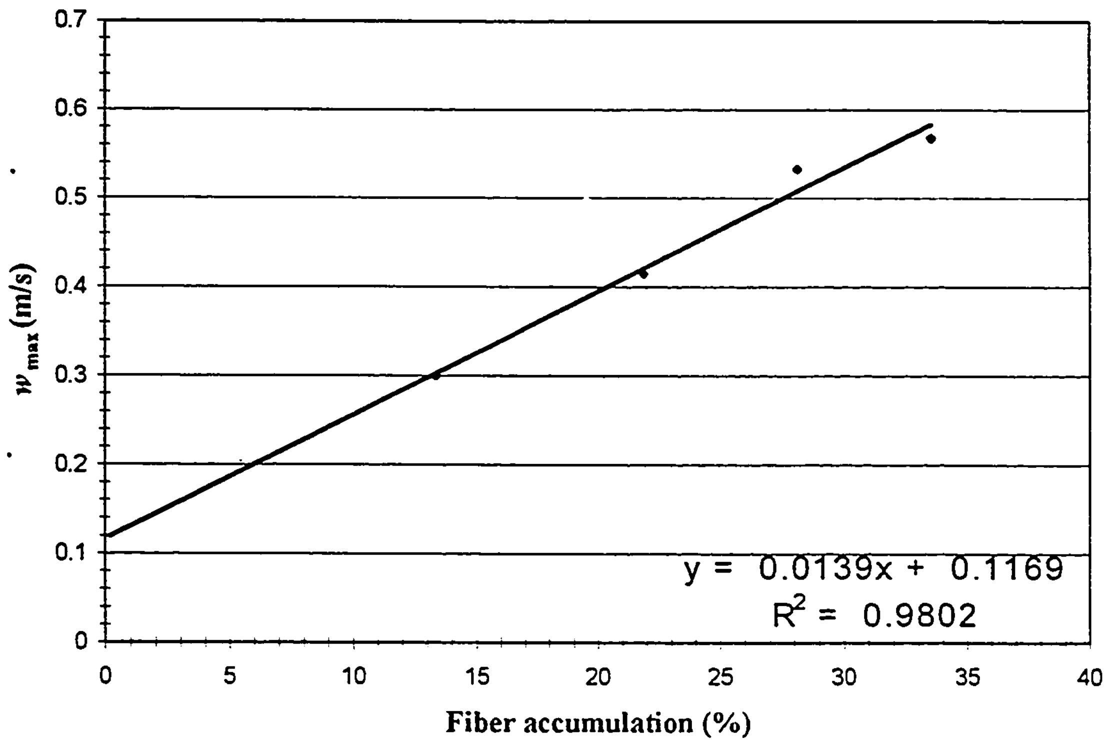

Figure 5.23: w_{max} versus % fiber accumulation correlation.

As we see from the above relation, the centrifugal force varies with the square of the velocity. If accumulation were due to the centrifugal force due to eddy re-circulation, then the plot of w_{max} versus accumulation shown in Figure 5.23 should not be linear. Therefore, it can be concluded that centrifugal forces are not responsible for the accumulation of fibers within the module header.

It is proposed in this study, that the phenomenon of shear-diffusion described in Chapter 2.0 is the mechanism through which the eddy results in the observed accumulation. Shear diffusion is the phenomenon in which a particle migrates from regions of high shear rate to low shear rate. The important nature of this phenomenon is best summarized in the words of Brady: "Because the particle migration is intrinsic, whenever there is an inhomogeneous flow there *must* be concentration inhomegeneities (Brady, 1994)." As the shear gradient is defined as the driving force for particle migration, it would perhaps be beneficial to investigate the variation of the shear rate along the same line traces used in Figures 5.19 through 5.22. Figures 5.24 through 5.27 show the variation in shear rate with radial distance for the four cases. Two main features can be seen from these figures. Firstly, as was suspected, the gradient of the shear rate across the eddy is seen to decrease with increasing inlet angle, α. Secondly the effect of α on the shear gradient on the inlet side of the eddy was seen to be negligible.

As the particle migrates to the regions of low shear within the eddy, which are the central regions of very low fluid movement, a particle can be entrapped within these slow

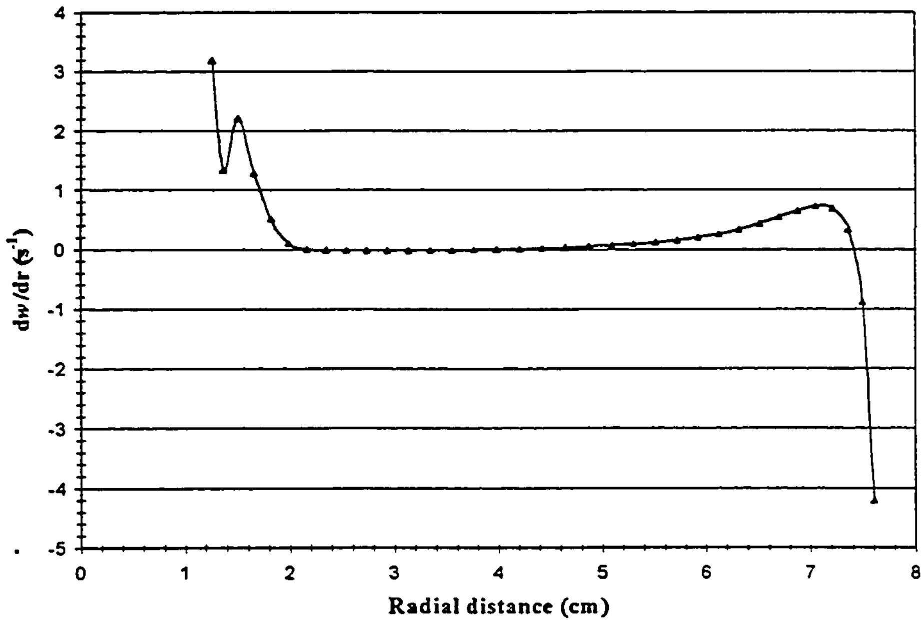

Figure 5.24: Shear rate versus radial distance from the inlet side of the eddy, for $\alpha = 0°$.

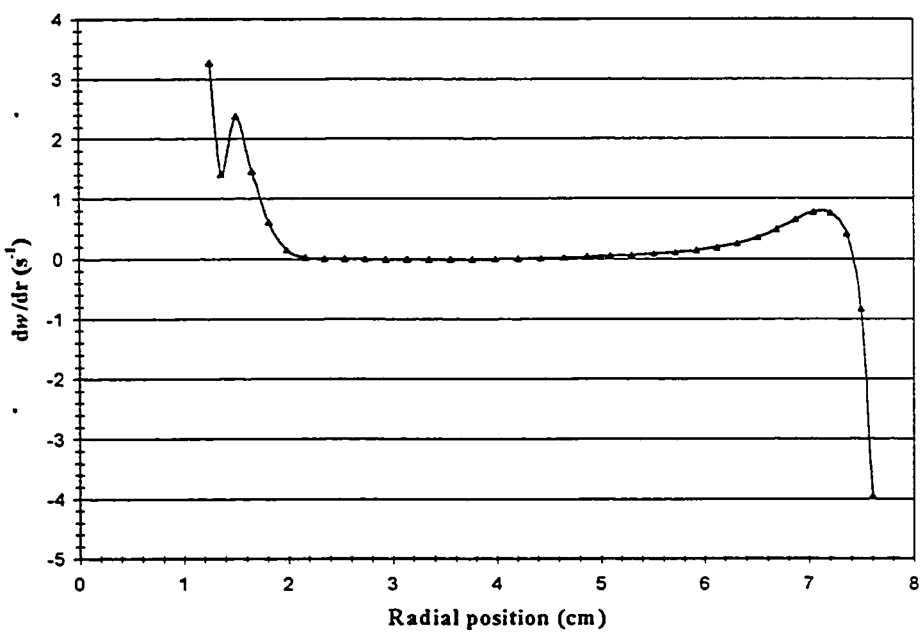

Figure 5.25: Shear rate versus radial distance from the inlet side of the eddy, for $\alpha = 30°$.

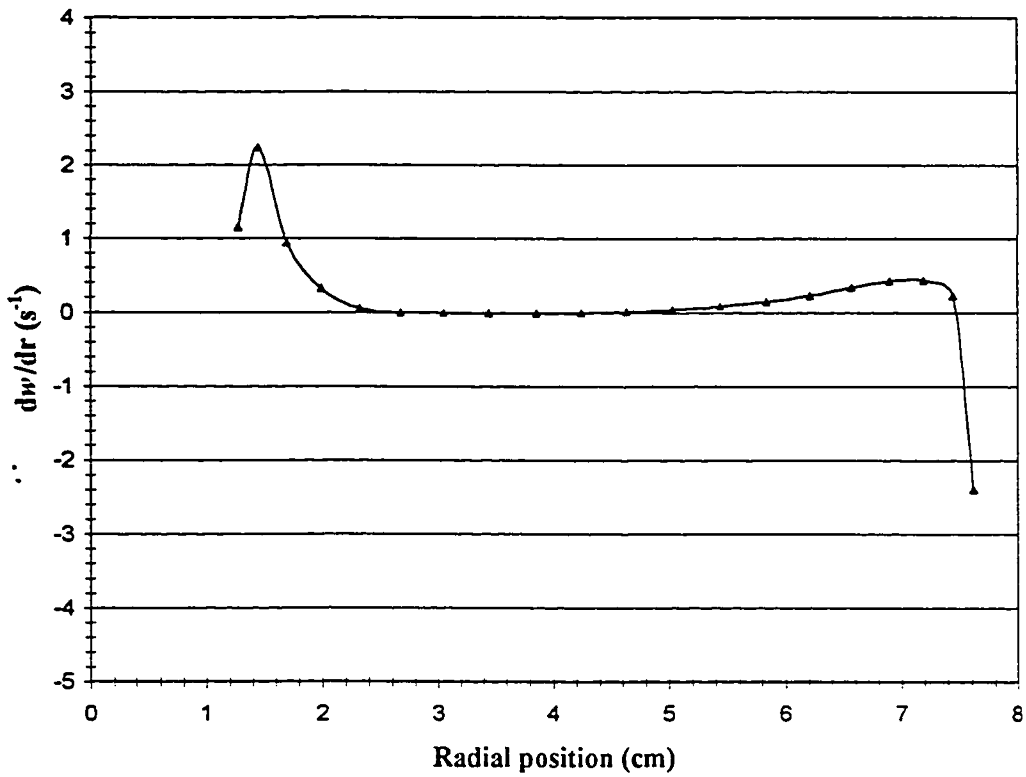

Figure 5.26: Shear rate versus radial distance from the inlet side of the eddy, for $\alpha = 45°$

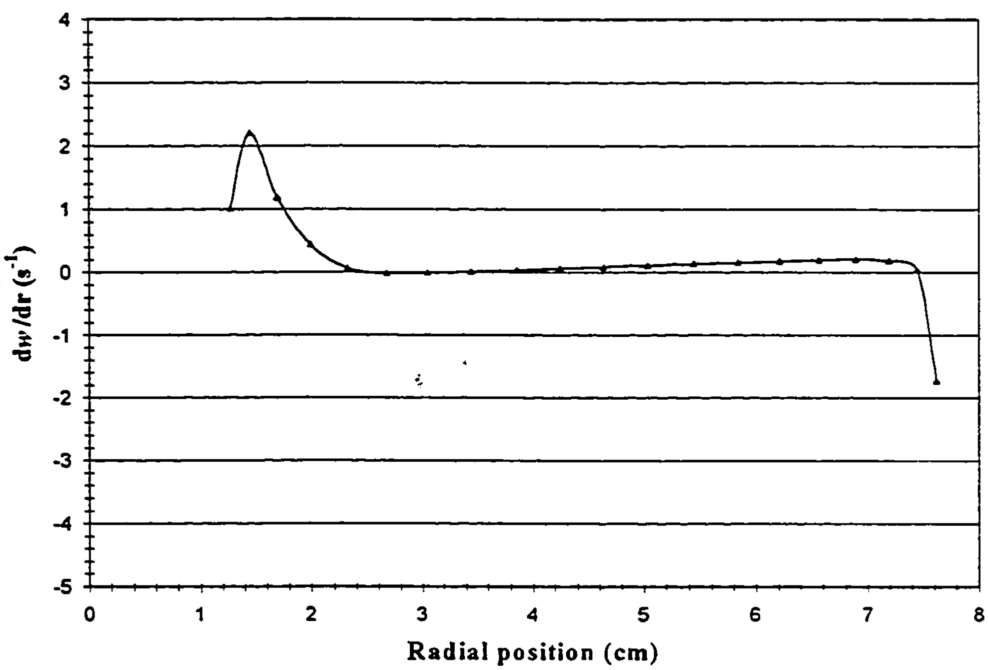

Figure 5.27: Shear rate versus radial distance from the inlet side of the eddy, for $\alpha = 55°$

moving regions. Particle traces were generated using the CFD-ACE+ package. A particle trace is the path taken by a hypothetical massless particle having no volume as it follows the streamlines from its point of injection. The longest streamline path obtained was for particles released in the center of the eddy located between two outlet tubes. Figure 5.28 illustrates such a particle trace for the case when $\alpha = 0°$. As we see, this hypothetical particle must follow a long and torturous path out of the eddy. Thus, the increase in particle concentration in the header and the steady-state values for accumulation within the header obtained by Chehab (1995) can be explained by both shear diffusion of particles toward the center of the eddy, and by slow eventual migration out of the header.

Sethi and Wiesner (1995) have developed a "microscopic" mass balance for particle transport across a polarized layer. The transport for a particle due to shear induced diffusion can be given as follows (Sethi and Wiesner, 1995):

$$N_p = \dot{\gamma}\, a^2 \hat{D}_{sh} \frac{d\varphi}{dr}, \tag{5.4–2}$$

where,

$$\dot{\gamma} = \left|\frac{dw}{dr}\right|, \tag{5.4–2}$$

a is the particle size, φ is the volume fraction of the particles, and $\hat{D}_{sh}$ is an experimentally determined dimensionless function of φ. Thus transport is in the direction

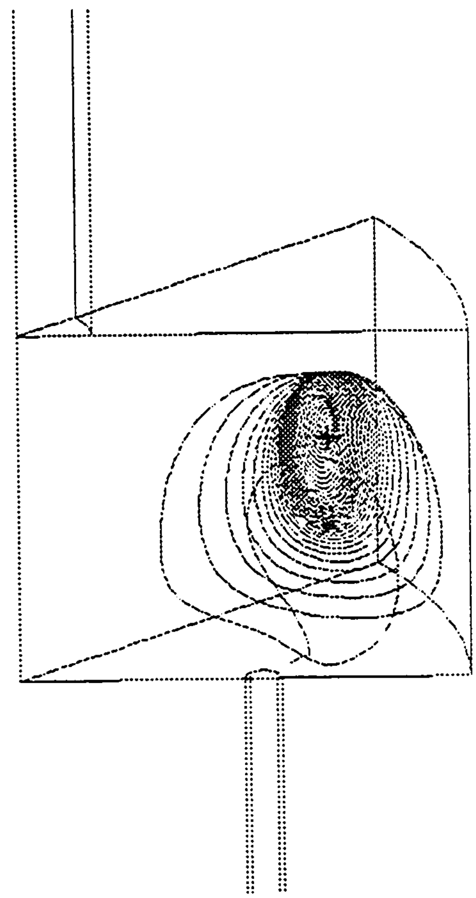

Figure 5.28 Particle trace plot in the 0 angle geometry injected in the vicinity of the center of an eddy.

of decreasing shear rate gradient. Assuming that the effect of the high shear present in the eddies is more dominant than that due to particle concentration gradients within the header, then it can be approximated that the flux is proportional to the shear rate. Thus:

$$N_p \,\alpha\, \frac{|u_c|}{L_c}, \tag{5.0–3}$$

where $|u_c|$ and L_c are some characteristic velocity and length respectively. As seen in Figures 5.19 through 5.22, the characteristic length of the eddy, (in between two outlet tubes), does not change appreciably as the inlet angle is altered. Therefore:

$$N_p \,\alpha\, |u_c|. \tag{5.0–4}$$

In essence then, Figure 5.23 shows the correlation of a characteristic velocity with the accumulation and is found to be strongly correlated.

A more suitable characteristic velocity of the eddy could be obtained which is more representative of the eddy intensity. It is proposed that an average total characteristic axial velocity can be defined as:

$$\overline{w}_c = \frac{\int_a^b \mathrm{abs}(w) \cdot dr}{b-a}, \tag{5.0–5}$$

where, a and b, the limits of integration take values from 2.5 cm from the central axis of the header to the wall. This distance from the center was chosen, as it was desired that the full eddy be considered but not the region that is strongly affected by the inlet jet. Figure 5.29 shows a plot of the correlation of the characteristic velocity and the observed accumulation. Again we see that there is a strong linear correlation with a correlation factor of 0.9986. The physical interpretation of the y-intercept is that a total average velocity of 0.0849 is required to produce no accumulation within the header.

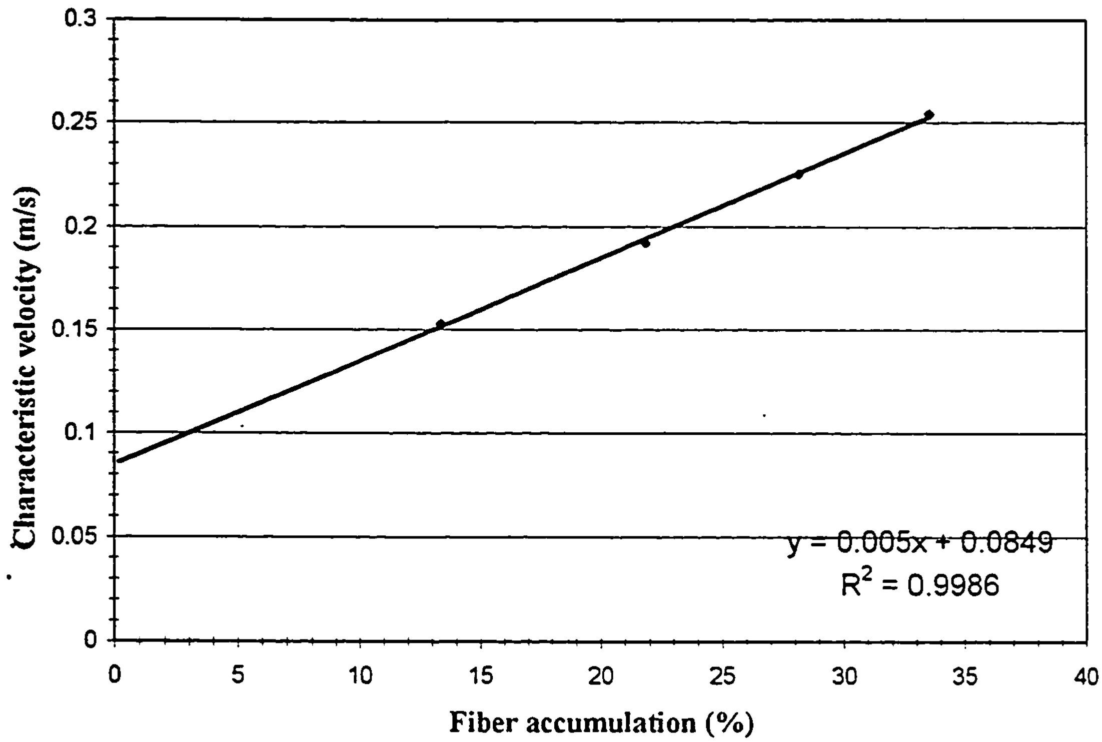

Figure 5.29: $\overline{w}_c$ versus % fiber accumulation correlation

Chapter 6.0

Conclusions

The following conclusions can be made from this work:

1. The eddy formation was identified as the key hydrodynamic element present in the module header.
2. There is a strong correlation between the eddy velocities and the accumulation of pulp fibers observed experimentally within the header.
3. Impingement and centrifugal forces could not account for the observed accumulation.
4. Shear diffusion is the dominant factor leading to fiber accumulation within the module header.
5. The gradual particle migration to the center of the eddy followed by a slow movement along the eddy and out the outlet tube explains the steady-state values of particle accumulation obtained experimentally.

Chapter 7.0

Recommendations

The following recommendations can be made:

1. For more rigorous simulations and denser grids, it is highly recommended that more RAM be installed on the HP workstation. The preferred amount would be approximately 128 Mb
2. A 21 inch colour display monitor capable of delivering resolutions up to 1600x1280 is also highly recommended for use as an interface as this eases the geometry and grid generation, and also greatly aids visualizations of the results.
3. Another option would be to switch the license to run the software on an Intel Pentium II platform. The cost to performance ratio is very small in comparison to that for Unix based workstations. A system failure would be less damaging as the availability of these computers is so high.
4. A module header geometry with ½ in. outlet tubes should be simulated to see if the velocity-accumulation correlation is independent of tube diameter.
5. The velocity information obtained in this study could be combined with the Shear Diffusion model to simulate the transient response of fiber accumulation within the header. This could then be compared to that observed experimentally.
6. The combination of the velocity information and the Shear Diffusion Model can also be used to identify regions within the header where, and under what conditions extreme aggregation might occur leading to tube blockage.

References

1. Afonso, M. D., and De Pinho, M. N., "Ultrafiltration of Bleach Effluents in Cellulose Production." Desalination, **79** (1990).

2. Bird, R. B., Stewart, W. E., Lightfoot, E. N., "Transport Phenomena", John Wiley & Sons, Inc., (1960).

3. Brady, John F., "Modeling Suspension Flows", ASME Liquid Solid Flows, **189**, p 1 (1994).

4. CFDRC, "CFD-ACE Theory Manual", CFD Research Corp. Huntsville Al., (1993).

5. CFDRC, "CFD-ACE User Guide", CFD Research Corp. Huntsville Al., (1996).

6. Chase, W. C., Donatelli, A. A., Walkinshaw, J. W., "Effects of Freeness and Consistency on the Viscosity of Hardwood and Softwood Pulp Suspensions." Tappi Journal, **72**(5), p 199 (1989).

7. Chehab, E.,Redesign of "Tubular Inlet Geometry to Reduce Fiber Accumulation in UF Modules", Masters thesis, University of Ottawa,(1995).

8. Chien, K. Y., "Predictions of Channel and Boundary-Layer Flows with Low-Reynolds-Number Turbulence Model," AIAA J., **20**, p33 (1982).

9. Davies, J. T., "Turbulence Phenomena", Academic Press, New York (1972).

10. Eckstein, E. C., Bailey, D.G., and Shapiro, A. H., "Self-Diffusion of Particles in Shear Flow of a Suspension," J. Fluid Mech., **79**, p191 (1977)

11. FDI, Fidap "Tutorial Manual", Fluid Dynamics International, Evanston, IL. (1993).

12. Fisheries and Environment Canada, "Site of Action of Chemicals From Pulp Mill Effluent That are Toxic to Fish", Project Report No. 488-2, (1978).

13. Gadala-Maria, F., Acrivos, A., "Shear Induced Structure in a Concentrated Suspension of Solid Spheres," J. Rheol., **24**, p799 (1980).

14. Gerald, C. F., Wheatley, P. O., "Applied Numerical Analysis", Addison-Wesley Publishing Company, Massachusetts, (1989).

16. Jenson, A. and Chenoweth, H. H., "Applied Engineering Mechanics", McGraw-Hill, New York (1972).

17. Jönsson, A. S., Jönsson C., Teppler, M., Tomani, P., Wänström, S., "Recovery of Dilute Paper Coating Colour Effluents by Ultrafiltration", Filtration and Separation, **33**(6), p453 (1996).

18. Jönsson, A. S., Jönsson C., Teppler, M., Tomani, P., Wänström, S.,"Treatment of Paper Coating Colour Effluents by Membrane Filtration", Desalination. **105**, p263 (1996).

19. Launder, B. E. and Spalding, D. B., Comp. Methods Appl. Mech. Eng., **3**, p269 (1974).

20. Leighton , D., and Acrivos, A., "Measurement of Shear-Induced Self-Diffusion in Concentrated Suspensions of Spheres," J. Fluid Mech., **177**, p109 (1987a).

21. Leighton , D., and Acrivos, A., "The Shear-Induced Migration of Particles in Concentrated Suspensions," J. Fluid Mech., **181**, p415 (1987b).

22. Riebel, P. N., Tyler, M. A., "Aquatic Ecosystem Monitoring at Canadian Pulp Mills: Overview and Future Directions", 1993 Environment Conference/Conférence sur l'environment 1993, pp89-96 (1993).

23. Sethi, S and Wiesner, M. R., "Performance and Cost Modeling of Ultrafiltration", Journal of Environmental Engineering, **121**(12), p 874 (1995).

24. Sun, Y-B., Joyce, T. W., Chang, H-M., "Dechlorination and decolorization of high-molecular-weight chlorolignin from bleach plant effluents by an oxidation process." Tappi Journal, **79**(9), p209 (1989).

25. Wilcox, D. C., "Progress in Hypersonic Turbulence Modeling," AIAA Paper 91-1785, (1991).

26. Wilcox, D. C., "Turbulence Modeling for CFD", DCW Industries, La Cañada, California,(1993).

27. Wiseman, N. and Ogden, G., "Zero Liquid Effluent Technologies for the Paper Industry", Paper Technology, **37**(1), p31 (1996).

28. Yakhot and Oszag , Phys. Rev. Lett., **57**, p1772 (1986).

29. Yakhot V., Smith, L. M., J. Sci. Comp., **7**(35), (1992).

30. Yao, W. X., Kennedy, K. J., Tam C. M., Hazlett, J. D., "Pre-treatment of Kraft Pulp Bleach Effluent by Selected Ultrafiltration Membranes," The Canadian Journal of Chemical Engineering, **72**, p991 (1994).

Appendix A

Raw Data for Velocity Traces

Table A.1: Raw Data for Line Traces

alpha = 0 degrees		alpha = 30 degrees		alpha = 45 degrees		alpha = 55 degrees	
Chord Length (in.)	w (m/s)	Chord Length (m)	w (m/s)	Chord Length (m)	w (m/s)	Chord Length (m)	w (m/s)
0	-1.57747	0	-1.03666	0	-1.13497	0	-1.08366
0.045	-1.73388	0.001143	-1.17359	0.00132933	-1.13248	0.00132933	-1.09062
0.09	-1.97623	0.002286	-1.45904	0.00265865	-1.12622	0.00265865	-1.10855
0.135	-2.11181	0.003429	-1.73129	0.00398797	-1.11929	0.00398797	-1.13242
0.18	-2.17689	0.004572	-1.94625	0.0053173	-1.11283	0.0053173	-1.15702
0.225	-2.17255	0.005715	-2.08302	0.00664662	-1.10282	0.00664662	-1.17269
0.27	-2.10001	0.006858	-2.11416	0.00797595	-0.94925	0.00797595	-1.03769
0.315	-1.96866	0.008001	-2.019	0.00970956	-0.5608	0.00970956	-0.65432
0.36	-1.79452	0.009144	-1.84751	0.0122446	-0.32258	0.0122446	-0.35507
0.405	-1.59199	0.010287	-1.65181	0.0152071	-0.2275	0.0152071	-0.2248
0.45	-1.37443	0.01143	-1.43485	0.0184866	-0.20937	0.0184866	-0.20203
0.495	-1.01008	0.012573	-1.0608	0.0220239	-0.20876	0.0220239	-0.20656
0.536723	-0.86841	0.0136328	-0.91189	0.0257812	-0.21073	0.0257812	-0.20977
0.590853	-0.56382	0.0150077	-0.58529	0.029732	-0.21453	0.029732	-0.20518
0.650925	-0.36711	0.0165335	-0.36351	0.0338562	-0.21894	0.0338562	-0.19111
0.715213	-0.28397	0.0181664	-0.26476	0.0377694	-0.22047	0.0377694	-0.16757
0.78283	-0.26582	0.0198839	-0.23961	0.0416825	-0.21575	0.0416825	-0.13371
0.853222	-0.26502	0.0216718	-0.23565	0.0455957	-0.20092	0.0455957	-0.09043
0.926012	-0.26698	0.0235207	-0.23503	0.0497199	-0.16808	0.0497199	-0.03482
1.00092	-0.26987	0.0254233	-0.2354	0.0536707	-0.11144	0.0536707	0.027868
1.07772	-0.27333	0.0273742	-0.23651	0.057428	-0.02524	0.057428	0.095155
1.15626	-0.27708	0.029369	-0.23822	0.0609653	0.092043	0.0609653	0.165479
1.23638	-0.28084	0.0314041	-0.24036	0.0642448	0.231193	0.0642448	0.23499
1.31798	-0.28429	0.0334767	-0.24271	0.0672073	0.359031	0.0672073	0.289299
1.40095	-0.28704	0.0355841	-0.24499	0.0697423	0.415767	0.0697423	0.299741
1.4852	-0.28869	0.0377242	-0.24685	0.071476	0	0.071476	0
1.57067	-0.28882	0.0398951	-0.24787	0.0751585	0	0.0751585	0
1.65729	-0.28698	0.0420952	-0.24762	0.0788411	0	0.0788411	0
1.745	-0.28267	0.044323	-0.24568	0.0825236	0	0.0825236	0
1.83271	-0.2753	0.0465508	-0.24151	0.0862061	0	0.0862061	0
1.91933	-0.26443	0.0487509	-0.23473	0.0898886	0	0.0898886	0
2.0048	-0.24976	0.0509218	-0.22511	0.0935712	0	0.0935712	0
2.08905	-0.23041	0.0530619	-0.21236	0.0972537	0	0.0972537	0
2.17202	-0.20535	0.0551693	-0.19558	0.100936	0	0.100936	0
2.25362	-0.17344	0.0572419	-0.17382	0.104619	0	0.104619	0
2.33374	-0.13306	0.059277	-0.14553	0.108301	0	0.108301	0
2.41228	-0.08203	0.0612718	-0.10845	0.111984	0	0.111984	0
2.48908	-0.01726	0.0632227	-0.05928	0.115666	0	0.115666	0
2.56399	0.064714	0.0651253	0.00723	0.119349	0	0.119349	0
2.63678	0.164403	0.0669742	0.09751				
2.70717	0.280309	0.0687621	0.213673				
2.77479	0.405477	0.0704796	0.346489				
2.83907	0.517426	0.0721125	0.470572				
2.89915	0.568544	0.0736383	0.533568				
2.95328	0.445989	0.0750133	0.419683				
2.995	0	0.076073	0				

Appendix B

Data for Mixing Length Correlation

Table B.1: Mixing Length Data Used for Correlation (Davies, 1972).

y/a	l/a
0.01509434	0.012073171
0.035849057	0.02195122
0.041509434	0.036585366
0.098113208	0.043902439
0.152830189	0.062195122
0.226415094	0.073902439
0.29245283	0.099878049
0.398113208	0.117073171
0.490566038	0.131707317
0.6	0.143414634
0.69245283	0.15
0.79245283	0.151829268
0.894339623	0.157317073
0.952830189	0.159146341
0.98490566	0.16097561

Appendix C

CFD-ACE Simulation Input Files

A.1 input file for $\alpha = 0°$

```
TITLE "
*
*
*
*
*
********************* Model *********************
*
*
MODEL 0-qrt8
*
GEOMETRY
 GRID 3D BFC
 READ GRID FROM 0-qrt8.PFGD
 SCALE 0.0254
* No Cell Types (Blockage or Solid) specified.
END
*
PROBLEM_TYPE
 SOLVE FLOW TURBULENCE
* Steady flow
END
*
PROPERTIES
 DENSITY CONSTANT 970.2
 VISCOSITY CONSTANT_DYNAMIC 0.0118
END
*
MODELS
 TURBULENCE_MODEL LOW_RE
END
*
*** Boundary Conditions ***
*
BOUNDARY_CONDITIONS
* boundary condition: INTERFACE_1
 INTERFACE 1 1 1 11 1 19 WEST
* boundary condition: inflow
 INLET 39 39 1 11 1 19 EAST
 U = 0 V = 0 W = PROF_2D P = 0 K = PROF_2D D = PROF_2D L = 0 T = 0
 W 34
 (0 0 10)
 (0.05 0 10)
 (0.1 0 10)
 (0.15 0 10)
 (0.2 0 10)
 (0.25 0 10)
 (0.3 0 10)
 (0.35 0 10)
 (0.4 0 10)
 (0.45 0 10)
 (0.49 0 10)
 (0.5 0 10)
 (0.04890738 0.010395585 10)
 (0.09781476 0.020791169 10)
 (0.14672214 0.031186754 10)
 (0.19562952 0.041582338 10)
 (0.2445369 0.051977923 10)
 (0.29344428 0.062373507 10)
 (0.34235166 0.072769092 10)
 (0.39125904 0.083164676 10)
 (0.44016642 0.093560261 10)
 (0.479292324 0.101876729 10)
 (0.4890738 0.103955845 10)
 (0.04045085 0.029389263 10)
```

(0.080901699 0.058778525 10)
(0.121352549 0.088167788 10)
(0.161803399 0.11755705 10)
(0.202254249 0.146946313 10)
(0.242705098 0.176335576 10)
(0.283155948 0.205724838 10)
(0.323606798 0.235114101 10)
(0.364057647 0.264503364 10)
(0.396418327 0.288014774 10)
(0.404508497 0.293892626 10)
-2.395585564
-2.354264264
-2.308914164
-2.25855614
-2.20178634
-2.136481
-2.059183907
-1.96364294
-1.836464269
-1.637833804
-1.255569121
0
-2.354264264
-2.308914164
-2.25855614
-2.20178634
-2.136481
-2.059183907
-1.96364294
-1.836464269
-1.637833804
-1.255569121
0
-2.354264264
-2.308914164
-2.25855614
-2.20178634
-2.136481
-2.059183907
-1.96364294
-1.836464269
-1.637833804
-1.255569121
0
K 31
(0 0 10)
(0.05 0 10)
(0.1 0 10)
(0.15 0 10)
(0.2 0 10)
(0.25 0 10)
(0.3 0 10)
(0.35 0 10)
(0.4 0 10)
(0.45 0 10)
(0.49 0 10)
(0.04890738 0.010395585 10)
(0.09781476 0.020791169 10)
(0.14672214 0.031186754 10)
(0.19562952 0.041582338 10)
(0.2445369 0.051977923 10)
(0.29344428 0.062373507 10)
(0.34235166 0.072769092 10)
(0.39125904 0.083164676 10)
(0.44016642 0.093560261 10)
(0.479292324 0.101876729 10)
(0.04045085 0.029389263 10)
(0.080901699 0.058778525 10)
(0.121352549 0.088167788 10)
(0.161803399 0.11755705 10)

(0.202254249 0.146946313 10)
(0.242705098 0.176335576 10)
(0.283155948 0.205724838 10)
(0.323606798 0.235114101 10)
(0.364057647 0.264503364 10)
(0.396418327 0.288014774 10)
0.000967369
0.001113436
0.001290756
0.001501057
0.001746166
0.002028401
0.002351905
0.002727044
0.003188039
0.003906467
0.006398253
0.001113436
0.001290756
0.001501057
0.001746166
0.002028401
0.002351905
0.002727044
0.003188039
0.003906467
0.006398253
0.001113436
0.001290756
0.001501057
0.001746166
0.002028401
0.002351905
0.002727044
0.003188039
0.003906467
0.006398253
D 31
(0 0 10)
(0.05 0 10)
(0.1 0 10)
(0.15 0 10)
(0.2 0 10)
(0.25 0 10)
(0.3 0 10)
(0.35 0 10)
(0.4 0 10)
(0.45 0 10)
(0.49 0 10)
(0.04890738 0.010395585 10)
(0.09781476 0.020791169 10)
(0.14672214 0.031186754 10)
(0.19562952 0.041582338 10)
(0.2445369 0.051977923 10)
(0.29344428 0.062373507 10)
(0.34235166 0.072769092 10)
(0.39125904 0.083164676 10)
(0.44016642 0.093560261 10)
(0.479292324 0.101876729 10)
(0.04045085 0.029389263 10)
(0.080901699 0.058778525 10)
(0.121352549 0.088167788 10)
(0.161803399 0.11755705 10)
(0.202254249 0.146946313 10)
(0.242705098 0.176335576 10)
(0.283155948 0.205724838 10)
(0.323606798 0.235114101 10)
(0.364057647 0.264503364 10)
(0.396418327 0.288014774 10)
0.000725618

```
0.000911974
0.001166451
0.001516473
0.002006384
0.002713859
0.003791049
0.00558905
0.009166018
0.020033578
0.125769866
0.000911974
0.001166451
0.001516473
0.002006384
0.002713859
0.003791049
0.00558905
0.009166018
0.020033578
0.125769866
0.000911974
0.001166451
0.001516473
0.002006384
0.002713859
0.003791049
0.00558905
0.009166018
0.020033578
0.125769866
* boundary condition: Symmetry_4
SYMMETRY 1 39 1 1 1 19 SOUTH
* boundary condition: Default
WALL 1 39 11 11 1 19 NORTH
U = 0 V = 0 W = 0
* boundary condition: Symmetry_4
SYMMETRY 1 39 1 11 1 1 LOW
* boundary condition: Symmetry_4
SYMMETRY 1 39 1 11 19 19 HIGH
DOMAIN 2
* boundary condition: INTERFACE_2
INTERFACE 1 1 25 31 1 4 WEST
* boundary condition: INTERFACE_2
INTERFACE 29 29 1 11 1 19 EAST
* boundary condition: Default
WALL 1 1 1 11 1 19 WEST
U = 0 V = 0 W = 0
* boundary condition: Default
WALL 1 1 12 45 5 19 WEST
U = 0 V = 0 W = 0
* boundary condition: Default
WALL 1 1 32 45 1 4 WEST
U = 0 V = 0 W = 0
* boundary condition: Default
WALL 1 1 12 24 1 4 WEST
U = 0 V = 0 W = 0
* boundary condition: Default
WALL 29 29 12 45 1 19 EAST
U = 0 V = 0 W = 0
* boundary condition: Symmetry_4
SYMMETRY 1 29 1 1 1 19 SOUTH
* boundary condition: Default
WALL 1 29 45 45 1 19 NORTH
U = 0 V = 0 W = 0
* boundary condition: Symmetry_4
SYMMETRY 1 29 12 45 1 1 LOW
* boundary condition: Symmetry_4
SYMMETRY 1 29 1 11 1 1 LOW
* boundary condition: Symmetry_4
SYMMETRY 1 29 1 11 19 19 HIGH
```

```
* boundary condition: Symmetry_4
 SYMMETRY 1 29 12 45 19 19 HIGH
 DOMAIN 3
* boundary condition: INTERFACE_3
 INTERFACE 34 34 1 7 1 4 EAST
* boundary condition: outflow
 EXIT_P 1 1 1 7 1 4 WEST
 U = 0 V = 0 W = -1   P = 0 K = 0.001 D = 0.00075 L = 0 T = 0
* boundary condition: Default
 WALL 1 34 1 1 1 4 SOUTH
 U = 0 V = 0 W = 0
* boundary condition: Default
 WALL 1 34 7 7 1 4 NORTH
 U = 0 V = 0 W = 0
* boundary condition: Symmetry_4
 SYMMETRY 1 34 1 7 1 1 LOW
* boundary condition: Default
 WALL 1 34 1 7 4 4 HIGH
 U = 0 V = 0 W = 0
END
*
INITIAL_CONDITIONS
* Full field initial conditions
 U = 0 V = 0 W = -1 P = 0 T = 0 K = 0.001 D = 0.00075 L = 0
END
*
********************** Solve **********************
*
*
SOLUTION_CONTROL
 ALGORITHM SIMPLEC
 S_SCHEME UPWIND U V W RHO K D
 ITERATIONS 1000
 C_ITERATIONS 1
 SOLVER WHOLE_I U V W K D
 SOLVER CG PP
 S_ITERATIONS 10 U V W
 S_ITERATIONS 500 PP
 S_ITERATIONS 10 K D
 INERTIAL_FACTOR 0.3 U V W
 INERTIAL_FACTOR 0.2 K D
 RELAX 1 P RHO T VIS
 MINVAL -1e+20 U V W
 MINVAL -1e+20 P
 MINVAL 1e-06 RHO
 MINVAL 1e-10 T VIS
 MINVAL 1e-10 K D
 MAXVAL 1e+20 U V W
 MAXVAL 1e+20 P RHO
 MAXVAL 5000 T
 MAXVAL 1e+20 VIS
 MAXVAL 1e+20 K D
END
*
OUTPUT
 PLOT3D ON FORMATTED
 SCALAR_FILE 1 YPLUS P T K D
 DIAGNOSTICS ON
 RESTART_SAVE 500
END
```

A.2 input file for $\alpha = 30°$

```
TITLE "
*
*
*
*
*
********************* Model *********************
*
*
MODEL 30-qrt5
*
GEOMETRY
 GRID 3D BFC
 READ GRID FROM 30-qrt5.PFGD
 SCALE 0.0254
* No Cell Types (Blockage or Solid) specified.
END
*
PROBLEM_TYPE
 SOLVE FLOW TURBULENCE
* Steady flow
END
*
PROPERTIES
 DENSITY CONSTANT 970.2
 VISCOSITY CONSTANT_DYNAMIC 0.0118
END
*
MODELS
 TURBULENCE_MODEL LOW_RE
END
*
*** Boundary Conditions ***
*
BOUNDARY_CONDITIONS
* boundary condition: INTERFACE_1
  INTERFACE 1 1 1 11 1 19 WEST
* boundary condition: inflow
  INLET 39 39 1 11 1 19 EAST
  U = 0 V = 0 W = PROF_2D P = 0 K = PROF_2D D = PROF_2D L = 0 T = 0
  W 34
  (0 0 10)
  (0.05 0 10)
  (0.1 0 10)
  (0.15 0 10)
  (0.2 0 10)
  (0.25 0 10)
  (0.3 0 10)
  (0.35 0 10)
  (0.4 0 10)
  (0.45 0 10)
  (0.49 0 10)
  (0.5 0 10)
  (0.04890738 0.010395585 10)
  (0.09781476 0.020791169 10)
  (0.14672214 0.031186754 10)
  (0.19562952 0.041582338 10)
  (0.2445369 0.051977923 10)
  (0.29344428 0.062373507 10)
  (0.34235166 0.072769092 10)
  (0.39125904 0.083164676 10)
  (0.44016642 0.093560261 10)
  (0.479292324 0.101876729 10)
  (0.4890738 0.103955845 10)
  (0.04045085 0.029389263 10)
  (0.080901699 0.058778525 10)
```

(0.121352549 0.088167788 10)
(0.161803399 0.11755705 10)
(0.202254249 0.146946313 10)
(0.242705098 0.176335576 10)
(0.283155948 0.205724838 10)
(0.323606798 0.235114101 10)
(0.364057647 0.264503364 10)
(0.396418327 0.288014774 10)
(0.404508497 0.293892626 10)
-2.395585564
-2.354264264
-2.308914164
-2.25855614
-2.20178634
-2.136481
-2.059183907
-1.96364294
-1.836464269
-1.637833804
-1.255569121
0
-2.354264264
-2.308914164
-2.25855614
-2.20178634
-2.136481
-2.059183907
-1.96364294
-1.836464269
-1.637833804
-1.255569121
0
-2.354264264
-2.308914164
-2.25855614
-2.20178634
-2.136481
-2.059183907
-1.96364294
-1.836464269
-1.637833804
-1.255569121
0
K 31
(0 0 10)
(0.05 0 10)
(0.1 0 10)
(0.15 0 10)
(0.2 0 10)
(0.25 0 10)
(0.3 0 10)
(0.35 0 10)
(0.4 0 10)
(0.45 0 10)
(0.49 0 10)
(0.04890738 0.010395585 10)
(0.09781476 0.020791169 10)
(0.14672214 0.031186754 10)
(0.19562952 0.041582338 10)
(0.2445369 0.051977923 10)
(0.29344428 0.062373507 10)
(0.34235166 0.072769092 10)
(0.39125904 0.083164676 10)
(0.44016642 0.093560261 10)
(0.479292324 0.101876729 10)
(0.04045085 0.029389263 10)
(0.080901699 0.058778525 10)
(0.121352549 0.088167788 10)
(0.161803399 0.11755705 10)
(0.202254249 0.146946313 10)

```
(0.242705098 0.176335576 10)
(0.283155948 0.205724838 10)
(0.323606798 0.235114101 10)
(0.364057647 0.264503364 10)
(0.396418327 0.288014774 10)
0.000967369
0.001113436
0.001290756
0.001501057
0.001746166
0.002028401
0.002351905
0.002727044
0.003188039
0.003906467
0.006398253
0.001113436
0.001290756
0.001501057
0.001746166
0.002028401
0.002351905
0.002727044
0.003188039
0.003906467
0.006398253
0.001113436
0.001290756
0.001501057
0.001746166
0.002028401
0.002351905
0.002727044
0.003188039
0.003906467
0.006398253
D 31
(0 0 10)
(0.05 0 10)
(0.1 0 10)
(0.15 0 10)
(0.2 0 10)
(0.25 0 10)
(0.3 0 10)
(0.35 0 10)
(0.4 0 10)
(0.45 0 10)
(0.49 0 10)
(0.04890738 0.010395585 10)
(0.09781476 0.020791169 10)
(0.14672214 0.031186754 10)
(0.19562952 0.041582338 10)
(0.2445369 0.051977923 10)
(0.29344428 0.062373507 10)
(0.34235166 0.072769092 10)
(0.39125904 0.083164676 10)
(0.44016642 0.093560261 10)
(0.479292324 0.101876729 10)
(0.04045085 0.029389263 10)
(0.080901699 0.058778525 10)
(0.121352549 0.088167788 10)
(0.161803399 0.11755705 10)
(0.202254249 0.146946313 10)
(0.242705098 0.176335576 10)
(0.283155948 0.205724838 10)
(0.323606798 0.235114101 10)
(0.364057647 0.264503364 10)
(0.396418327 0.288014774 10)
0.000725618
0.000911974
```

```
0.001166451
0.001516473
0.002006384
0.002713859
0.003791049
0.00558905
0.009166018
0.020033578
0.125769866
0.000911974
0.001166451
0.001516473
0.002006384
0.0027138.9
0.003791049
0.00558905
0.009166018
0.020033578
0.125769866
0.000911974
0.001166451
0.001516473
0.002006384
0.002713859
0.003791049
0.00558905
0.009166018
0.020033578
0.125769866
* boundary condition: Symmetry_4
 SYMMETRY 1 39 1 1 1 19 SOUTH
* boundary condition: Symmetry_4
 SYMMETRY 1 39 1 11 1 1 LOW
* boundary condition: Symmetry_4
 SYMMETRY 1 39 1 11 19 19 HIGH
 DOMAIN 2
* boundary condition: INTERFACE_2
 INTERFACE 34 34 1 9 1 5 EAST
* boundary condition: Outlet_2
 EXIT_P 1 1 1 9 1 5 WEST
 U = 0 V = 0 W = -4 P = 0 K = 0.001 D = 1000 L = 0 T = 0
* boundary condition: Symmetry_4
 SYMMETRY 1 34 1 9 1 1 LOW
 DOMAIN 3
* boundary condition: INTERFACE_3
 INTERFACE 1 1 1 9 1 5 WEST
* boundary condition: INTERFACE_3
 INTERFACE 9 9 1 9 1 5 EAST
* boundary condition: Symmetry_4
 SYMMETRY 1 9 1 9 1 1 LOW
 DOMAIN 4
* boundary condition: INTERFACE_4
 INTERFACE 1 1 24 32 1 5 WEST
* boundary condition: INTERFACE_4
 INTERFACE 29 29 1 11 1 19 EAST
* boundary condition: Symmetry_4
 SYMMETRY 1 29 1 1 1 19 SOUTH
* boundary condition: Symmetry_4
 SYMMETRY 1 29 12 45 1 1 LOW
* boundary condition: Symmetry_4
 SYMMETRY 1 29 1 11 1 1 LOW
* boundary condition: Symmetry_4
 SYMMETRY 1 29 1 11 19 19 HIGH
* boundary condition: Symmetry_4
 SYMMETRY 1 29 12 45 19 19 HIGH
END
*
INITIAL_CONDITIONS
* input for domain 1 (inlet)
 U = 0 V = 0 W = -1 P = 0 T = 0 K = 0.001 D = 0.00075 L = 0
```

```
* input for domain 2 (outlet)
 DOMAIN 2
 U = 0 V = 0 W = -4 P = 0 T = 0 K = 4 D = 1000 L = 0
* input for domain 3 (cone)
 DOMAIN 3
 U = 0 V = 0 W = -2 P = 0 T = 0 K = 0.05 D = .005 L = 0
* input for domain 4 (header)
 DOMAIN 4
 U = 0.1 V = -0.05 W = -1 P = 0 T = 0 K = 0.1 D = 4 L = 0
 END
*
********************* Solve *********************
*
*
SOLUTION_CONTROL
 ALGORITHM SIMPLEC
 S_SCHEME UPWIND U V W RHO K D
 ITERATIONS 1000
 C_ITERATIONS 1
 SOLVER WHOLE_I U V W
 SOLVER CG PP K D
 S_ITERATIONS 10 U V W
 S_ITERATIONS 500 PP
 S_ITERATIONS 500 K D
 INERTIAL_FACTOR 0.8 U V W
 INERTIAL_FACTOR 0.8 K D
 RELAX 0.8 P
 RELAX 0.8 RHO T VIS
 MINVAL -1e+20 U V W
 MINVAL -1e+20 P
 MINVAL 1e-06 RHO
 MINVAL 1e-10 T VIS
 MINVAL 1e-10 K D
 MAXVAL 1e+20 U V W
 MAXVAL 1e+20 P RHO
 MAXVAL 5000 T
 MAXVAL 1 VIS
 MAXVAL 1e+20 K D
END
*
OUTPUT
 PLOT3D ON FORMATTED
 SCALAR_FILE 1 RHO P T K D
 DIAGNOSTICS ON
 RESTART_SAVE 500
END
```

A.3 input file for $\alpha = 45°$

```
TITLE "
*
*
*
*
*
********************* Model *********************
*
*
MODEL 45-new5
*
GEOMETRY
 GRID 3D BFC
 READ GRID FROM 45-new5.PFGD
 SCALE 0.0254
```

```
* No Cell Types (Blockage or Solid) specified.
END
*
PROBLEM_TYPE
 SOLVE FLOW TURBULENCE
* Steady flow
END
*
PROPERTIES
 DENSITY CONSTANT 970.2
 VISCOSITY CONSTANT_DYNAMIC 0.0118
END
*
MODELS
 TURBULENCE_MODEL LOW_RE
END
*
*** Boundary Conditions ***
*
BOUNDARY_CONDITIONS
* boundary condition: INTERFACE_1
  INTERFACE 33 33 1 9 1 6 EAST
* boundary condition: INTERFACE_1
  INTERFACE 1 33 9 9 1 6 NORTH
* boundary condition: Default
  WALL 1 1 1 9 1 6 WEST
  U = 0 V = 0 W = 0
* boundary condition: Symmetry_4
  SYMMETRY 1 33 1 1 1 6 SOUTH
* boundary condition: Symmetry_4
  SYMMETRY 1 33 1 9 1 1 LOW
* boundary condition: Symmetry_4
  SYMMETRY 1 33 1 9 6 6 HIGH
  DOMAIN 2
* boundary condition: INTERFACE_2
  INTER
```

```
SYMMETRY 1 33 1 1 7 25 SOUTH
* boundary condition: Symmetry_4
SYMMETRY 1 33 1 15 1 1 LOW
* boundary condition: Symmetry_4
SYMMETRY 1 33 1 15 38 38 HIGH
DOMAIN 3
* boundary condition: INTERFACE_3
INTERFACE 1 1 1 38 1 11 WEST
* boundary condition: INTERFACE_3
INTERFACE 16 16 1 38 1 11 EAST
* boundary condition: Symmetry_4
SYMMETRY 1 16 1 1 1 11 SOUTH
* boundary condition: Symmetry_4
SYMMETRY 1 16 38 38 1 11 NORTH
* boundary condition: Symmetry_4
SYMMETRY 1 16 1 38 1 1 LOW
* boundary condition: Default
WALL 1 16 1 11 11 11 HIGH
U = 0 V = 0 W = 0
* boundary condition: Default
WALL 1 16 12 20 11 11 HIGH
U = 0 V = 0 W = 0
* boundary condition: Default
WALL 1 16 21 29 11 11 HIGH
U = 0 V = 0 W = 0
* boundary condition: Default
WALL 1 16 30 38 11 11 HIGH
U = 0 V = 0 W = 0
DOMAIN 4
* boundary condition: INTERFACE_4
INTERFACE 1 1 1 38 1 11 WEST
* boundary condition: INTERFACE_4
INTERFACE 1 33 1 6 11 11 HIGH
* boundary condition: INTERFACE_4
INTERFACE 1 33 7 11 11 11 HIGH
* boundary condition: INTERFACE_4
INTERFACE 1 33 12 20 11 11 HIGH
* boundary condition: INTERFACE_4
INTERFACE 1 33 21 25 11 11 HIGH
* boundary condition: INTERFACE_4
INTERFACE 1 33 26 29 11 11 HIGH
* boundary condition: INTERFACE_4
INTERFACE 1 33 30 38 11 11 HIGH
* boundary condition: Default
WALL 33 33 1 38 1 11 EAST
U = 0 V = 0 W = 0
* boundary condition: Symmetry_4
SYMMETRY 1 33 1 1 1 11 SOUTH
* boundary condition: Symmetry_4
SYMMETRY 1 33 38 38 1 11 NORTH
* boundary condition: Symmetry_4
SYMMETRY 1 33 1 38 1 1 LOW
DOMAIN 5
* boundary condition: INTERFACE_5
INTERFACE 1 1 1 9 1 6 WEST
* boundary condition: inflow
INLET 17 17 1 9 1 6 EAST
U = 0 V = 0 W = PROF_2D P = 0 K = PROF_2D D = PROF_2D L = 0 T = 0
W 34
(0 0 6)
(0.05 0 6)
(0.1 0 6)
(0.15 0 6)
(0.2 0 6)
(0.25 0 6)
(0.3 0 6)
(0.35 0 6)
(0.4 0 6)
(0.45 0 6)
(0.49 0 6)
```

(0.5 0 6)
(0.04890738 0.010395585 6)
(0.09781476 0.020791169 6)
(0.14672214 0.031186754 6)
(0.19562952 0.041582338 6)
(0.2445369 0.051977923 6)
(0.29344428 0.062373507 6)
(0.34235166 0.072769092 6)
(0.39125904 0.083164676 6)
(0.44016642 0.093560261 6)
(0.479292324 0.101876729 6)
(0.4890738 0.103955845 6)
(0.04045085 0.029389263 6)
(0.080901699 0.058778525 6)
(0.121352549 0.088167788 6)
(0.161803399 0.11755705 6)
(0.202254249 0.146946313 6)
(0.242705098 0.176335576 6)
(0.283155948 0.205724838 6)
(0.323606798 0.235114101 6)
(0.364057647 0.264503364 6)
(0.396418327 0.288014774 6)
(0.404508497 0.293892626 6)
-2.395585564
-2.354264264
-2.308914164
-2.25855614
-2.20178634
-2.136481
-2.059183907
-1.96364294
-1.836464269
-1.637833804
-1.255569121
0
-2.354264264
-2.308914164
-2.25855614
-2.20178634
-2.136481
-2.059183907
-1.96364294
-1.836464269
-1.637833804
-1.255569121
0
-2.354264264
-2.308914164
-2.25855614
-2.20178634
-2.136481
-2.059183907
-1.96364294
-1.836464269
-1.637833804
-1.255569121
0
K 31
(0 0 6)
(0.05 0 6)
(0.1 0 6)
(0.15 0 6)
(0.2 0 6)
(0.25 0 6)
(0.3 0 6)
(0.35 0 6)
(0.4 0 6)
(0.45 0 6)
(0.49 0 6)
(0.04890738 0.010395585 6)

```
(0.09781476 0.020791169 6)
(0.14672214 0.031186754 6)
(0.19562952 0.041582338 6)
(0.2445369 0.051977923 6)
(0.29344428 0.062373507 6)
(0.34235166 0.072769092 6)
(0.39125904 0.083164676 6)
(0.44016642 0.093560261 6)
(0.479292324 0.101876729 6)
(0.04045085 0.029389263 6)
(0.080901699 0.058778525 6)
(0.121352549 0.088167788 6)
(0.161803399 0.11755705 6)
(0.202254249 0.146946313 6)
(0.242705098 0.176335576 6)
(0.283155948 0.205724838 6)
(0.323606798 0.235114101 6)
(0.364057647 0.264503364 6)
(0.396418327 0.288014774 6)
0.000967369
0.001113436
0.001290756
0.001501057
0.001746166
0.002028401
0.002351905
0.002727044
0.003188039
0.003906467
0.006398253
0.001113436
0.001290756
0.001501057
0.001746166
0.002028401
0.002351905
0.002727044
0.003188039
0.003906467
0.006398253
0.001113436
0.001290756
0.001501057
0.001746166
0.002028401
0.002351905
0.002727044
0.003188039
0.003906467
0.006398253
D 31
(0 0 6)
(0.05 0 6)
(0.1 0 6)
(0.15 0 6)
(0.2 0 6)
(0.25 0 6)
(0.3 0 6)
(0.35 0 6)
(0.4 0 6)
(0.45 0 6)
(0.49 0 6)
(0.04890738 0.010395585 6)
(0.09781476 0.020791169 6)
(0.14672214 0.031186754 6)
(0.19562952 0.041582338 6)
(0.2445369 0.051977923 6)
(0.29344428 0.062373507 6)
(0.34235166 0.072769092 6)
(0.39125904 0.083164676 6)
```

```
(0.44016642 0.093560261 6)
(0.479292324 0.101876729 6)
(0.04045085 0.029389263 6)
(0.080901699 0.058778525 6)
(0.121352549 0.088167788 6)
(0.161803399 0.11755705 6)
(0.202254249 0.146946313 6)
(0.242705098 0.176335576 6)
(0.283155948 0.205724838 6)
(0.323606798 0.235114101 6)
(0.364057647 0.264503364 6)
(0.396418327 0.288014774 6)
0.000725618
0.000911974
0.001166451
0.001516473
0.002006384
0.002713859
0.003791049
0.00558905
0.009166018
0.020033578
0.125769866
0.000911974
0.001166451
0.001516473
0.002006384
0.002713859
0.003791049
0.00558905
0.009166018
0.020033578
0.125769866
0.000911974
0.001166451
0.001516473
0.002006384
0.002713859
0.003791049
0.00558905
0.009166018
0.020033578
0.125769866
* boundary condition: Symmetry_4
SYMMETRY 1 17 1 1 1 6 SOUTH
* boundary condition: Default
WALL 1 17 9 9 1 6 NORTH
U = 0 V = 0 W = 0
* boundary condition: Symmetry_4
SYMMETRY 1 17 1 9 1 1 LOW
* boundary condition: Symmetry_4
SYMMETRY 1 17 1 9 6 6 HIGH
DOMAIN 6
* boundary condition: INTERFACE_6
INTERFACE 11 11 1 38 1 11 EAST
* boundary condition: outflow
EXIT_P 1 1 1 38 1 11 WEST
U = 0 V = 0 W = -5  P = 0 K = 1 D = 500 L = 0 T = 0
* boundary condition: Symmetry_4
SYMMETRY 1 11 1 1 1 11 SOUTH
* boundary condition: Symmetry_4
SYMMETRY 1 11 38 38 1 11 NORTH
* boundary condition: Symmetry_4
SYMMETRY 1 11 1 38 1 1 LOW
* boundary condition: Default
WALL 1 11 1 11 11 11 HIGH
U = 0 V = 0 W = 0
* boundary condition: Default
WALL 1 11 12 20 11 11 HIGH
U = 0 V = 0 W = 0
```

```
* boundary condition: Default
 WALL 1 11 21 29 11 11  HIGH
 U = 0 V = 0 W = 0
* boundary condition: Default
 WALL 1 11 30 38 11 11  HIGH
 U = 0 V = 0 W = 0
END
*
INITIAL_CONDITIONS
RESTART FROM 45-new5.PFS CONTINUE
END
*
********************* Solve **********************
*
*
SOLUTION_CONTROL
 ALGORITHM SIMPLEC
 S_SCHEME UPWIND U V W RHO K D
 ITERATIONS 2500
 C_ITERATIONS 2
 SOLVER WHOLE_I U V W
 SOLVER CG PP K D
 S_ITERATIONS 50 U V W
 S_ITERATIONS 1200 PP
 S_ITERATIONS 1000 K D
 INERTIAL_FACTOR 0.5 U V W
 INERTIAL_FACTOR 0.4 K D
 RELAX 0.7 P RHO T VIS
 MINVAL -1e+20 U V W
 MINVAL -1e+20 P
 MINVAL 1e-06 RHO
 MINVAL 1e-10 T VIS
 MINVAL 1e-10 K D
 MAXVAL 1e+20.U V W
 MAXVAL 1e+20 P RHO
 MAXVAL 5000 T
 MAXVAL 1 VIS
 MAXVAL 1e+20 K D
END
*
OUTPUT
 PLOT3D ON FORMATTED
 SCALAR_FILE 1 VIS P YPLUS K D
 DIAGNOSTICS ON
 RESTART_SAVE 200
END
```

A.4 input file for $\alpha = 55°$

```
TITLE "
*
*
*
*
*
********************** Model **********************
*
*
MODEL 55-qrt
*
GEOMETRY
```

```
 GRID 3D BFC
 READ GRID FROM 55-qrt.PFGD
 SCALE 0.0254
* No Cell Types (Blockage or Solid) specified.
END
*
PROBLEM_TYPE
 SOLVE FLOW TURBULENCE
* Steady flow
END
*
PROPERTIES
 DENSITY CONSTANT 970.2
 VISCOSITY CONSTANT_DYNAMIC 0.0118
END
*
MODELS
 TURBULENCE_MODEL LOW_RE
END
*
*** Boundary Conditions ***
*
BOUNDARY_CONDITIONS
* boundary condition: INTERFACE_1
  INTERFACE 27 27 1 9 1 6 EAST
* boundary condition: INTERFACE_1
  INTERFACE 1 27 9 9 1 6 NORTH
* boundary condition: Default
  WALL 1 1 1 9 1 6 WEST
  U = 0 V = 0 W = 0
* boundary condition: Symmetry_4
  SYMMETRY 1 27 1 1 1 6 SOUTH
* boundary condition: Symmetry_4
  SYMMETRY 1 27 1 9 1 1 LOW
* boundary condition: Symmetry_4
  SYMMETRY 1 27 1 9 6 6 HIGH
  DOMAIN 2
* boundary condition: INTERFACE_2
  INTERFACE 1 1 1 9 1 6 WEST
* boundary condition: inflow
  INLET 16 16 1 9 1 6 EAST
  U = 0 V = 0 W = PROF_2D P = 0 K = PROF_2D D = PROF_2D L = 0 T = 0
  W 34
  (0 0 6)
  (0.05 0 6)
  (0.1 0 6)
  (0.15 0 6)
  (0.2 0 6)
  (0.25 0 6)
  (0.3 0 6)
  (0.35 0 6)
  (0.4 0 6)
  (0.45 0 6)
  (0.49 0 6)
  (0.5 0 6)
  (0.04890738 0.010395585 6)
  (0.09781476 0.020791169 6)
  (0.14672214 0.031186754 6)
  (0.19562952 0.041582338 6)
  (0.2445369 0.051977923 6)
  (0.29344428 0.062373507 6)
  (0.34235166 0.072769092 6)
  (0.39125904 0.083164676 6)
  (0.44016642 0.093560261 6)
  (0.479292324 0.101876729 6)
  (0.4890738 0.103955845 6)
  (0.04045085 0.029389263 6)
  (0.080901699 0.058778525 6)
  (0.121352549 0.088167788 6)
  (0.161803399 0.11755705 6)
```

```
(0.202254249 0.146946313 6)
(0.242705098 0.176335576 6)
(0.283155948 0.205724838 6)
(0.323606798 0.235114101 6)
(0.364057647 0.264503364 6)
(0.396418327 0.288014774 6)
(0.404508497 0.293892626 6)
-2.395585564
-2.354264264
-2.308914164
-2.25855614
-2.20178634
-2.136481
-2.059183907
-1.96364294
-1.836464269
-1.637833804
-1.255569121
0
-2.354264264
-2.308914164
-2.25855614
-2.20178634
-2.136481
-2.059183907
-1.96364294
-1.836464269
-1.637833804
-1.255569121
0
-2.354264264
-2.308914164
-2.25855614
-2.20178634
-2.136481
-2.059183907
-1.96364294
-1.836464269
-1.637833804
-1.255569121
0
K 31
(0 0 6)
(0.05 0 6)
(0.1 0 6)
(0.15 0 6)
(0.2 0 6)
(0.25 0 6)
(0.3 0 6)
(0.35 0 6)
(0.4 0 6)
(0.45 0 6)
(0.49 0 6)
(0.04890738 0.010395585 6)
(0.09781476 0.020791169 6)
(0.14672214 0.031186754 6)
(0.19562952 0.041582338 6)
(0.2445369 0.051977923 6)
(0.29344428 0.062373507 6)
(0.34235166 0.072769092 6)
(0.39125904 0.083164676 6)
(0.44016642 0.093560261 6)
(0.479292324 0.101876729 6)
(0.04045085 0.029389263 6)
(0.080901699 0.058778525 6)
(0.121352549 0.088167788 6)
(0.161803399 0.11755705 6)
(0.202254249 0.146946313 6)
(0.242705098 0.176335576 6)
(0.283155948 0.205724838 6)
```

(0.323606798 0.235114101 6)
(0.364057647 0.264503364 6)
(0.396418327 0.288014774 6)
0.000967369
0.001113436
0.001290756
0.001501057
0.001746166
0.002028401
0.002351905
0.002727044
0.003188039
0.003906467
0.006398253
0.001113436
0.001290756
0.001501057
0.001746166
0.002028401
0.002351905
0.002727044
0.003188039
0.003906467
0.006398253
0.001113436
0.001290756
0.001501057
0.001746166
0.002028401
0.002351905
0.002727044
0.003188039
0.003906467
0.006398253
D 31
(0 0 6)
(0.05 0 6)
(0.1 0 6)
(0.15 0 6)
(0.2 0 6)
(0.25 0 6)
(0.3 0 6)
(0.35 0 6)
(0.4 0 6)
(0.45 0 6)
(0.49 0 6)
(0.04890738 0.010395585 6)
(0.09781476 0.020791169 6)
(0.14672214 0.031186754 6)
(0.19562952 0.041582338 6)
(0.2445369 0.051977923 6)
(0.29344428 0.062373507 6)
(0.34235166 0.072769092 6)
(0.39125904 0.083164676 6)
(0.44016642 0.093560261 6)
(0.479292324 0.101876729 6)
(0.04045085 0.029389263 6)
(0.080901699 0.058778525 6)
(0.121352549 0.088167788 6)
(0.161803399 0.11755705 6)
(0.202254249 0.146946313 6)
(0.242705098 0.176335576 6)
(0.283155948 0.205724838 6)
(0.323606798 0.235114101 6)
(0.364057647 0.264503364 6)
(0.396418327 0.288014774 6)
0.000725618
0.000911974
0.001166451
0.001516473

```
0.002006384
0.002713859
0.003791049
0.00558905
0.009166018
0.020033578
0.125769866
0.000911974
0.001166451
0.001516473
0.002006384
0.002713859
0.003791049
0.00558905
0.009166018
0.020033578
0.125769866
0.000911974
0.001166451
0.001516473
0.002006384
0.002713859
0.003791049
0.00558905
0.009166018
0.020033578
0.125769866
* boundary condition: Symmetry_4
 SYMMETRY 1 16 1 1 1 6  SOUTH
* boundary condition: Default
 WALL 1 16 9 9 1 6  NORTH
 U = 0 V = 0 W = 0
* boundary condition: Symmetry_4
 SYMMETRY 1 16 1 9 1 1  LOW
* boundary condition: Symmetry_4
 SYMMETRY 1 16 1 9 6 6  HIGH
 DOMAIN 3
* boundary condition: INTERFACE_3
 INTERFACE 10 10 1 38 1 16  EAST
* boundary condition: outflow
 EXIT_P 1 1 1 38 1 16  WEST
 U = 0 V = 0 W = -5   P = 0 K = 1 D = 500 L = 0 T = 0
* boundary condition: Symmetry_4
 SYMMETRY 1 10 1 1 1 16  SOUTH
* boundary condition: Symmetry_4
 SYMMETRY 1 10 38 38 1 16  NORTH
* boundary condition: Symmetry_4
 SYMMETRY 1 10 1 38 1 1  LOW
* boundary condition: Default
 WALL 1 10 1 11 16 16  HIGH
 U = 0 V = 0 W = 0
* boundary condition: Default
 WALL 1 10 12 20 16 16  HIGH
 U = 0 V = 0 W = 0
* boundary condition: Default
 WALL 1 10 21 29 16 16  HIGH
 U = 0 V = 0 W = 0
* boundary condition: Default
 WALL 1 10 30 38 16 16  HIGH
 U = 0 V = 0 W = 0
 DOMAIN 4
* boundary condition: INTERFACE_4
 INTERFACE 1 1 1 38 1 16  WEST
* boundary condition: INTERFACE_4
 INTERFACE 15 15 1 38 1 16  EAST
* boundary condition: Symmetry_4
 SYMMETRY 1 15 1 1 1 16  SOUTH
* boundary condition: Symmetry_4
 SYMMETRY 1 15 38 38 1 16  NORTH
* boundary condition: Symmetry_4
```

```
SYMMETRY 1 15 1 38 1 1 LOW
* boundary condition: Default
WALL 1 15 1 11 16 16 HIGH
U = 0 V = 0 W = 0
* boundary condition: Default
WALL 1 15 12 20 16 16 HIGH
U = 0 V = 0 W = 0
* boundary condition: Default
WALL 1 15 21 29 16 16 HIGH
U = 0 V = 0 W = 0
* boundary condition: Default
WALL 1 15 30 38 16 16 HIGH
U = 0 V = 0 W = 0
DOMAIN 5
* boundary condition: INTERFACE_5
INTERFACE 1 1 1 38 1 16 WEST
* boundary condition: INTERFACE_5
INTERFACE 1 27 1 11 16 16 HIGH
* boundary condition: INTERFACE_5
INTERFACE 1 27 12 20 16 16 HIGH
* boundary condition: INTERFACE_5
INTERFACE 1 27 21 29 16 16 HIGH
* boundary condition: INTERFACE_5
INTERFACE 1 27 30 38 16 16 HIGH
* boundary condition: Default
WALL 27 27 1 38 1 16 EAST
U = 0 V = 0 W = 0
* boundary condition: Symmetry_4
SYMMETRY 1 27 1 1 1 16 SOUTH
* boundary condition: Symmetry_4
SYMMETRY 1 27 38 38 1 16 NORTH
* boundary condition: Symmetry_4
SYMMETRY 1 27 1 38 1 1 LOW
DOMAIN 6
* boundary condition: INTERFACE_6
INTERFACE 1 27 1 11 1 1 LOW
* boundary condition: INTERFACE_6
INTERFACE 1 27 12 20 1 1 LOW
* boundary condition: INTERFACE_6
INTERFACE 1 27 21 29 1 1 LOW
* boundary condition: INTERFACE_6
INTERFACE 1 27 30 38 1 1 LOW
* boundary condition: INTERFACE_6
INTERFACE 1 27 1 6 13 13 HIGH
* boundary condition: Default
WALL 1 1 26 38 1 13 WEST
U = 0 V = 0 W = 0
* boundary condition: Default
WALL 1 1 7 25 1 13 WEST
U = 0 V = 0 W = 0
* boundary condition: Default
WALL 1 1 1 6 1 13 WEST
U = 0 V = 0 W = 0
* boundary condition: Default
WALL 27 27 7 25 1 13 EAST
U = 0 V = 0 W = 0
* boundary condition: Default
WALL 27 27 26 38 1 13 EAST
U = 0 V = 0 W = 0
* boundary condition: Default
WALL 27 27 1 6 1 13 EAST
U = 0 V = 0 W = 0
* boundary condition: Symmetry_4
SYMMETRY 1 27 1 1 1 13 SOUTH
* boundary condition: Symmetry_4
SYMMETRY 1 27 38 38 1 13 NORTH
* boundary condition: Symmetry_4
SYMMETRY 1 27 7 25 13 13 HIGH
* boundary condition: Default
WALL 1 27 26 38 13 13 HIGH
```

```
 U = 0 V = 0 W = 0
END
*
INITIAL_CONDITIONS
RESTART FROM 55-qrt.AUR CONTINUE
END
*
********************* Solve **********************
*
*
SOLUTION_CONTROL
 ALGORITHM SIMPLEC
 S_SCHEME UPWIND U V W RHO K D
 ITERATIONS 1000
 C_ITERATIONS 1
 SOLVER WHOLE_1 U V W
 SOLVER CG PP K D
 S_ITERATIONS 50 U V W
 S_ITERATIONS 1200 PP
 S_ITERATIONS 1000 K D
 INERTIAL_FACTOR 0.5 U V W
 INERTIAL_FACTOR 0.4 K D
 RELAX 0.7 P RHO T VIS
 MINVAL -1e+20 U V W
 MINVAL -1e+20 P
 MINVAL 1e-06 RHO
 MINVAL 1e-10 T VIS
 MINVAL 1e-10 K D
 MAXVAL 1e+20 U V W
 MAXVAL 1e+20 P RHO
 MAXVAL 5000 T
 MAXVAL 1 VIS
 MAXVAL 1e+20 K D
END
*
OUTPUT
 PLOT3D ON FORMATTED
 SCALAR_FILE 1 VIS P T K D
 DIAGNOSTICS ON
 RESTART_SAVE 100
END
```